Ion Transport Phenomena in Electrode Materials

Jing Wen[1,2], Xinzhi Ma[1], Lu Li[1], Xitian Zhang[*,1], Bin Wang[*,2]

[1]*Key Laboratory for Photonic and Electronic Bandgap Materials, Ministry of Education, School of Physics and Electronic Engineering, Harbin Normal University, Harbin 150025, P. R. China*

[2]*School of Chemical, Biological and Materials Engineering, University of Oklahoma, Norman, OK 73019, United States*

Abstract: Because of the increasing demand, high-power, high-rate energy storage devices based on the electrode materials have attracted immense attention. However, challenges remain to be addressed to improve the concentration-dependent kinetics of ionic diffusion and understand phase transformation, interfacial reactions, and capacitive behaviors that vary with particle morphology and scanning rates. It is valuable to understand the microscopic origins of ion transport in electrode materials. In this review, we discuss the microscopic transport phenomena and their dependence on ion concentration in the cathode materials by comparing dozens of well-studied transition metal oxides, sulfides, phosphates, and in the anode materials including several carbon species and carbides. We generalize the kinetic effects on the microscopic ionic transport processes from the phenomenological points of view based on the well-studied systems. The dominant kinetic effects on ion diffusion varied with ion concentration, and the pathway- and morphology-dependent diffusion and capacitive behaviors affected by the sizes and boundaries of particles are demonstrated. The important kinetic effects on ion transport by phase transformation, transferred electrons, and water molecules are discussed. The results are expected to shed light on the microscopic limiting factors of charging/discharging rates for developing new intercalation and conversion reaction systems.

Keywords: Ion transport; Electrode materials; Intercalation materials; Transport kinetics

1. Introduction

Lithium ion batteries is one of the currently most important energy storage cells due to the reversible electrochemical processes based on the intercalation/deintercalation of guest ions in the electrode materials accompanied by the electronic transport. Increasing need for these cells possessing long cycling capability and safety with high energy and power densities is vaster than ever before. To meet the high-rate charging/discharging requirements without significantly sacrificing the capacity, many efforts have been devoted to modifying the intercalation battery materials[1-7] or exploring capacitive materials with bulk storage capability.[8-12] Several effective strategies have been developed including crystallization of nanostructures,[13-14] coating the particles with conductive materials,[15-16] modifying the structural dimensions, boundaries, shapes, and orientations of the systems,[1, 8, 17-19] and many others.[20-21] Most of the methods have been mainly focused on the modification of ionic diffusion at the interior and interface of the electrode system because it is generally believed that the rate capability is limited by these processes. However, the microscopic ionic transport processes and kinetics depend on many parameters, such as the guest-ion concentration, crystal and electronic structures of the host, phase transformation, sizes and morphologies of the electrode particles; all these complicate the transport phenomena and present the challenges for finding out the microscopic rate-limiting step for a specific sample.

For clarifying the transport capability of ions in an electrode, quantitative description of the collective movement commonly employs the diffusion coefficient D as defined in the macroscopic phenomenological Fick's law. Without considering the local electric field induced by the polarized electrons, the diffusion coefficient in a neutral single-phase host is mainly controlled by the chemical environment of the intercalation compound, which can be measured based on the potentiostatic and

galvanostatic intermittent titration techniques (PITT and GITT),[22-23] or electrochemical impedance spectroscopy (EIS).[24-25] The value of *D* can span several orders of magnitude for a given system (e.g. 10^{-6}~10^{-16} cm^2/s in graphite)[26-27] due to the boundary and concentration-dependent effects. It is very helpful to use *D* to estimate the ion mobility, and then to correlate with the rate performance for a given sample. However, experimental measurement of *D* usually relies on the response of the whole ionic transport process in a cell, which can obscure the boundary reactions and inner transport processes, and cannot provide the information about the microscopic ionic transport details and their dominant factors. Furthermore, the increase of guest-ion concentration in the host is usually accompanied by phase transformation during the charging/discharging processes. It can invalidate the diffusion kinetics described by *D*. In recent years, transformations of solid-state diffusion to the capacitive behavior caused by the size effects or the presence of water have been observed in many electrode materials, indicating the existence of the kinetic transformation condition for the tradeoff between the capacity and rate capability. These difficulties show the challenges for the kinetic description about the ionic transport phenomena. Many excellent reviews, such as those by Whittingham,[5, 28-29] Goodenough,[30-31] and others,[13, 20, 32-50] have summarized the electrochemical performances for several types of electrode materials and shed light on the ionic diffusion mechanisms under the single-phase limitation.[34, 51-52] However, a knowledge gap is still left for the connections among different materials on these multiple kinetic processes.

In this review, we summarize several electrode materials on their ionic transport properties. The selected systems belong to the well-studied electrode materials including the cathode materials, such as Li_xMO_2 (*M* = Co, Ni, $Ni_{1-y-z}Mn_zCo_y$), Li_xTiS_2, six polymorphs of MnO_2, $Li_xM_2O_4$ (*M* = Mn, Ti), $LiFePO_4$, and others, and the anode materials including graphite, graphene, MXenes, $Li_4Ti_5O_{12}$, and others, where *x* is the concentration of guest ions. Lithium ion is selected as the representative guest species and some other representative ions are also discussed. The microscopic ionic transport

processes and kinetic effects are classified into several parts as depicted in Figure 1. We mainly focus on the phenomena and mechanisms of ion transport developed in this field. In single phases, the concentration-dependent diffusion processes are presented in Section 2. The dominant factors that influence the trends of the measured $D(x)$ varied with increasing ion-concentration x are discussed based on the density functional theory (DFT) calculations and nuclear magnetic resonance (NMR) experiments. Because the measured values of $D(x)$ depend on the geometries of the electrode particles and vary from sample to sample, we only discuss the trends observed in the measured $D(x)$ curves with x that have been confirmed by several reported results rather than stressing their values. Phase transformation effects on the ion transport are described in Section 3. Two-phase coexistence transport and the typical order-disorder and metal-insulator transformation effects are presented and discussed. In Section 4, the size effects on the kinetic variation at different scales are summarized. The morphology-dependent diffusion including the interfacial and orientation effects has also been discussed here. The cooperative effects on the ion transport induced by the transferred electrons and water molecules are presented in Section 5. Summary and outlook can be found in Section 6.

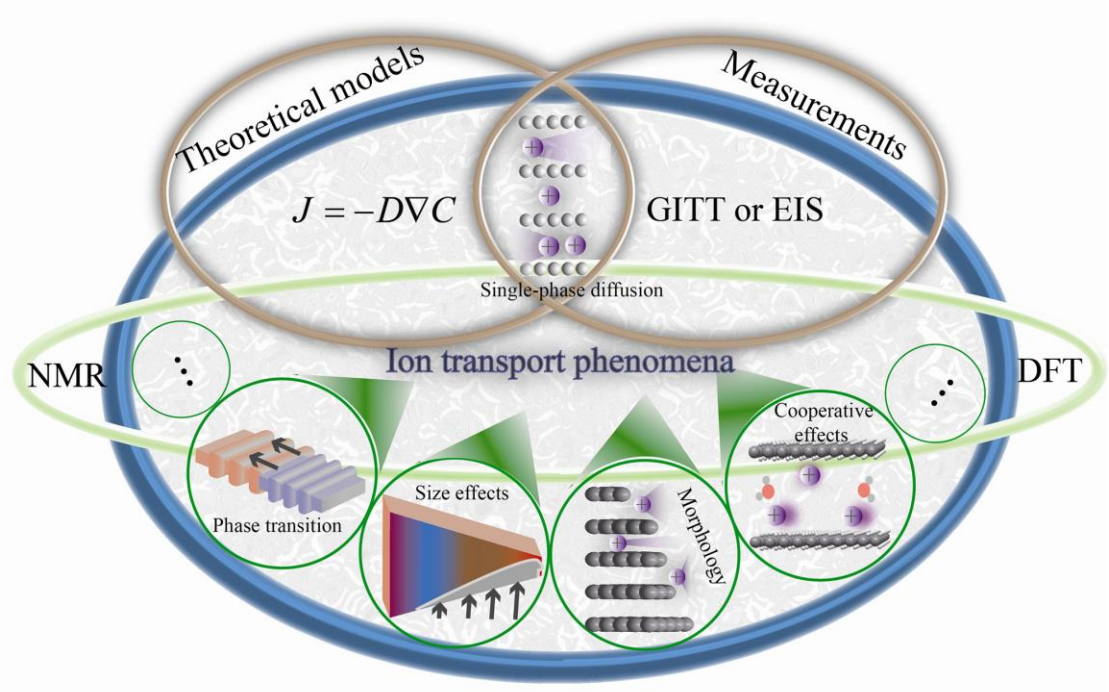

Figure 1. Schematic diagram for the ionic transport phenomena classified from their different kinetic processes. The abbreviations and cycles denote the experimental and theoretical methods usually employed to quantitatively study these phenomena and their correlations.

2. Concentration dependence of ionic diffusion in the single phase

2.1. Concentration-dependent diffusion coefficient

Collective transport behavior of guest ions in a single-phase solid-solution state can be quantitatively reflected by the chemical diffusion coefficient D defined in the Fick's first law by $J = -D\nabla C$, where J and C are the net particle flux and local particle concentration. D is always a function of ion concentration x as shown in Figure 2, which gives several measured $D(x)$ for different electrode materials at room temperature. Each of the $D(x)$ curves exhibits multiple trends at different intervals of x. The trends of $D(x)$ present the evidence that there should be a dominant diffusion mechanism in each monotonic range. Characterizing the dominant effects on the ion diffusion mainly depends on the microscopic details of ion movement. An available method to visualize whether it is difficult or not to move ions in a specific interstitial network is to depict the migration energy profile along the preferred pathway in the host structure. The migration barrier (or activation barrier) ΔE along the pathway, defined as the difference of energies between the activated and equilibrium states as shown in Figure 2(a), can characterize the migration behavior of ions between the nearest-neighboring equilibrium sites under the thermodynamic state, and hence plays the dominant role in influencing the diffusion coefficient based the relationship of $D \propto e^{-\Delta E/kT}$,[53] where k and T are Boltzmann constant and temperature. Therefore, any change in the interaction imposed on the guest ions can reshape the migration energy profile, and then affect the value of D.

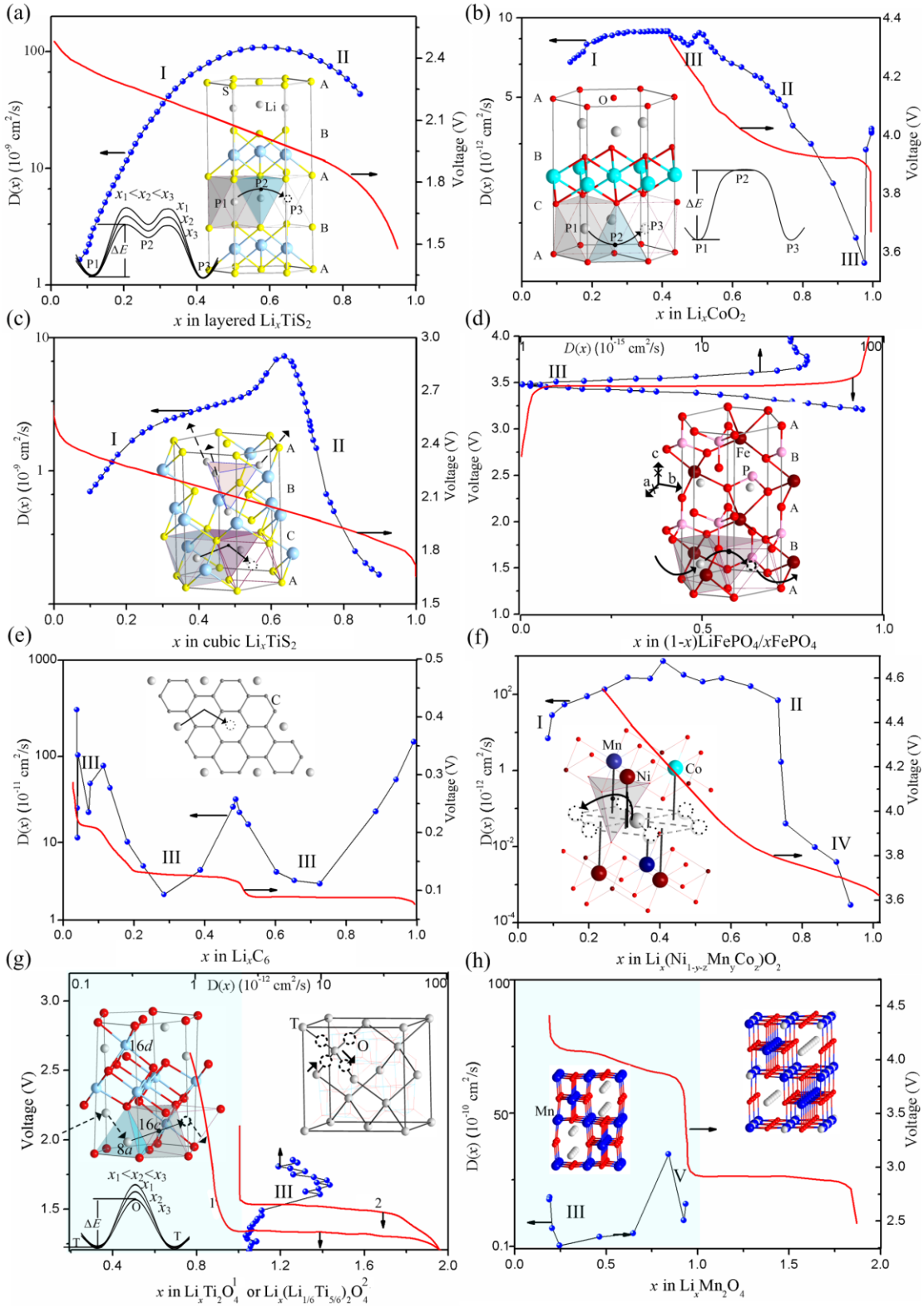

Figure 2. Measured $D(x)$ and voltage (V) as a function of x with the representative migration pathways for different electrode materials. The numbers I (see Section 2.2), II (Section 2.3), III (Section 3.1), IV (Section 2.3.2), V (Section 2.3.3) have been

assigned to the trends of $D(x)$ to identify their corresponding dominant mechanisms. T and O in (g) denote the tetrahedral and octahedral sites, respectively. Data of D(x) were obtained from (a)[54], (b)[55], (c)[56], (d)[57], (e)[58], (f)[59], (g)[60], (h)[61]. Data of V(x) were obtained from (a)[62], (b)[63], (c)[64], (d)[65], (e)[66], (f)[67], (g)[68], (h)[39].

When the concentration x is increased, the site energies of the guest ions along the migration route will be changed due to the extra interactions introduced from the newly added charged particles. It is possible to separately consider the influences of the interactions on the equilibrium and activated states based on the definition of migration barrier. The influences on the value of D come from the extra interactions can be classified as the changes of the interactions among the guest ions, interactions among the host cations and ions, site energies of ions induced by the coordination distortion, and the favorable pathways induced by the local vacancy concentrations around the intermediate sites. The effectiveness of these factors may vary with the system, leading to the different profiles of $D(x)$ curves with the dominant mechanisms being identified in each monotonic interval of x. These mechanisms will be discussed in the following parts.

2.2. Interionic repulsion effects

Given a specific host structure, incorporation of guest ions and electrons needs to redistribute the charge population between the host anions and cations to stabilize the configuration. Supposing the ideal case, in which each new guest ion can gain the same stabilization in terms of energy from the host, the extra repulsive interactions among the newly added ions and the pre-existing ones will inevitably decrease the stabilities of overall guest ions, as embodied by increasing the energies of ions at their stable occupation sites. It may lower the migration barrier by pulling the energy at the equilibrium site upward. If the energy at the activation site undergoes a smaller change compared with that at the equilibrium site, it should give the prediction that

concentration-dependent diffusion should become easier when the concentration of ions is increased.

As studied in layered Li_xTiS_2, the stabilities of ions at the equilibrium sites can be correlated with their chemical potential. According to the Nernst equation,[69] the Li chemical potential $\mu_{Li}^{cathode}$ as a function of concentration x in a cathode can be directly accessed from the open cell voltage $V(x)$ according to $V(x) = -(\mu_{Li}^{cathode}(x) - \mu_{Li}^{reference})/e$, where $\mu_{Li}^{reference}$ is the constant Li chemical potential in the bulk Li reference electrode and e is the magnitude of electron charge. Experimental V(x) curves[62] show a nearly linear drop of voltage with x, indicating a decreasing stability of Li with concentration and a single-phase solid-solution behavior (See Figure 2(a)). However, this trend cannot ensure the decrease of migration barrier because it is not clear about the site energy at the activated state. Calculated energy profiles[70] along the migration path with different ion concentrations (see Figure 2(a)) in Li_xTiS_2 show a decreasing trend of migration barrier and a nearly consistent barrier height between the intermediate (P2 in Figure 2(a)) and activated states with increasing x, indicating that the activated state is more insensitive to the concentration than the equilibrium state in this case, which proposes that the dominating factor to control the concentration-dependent diffusion is the stability of Li changed by the increased interionic repulsive interactions. The newly added ions sometimes can induce an expansion of c-lattice parameter in the layered structure, such as in the Li_xTiS_2 with the c-axis value increased from 5.7 (x=0) to 6.2 Å (x=1),[71] giving the associated effect with the decreased ion stability. The increasing trend of $D(x)$ predicted by DFT[70] can be observed in the experimental results (see Figure 2(a)) of Li_xTiS_2 in the low concentration range. This ionic-stability-dominated mechanism (denoted by I in Figure 2) can also be applied to the observed $D(x)$ curve on Li_xCoO_2 (x<0.4) (see Figure 2(b)). In this range, Li_xCoO_2 also accompany a significant c-lattice increase from 12.88 (x=0) to 14.42 (x=0.4).[72] A deceasing trend of migration barrier with x has also been confirmed through DFT calculations for Li_xCoO_2.[73] Current

research mainly focuses on this deep delithiation stage for increasing the upper work voltage over 4.2 V.[74] Many studies believe the small diffusion coefficient of Li at low Li content and structural instability may be responsible for the capacity failure of Li_xCoO_2 at high voltage. Therefore, multiple doping is developed as an effective strategy to modify the reaction kinetics of Li_xCoO_2 at high cutoff voltage. For example, it has been demonstrated that Al doping can effectively improve the structural instability.[75] Not only limited in the layered structure, this mechanism is also suitable for the case of cubic Li_xTiS_2 in the low concentration range (see Figure 2(c)). Both DFT calculations[76] and NMR measurements[77] have provided the evidences that the migration barrier in cubic Li_xTiS_2 also exhibits the decreasing trend with x. On the other hand, the deceasing trends of $D(x)$ with x in layered and cubic Li_xTiS_2 in the high concentration ranges (see Figure 2(a) and 2(c)) pose the possibility that some other competitive mechanisms should exist to control the concentration-dependent diffusion as discussed below.

2.3. Pathway dependence

If we transfer our attention from the equilibrium to the activated state, it can be found that the local vacancy concentration around the intermediate site along the migration pathway may influence the site energy of the activated state under a specific concentration. As confirmed from DFT calculations[70] and NMR results,[78] a preferred pathway for Li diffusion in layered Li_xTiS_2 is connected by two octahedral sites through an intermediate tetrahedral site (see Figure 2(a)). There are two different local vacancy configurations can be chosen along the path as shown in Figure 3(a). Lithium ion prefers the high local vacancy-concentration direction with a lower migration barrier (path 1) to move, as compared with that of path 2. Investigating the difference in interaction between the two paths can find that the low vacancy concentration around the intermediate site can introduce extra repulsive interactions among the neighboring pre-existing and the migrating ions. It exerts a much more significant influence on the activated state by pulling its site energy upward compared with the

equilibrium site, leading to an increase of migration barrier and providing the guidance for the ionic hopping direction. This correlated result can be regarded as another effect on ion diffusion generally refereed by the vacancy-cluster-dominated mechanism as denoted by II in Figure 2.[52] The microscopic kinetic effects induced by the vacancy concentration may be derived from the different local lattice strains. This mechanism predicts that the ionic diffusion process may become more difficult under the high ion-concentration condition due to the decrease of local vacancies along the pathway. The decreasing trend of $D(x)$ with x in layered Li_xTiS_2 at the high concentration range (see Figure 2(a)) indicates the dominant factor is gradually changed from the ionic stability to the vacancy cluster. This dominant effect is more pronounced in the cubic Li_xTiS_2 phase as the local vacancy concentration increases from two to three under the cubic configuration (see Figure 3(b)).[76] The mechanism can also be applied to the system of Li_xCoO_2 ($0.6<x<0.75$) to explain the decreasing trend of $D(x)$ curve because it has the similar 2-dimensional (2D) octahedron-tetrahedron-octahedron (O-T-O) pathways[73, 79] as exhibited in the layered Li_xTiS_2. It seems that this competitive mechanism should always be responsible for the decreasing trend of $D(x)$ in a high-concentration region under the single-phase condition, but it should be invalid if the migration pathway has only one choice, such as in the case of $LiFePO_4$ as discussed below. It brings forward the requirement to classify the pathway-dependent diffusion processes.

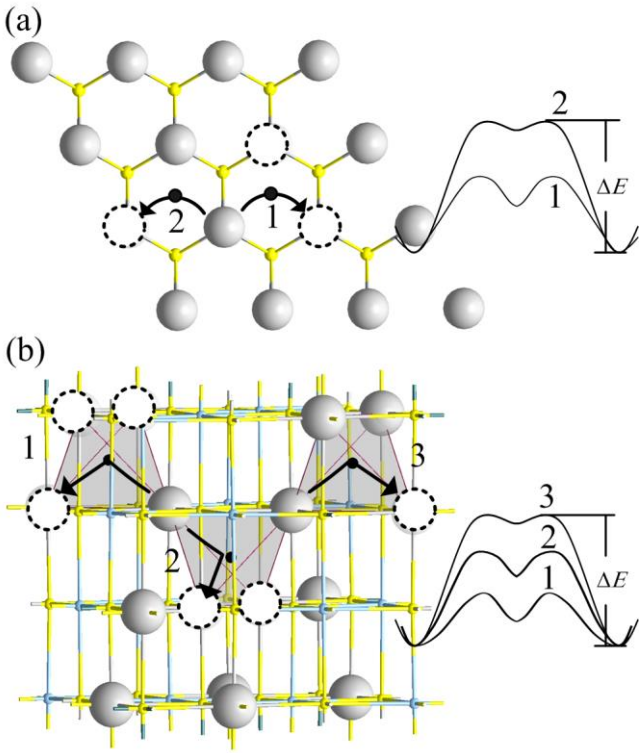

Figure 3. Migration barriers along the pathways with different local vacancy concentrations around the intermediate sites in layered (a) and cubic (b) structures of Li_xTiS_2, data collected from Refs.[70, 76].

2.3.1. 1D channel

Many intercalation compounds are formed by anions (O or S) sublattice stacked along the specific crystallographic direction with repeated configurations of *ABAB* sequence (see Li_xTiS_2 in Figure 2(a) and $LiFePO_4$ in Figure 2(d)), which is usually denoted by O1 structure (CdI_2 type), or *ABCABC* configurations (see Li_xCoO_2 in Figure 2(b) and cubic Li_xTiS_2 in Figure 2(c)), which is usually denoted by O3 structure (α-$NaFeO_2$ type).[80] Transition metal cations or guest ions can be filled into the octahedral or tetrahedral interstitial sites surrounded by the anions. The ordered arrangement of transition metal ions usually gives rise to the layered structure and 2D available sites for the guest ions. Disordered occupation of cations can lead to the cubic structure with 3D available interstitial network distributed among the O3 configuration, usually producing the spinel or disordered rocksalt cubic structure.

Detailed description about these structures and transformations can be found elsewhere.[34, 80-83] According to the available pathways for the ionic movement, these structures can be classified into the host 1D channels, 2D channels or planes, and 3D channels and spaces.

Movement of ions in 1D channel can exist in the olivine $LiFePO_4$, which has been confirmed through DFT calculations combined with molecular dynamics (MD) simulations.[84-87] A direct evidence for Li^+ ion transport in a zigzag pathway (see Figure 2(d)) along the *b*-lattice direction of $LiFePO_4$ has been provided through the neutron diffraction experiment.[88] Geometrically, Li^+ ion located at one energetically favorable octahedral site can pass through a tetrahedral site (along *b* axis) or an octahedral site (along *c* axis) to the other octahedral site, but the migration barrier along the *c* axis is over 5 times larger than that along the *b* axis,[85-87] thus inhibiting the ionic movement along this path. Some defects, such as antisite Fe_{Li},[85, 89] may distribute along the channel, and then impede the transport of ions.[90-91] As embodied from the low diffusion coefficient (Figure 2(d)),[57, 92-93] intrinsic 1D channel in bulk state accompanied with the favorable defects leads to a decreased ion mobility compared with other cases. Furthermore, the multiple trends in $D(x)$ can neither be ascribed to the ionic stability nor to the vacancy cluster. The reason is that a commonly accepted two-phase reaction controls the Li^+ ion insertion/extraction processes in $FePO_4$/$LiFePO_4$.[94-95] Many different models[94-99] describe the two-phase reaction as that one phase in the bulk state grows at the expense of the other without the presence of continuous solid-solution state Li_xFePO_4 at room temperature. Lithium transport involves the kinetic processes[100] influenced by the two-phase boundary of $FePO_4$ and $LiFePO_4$ (see Section 3). Hence, the measured values of $D(x)$ can not be employed to predict the rate capability of $LiFePO_4$. As evidenced by the surface modified nanoparticles of $LiFePO_4$ with large-ratio coating of carbon,[1] over 60% of the theoretical capacity can be maintained at 200C rate, which is over most of the intercalation electrode materials that have larger measured bulk-diffusion coefficients than $LiFePO_4$. Therefore, the improved rate performance should not

benefit from the bulk diffusion in single phase, but from the size effects (see Section 4) and its special two-phase boundary kinetics with the assistance of the transferred electrons (see Section 3 and 5).

Another typical 1D channel system is MnO_2. MnO_2 has a large number of polymorphic structures,[101] usually exhibited as the fine-grained and amorphous states under the natural condition.[102-103] As shown in Figure 4, 1D channels exist in their specific α (hollandite type), β (rutile type), ramsdellite-type, and γ phases (intergrowth between rutile and ramsdellite types). The δ (layered type) and λ phases (spinel type) have been categorized into the high dimensional channel systems because their configurations can form 2D and 3D networks. The 1D channels have been classified into 1×1 (β), 1×2 (γ, ramsdellite), and 2×2 (α) tunnels according to the number of octahedral units in the cross section. Some electrochemical experiments have provided the evidences that the 1×1 tunnels are difficult to accommodate any significant quantities of Li,[39] thus against the availability of crystalline β phase in the bulk state as an insertion electrode. Note that the nanoparticles of β phase can give different electrochemical behaviors in contrast with the micrometer-sized ones.[104-107] γ-MnO_2 has gained success for its application in primary batteries.[108] Li diffusion in γ-MnO_2 generally can be characterized by using the ramsdellite phase because it can be regarded as a mixture of 1×1 and 1×2 tunnels. As confirmed by DFT calculations,[109] the equilibrium site for single Li in the 1×2 tunnels is located in the tetrahedral site in the dilute state and will be moved to the octahedral site if two Li are simultaneously inserted into the block under the high-concentration condition (see Figure 4(c)). The pathways follow a zigzag line of T-O-T-O-T with a smaller migration barrier under the dilute Li concentration compared with the migration of Li under the high-concentration limit in a single-channel pathway of O-T-O. Therefore, concentration-dependent Li diffusion in the 1×2 tunnels under the ideal solid-solution condition should become difficult in the high-concentration condition due to the vacancy-cluster-dominated mechanism discussed in section 2.3. This predicted decreasing trend in $D(x)$ curve is consistent

with the experimental results.[110] Note that the nearly full lithiation of ramsdellite MnO_2 can expand the cell volume anisotropically over by 21%, which usually results in the poor reversible structural kinetics for the high-concentration case, so it is difficult to accurately measure the concentration-dependent value of *D*. In the primary batteries of MnO_2, the guest ions usually involve protons instead of Li^+. Observations on diffusion coefficients of protons in different types of MnO_2[111] gave the evidences that support the similar decreasing trends as shown in Figure 4. Detailed study on the diffusion processes of protons in γ-MnO_2 may be generalized to the other types of ions.[108, 112] For example, three types of protons have been identified as the water related protons with superior mobility, surface bonded species, and localized protons assigned to the particular sites in the lattice, respectively.[113] Correspondingly, three sequential steps can be observed in the reduction voltammogram during the negative scanning process with the Mn reductions at the surface sites, 1×2 tunnels, and 1×1 tunnels, respectively. The measured diffusion coefficient of protons ranged from 10^{-10} to 10^{-16} cm^2/s due to the ambiguities of measured proton types and the active surface areas.[108, 111, 114] It is believed that the smaller value should be the characteristics of proton diffusion in the channels, and the larger value may come from the surface contribution. The accumulated knowledge on the proton diffusion in MnO_2 boosts the study on aqueous secondary batteries based on the Zn/MnO_2 electrodes.[115-120]

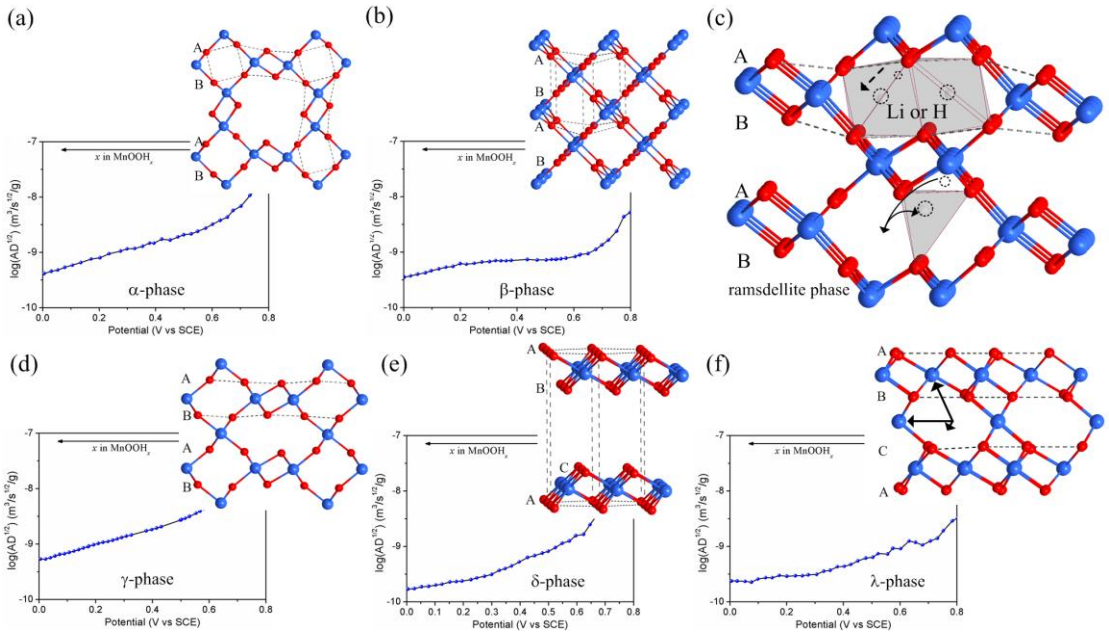

Figure 4. Structures of MnO_2 in different polymorphic states and the measured diffusion parameters ($AD^{1/2}$, where A represents the specific surface area) of protons in their corresponding host structures, where the data of $AD^{1/2}$ were obtained from Ref.[111]. (a) α phase, (b) β phase, (c) ramsdellite-type phase, (d) γ phase, (e) δ phase, (f) λ phase.

The large tunnels, such as in the α phase, can easily accommodate a wide range of cations (such as Na^+, K^+, Rb^+, Ca^{2+}, Ba^{2+}, Pb^{2+}, NH^{4+})[102, 121-123] accompanied by water molecules as the pillars through charge balance of partial Mn^{4+}/Mn^{3+} to stabilize the stress in the spaces. This feature seems to be more appealing to the ion intercalation compared with the small tunnel system. By comparing the migration barriers in the ideal empty channels in α (0.1 eV)[124] and ramsdellite phases (0.2 eV),[109] it has been concluded that Li diffusion in the large empty channels should be easier than that in the smaller ones, but this advantage with the absence of pillars needs a tradeoff between the cycling stability and diffusion in the real case. The structural stability of α-MnO_2 needs introducing cations or Lithium oxide (such as Li_2O) to stabilize the large tunnels.[39] These cations also play the role of blockers to impede the diffusion of Li in the channels. On the other hand, comparative studies of different phases of nanoparticles MnO_2 on the capacitive behaviors gave the specific capacitances in the order of α>γ>β, and then confirmed the intrinsic superiority of large tunnels used in the supercapacitors after excluding the specific surface-area effect.[125] This advantage benefits from the different intercalation processes in aqueous electrolytes according to the following proposed charge storage mechanism:[126-129]

$$MnO_2^{bulk/surface} + M^+ + e^- \Leftrightarrow MnOOM^{bulk/surface} \ (M = Li^+,\ Na^+,\ K^+,\ \text{or}\ H_3O^+)\,,$$

where alkaline metal ions and protons are believed to be involved in the processes under the presence of water. The bulk insertion/extraction were observed that are only pronounced in the nanoparticles morphology compared with the thick composites.[126] Water molecules (see Section 5) and size effects (see Section 4) can trigger the more superior kinetic processes in contrast with the solid-state diffusion in Li-ion batteries.

In addition, the other dominant mechanisms denoted by III (Section 3.1), IV (Section 2.3.2), V (Section 2.3.3) in Figure 2 will be discussed in the following sections.

2.3.2. 2D channel

2D channels can be classified into two types. One corresponds to the ions populated in the interlayer space without the anion-coordinated interstitial sites on the planes. The other corresponds to the ions populated at the interstitial sites in the 2D planes formed by the anion sublattice.

For the first type, a typical representative system is graphite (see Figure 2(e)).[130-132] Previous DFT calculations have shown that penetrating a carbon honeycomb from one layer to another is energetically unfavorable for Li^+ ions (approximately 8~10 eV).[133-134] The favorable occupation site of Li in graphite is at the center of six-carbon ring. Diffusion pathway is connected by the three central sites through two ring walls with a migration barrier no more than 0.5 eV (see Figure 2(e)).[27, 135] It was evidenced that the diffusion of Li along the *c*-lattice direction in highly oriented pyrolytic graphite (HOPG) is limited by the number of grain boundaries,[27] so the diffusion of ions in graphite may give a large control to the grain boundaries as well as their orientations. These morphology-dependent diffusion properties lead to the uncertainty of Li diffusion coefficients in graphite varied from 10^{-6} to 10^{-16} cm^2/s.[27, 136] However, the concentration dependent diffusion coefficient can still be observed in the film samples. As shown in Figure 2(e), it gives the multiple trends of diffusion coefficient with x in Li_xC_6 ($0<x\leqslant 1$) measured from the thin-layer graphite.[58] In the literature, it is well-admitted that the intercalation compound Li_xC_6 follow the stage-sequence variation with x according to: dilute stage 1 → stage 4 → stage 3 → stage 2 → stage 1,[137] where stage n correspond to the phase configuration with n host layers placed between two successive Li layers (such as stage 2 ($Li_{0.5}C_6$) can be denoted by $AA\alpha AA\alpha$,[138] and stage 1 (LiC_6) by $A\alpha A\alpha$[139], where A and α represent the C and Li layers, respectively). Each transformation between two stages always includes

intermediate multiple phase compositions. In contrast with the profile of V(x) (see Figure 2(e)), it can be found that concentration-dependent Li transport in the interlayer space of graphite should follow the phase-dependent process (see Section 3).

Intuitively, as a single layer of graphite, graphene should transform the sequential bulk diffusion of ions to the simultaneous surface adsorption with an increased accumulation rate. However, DFT calculated Li adsorption capacities on pristine graphene provoke a controversy,[140-144] showing a large range from zero adsorption with respect to the metal bulk Li,[140-141] to the Li_xC_6 ($0<x\leq6$) with respect to the isolated Li atom.[142-144] Some experimental results obtained from different morphologies of graphene also provided a large measured range of reversible specific capacities from 460 to 800 mAh/g over the theoretical capacity of graphite (372 mAh/g).[145-147] In conflict with that, the decreased adsorption capability of graphene compared to graphite has also been reported.[148] Some researchers believe that the reversible Li storage capacity of pristine graphene may be not superior to graphite due to the repulsive interactions among the guest ions while they are uniformly distributed (decreasing the capacity), or due to the possible Li cluster effects on the graphene surface while they are aggregated and staggered together (decreasing the cycling capability). However, the defect- and edge-dominated mechanisms can significantly enhance the adsorption and diffusion capabilities of Li, accounting for the large measured capacity values.[140-141, 143, 146, 148-149] It is fortunate that this adsorption controversy should not bring significant influence on the diffusion processes because the migration barrier only depends on the energy difference along the pathway. As a representative 2D material, diffusion of ions on graphene not only involves the surface sequential diffusion process in the restacking configuration as behaved in graphite, but also includes the surface adsorption process as behaved in the porous hard (non-graphitizable) carbon[150] for an electric double layer capacitor (EDLC) in the monolayer or bilayer structure. For the part of sequential diffusion, it has been reported that the edges of graphene with different functional groups (such as –O, –OH,

–H),[151-152] and defects (such as vacancies, Stone-Wales defects, dopants)[143, 153-155] in the interior region, are inclined to become stable cluster centers to trap ions. These disordered defects can diversify the activate states and migration pathways around these areas. DFT calculated results predicted that these centers generally can facilitate the diffusion of ions with lowered migration barriers. Cyclic voltammetry experiments conducted on graphene with the improved rate performance seems to support this conclusion, but the large irreversible capacities[153] indicate that the improved diffusion capability may be only available for the shallow trapped ions, not working for the deep trapped ones. The edge-trapped effects also provide the evidences that it is convenient for the intercalation processes in graphite from the edge to the interior.[151-152, 156] Note that it has been demonstrated that the rate capability of graphite could be effectively boosted by taking full advantage of diffusion kinetics of Li in graphene. For example,[157] a sample of bilayer graphite (or bilayer graphene) shows a faster diffusion of Li than in bulk graphite and even surpassing the diffusion of NaCl in liquid water. The measured diffusion coefficient can reach as high as 7×10^{-5} cm^2/s. The results indicate that the sample acts as a single-phase mixed conductor with a high electronic and ionic conductivity. These properties can be generalized to the other 2D-structure materials to describe the effects of the non-periodic species (defects and edges) on the microscopic ionic diffusion processes.

For the second type, typical 2D-limited electrode materials include layered Li_xMO_2 (M=Co, Ni, $Ni_{1-y-z}Mn_zCo_y$) with O3 structure,[158-159] and layered Li_xTiS_2 with O1 structure as mentions before (see Figure 2). In addition to the diffusion dependence on the local vacancy concentration in these configurations, the species of transition metal and anions can also introduce different influences on ion transport. According to the intercalation voltage of $LiMO_2$: Co^{3+}/Co^{4+} (~3.9 V by experiment,[160] 3.75 V by calculation[161]), Ni^{3+}/Ni^{4+} (~3.6 V,[162] 2.92 V[161]), Li chemical potential in $LiCoO_2$ is lower than $LiNiO_2$. This difference mainly results from the lower redox energy level of Co^{3+}/Co^{4+} (belonging to the t_{2g} orbitals) relative to that of Ni^{3+}/Ni^{4+} (e_g orbitals) as shown in Figure 5(a). Thus, in the migration-energy profile of $LiCoO_2$, the

equilibrium-site energy should be lower than that in $LiNiO_2$, but the calculated migration barriers of $LiCoO_2$ and $LiNiO_2$ have nearly the same values under the supposed same lattice parameters.[163] It means Li-ion energies at the activated sites follow the consistent trend with the equilibrium sites, leading to the negligible influence on the diffusion barrier. Note that this conclusion should be only available in the full lithiation state under the ideal identical structure of $LiMO_2$ (M=Co, Ni) with the same lattice parameters. In the real cases, multiple-stages phase transformations accompanied by different extent of expansion and contraction of c-lattice parameters will proceed in Li_xMO_2 ($0<x\leqslant 1$, M=Co, Ni) with increasing x.[164-166] These processes can result in different phase-transformation-dependent diffusion properties (See Section 3). In addition, Li_xNiO_2 is more thermally favorable to form the antisite-defect structure referred by $Li_{1-x}Ni_{1+x}O_2$ with Ni randomly occupying the Li sites,[167] which can impede the migration of Li[168] and can lead to the weaker diffusion capability of Li in contrast with Li_xCoO_2 as confirmed from the NMR measurements[169] and rate-dependence results.[170] A larger value of D (~10^{-7} cm^2/s) over Li_xCoO_2 has been reported for Li_xNiO_2 with nearly ideal stoichiometric composition.[171] In the alloy structure of $Li_x(Ni_{1-y-z}Mn_zCo_y)O_2$ (NMC), the redox couples follow the sequence of $Ni^{2+}/Ni^{3+} \rightarrow Ni^{3+}/Ni^{4+} \rightarrow Co^{3+}/Co^{4+}$ to oxidize with increasing voltage (see Figure 5(a)).[172] The nonreactive behavior of Mn^{4+} observed in NMC is due to the donation of electrons to the lower level of Ni^{2+}. These multiple valences configurations result in a more disordered migration-barrier distribution in the Li-occupation layer (see Figure 5(b)).[173] It can overwhelm the phase-controlled diffusion process and lead to the trend of concentration-dependent diffusion in the solid-solution state similar with Li_xTiS_2 as shown in Figure 2(f).[59, 67] Investigation on the kinetic behavior of NMC based on a single-particle sample has suggested that the combination of interfacial reaction and bulk diffusion (denoted by IV in Figure 2(f)) and complete bulk-diffusion-limited processes are dominant in the high and dilute Li-concentration cases, respectively,[174] which may account for the significant decreasing trend in $D(x)$ of NMC at the high-concentration region. The obvious decreasing trend in this region also corresponds to a sharp rise of charge-transfer

resistance for the interfacial reaction with x at the high-concentration region as observed in $LiCoO_2$ through electrochemical impedance spectra (EIS).[175] It gave an indirect support for the kinetics transformation at the high-intercalation level in this system. The reason for this change of kinetics can be expected to be induced from the increase of resistance for the electron transport in NMC with the increasing x, because the electronic resistance can be increased by over 5 orders of magnitude in the high-concentration region,[176] which can slow down the interfacial reaction as exhibited in the bulk state of $LiFePO_4$ (see Section 4 and 5).[177] On the other hand, although some analogies have been exhibited between Li_xTiS_2 and NMC, the intrinsic diffusion capabilities in these systems should be different due to the different redox couples and anions. The higher redox levels in Ti pinned with anion S p-bands than M (M=Mn, Ni, Co) with O p-bands in NMC result in the decreased redox-voltage range in Li_xTiS_2 (see Figure 5(a) and Figure 2). This deceased intercalation voltage also indicates a weaker stability of Li trapped in Li_xTiS_2 relative to Li_xMO_2. In addition, larger atomic distances between the Li^+ ions and host cations in Li_xTiS_2 have also been observed in contrast with Li_xMO_2,[163] which can result in the weaker repulsive influence of host cations on the activated states. These factors can lead to a better intrinsic Li-diffusion capability in Li_xTiS_2 than in Li_xMO_2 under the condition of solid-solution state based on the ionic-stability-dominated mechanism. The experimental measurements also usually gave the larger values of diffusion coefficient in Li_xTiS_2 than in Li_xMO_2 as shown in Figure 2. This feature seems to be more general for the anode that usually has better intrinsic bulk-diffusion capabilities of ions than the cathode in the layered intercalation system without considering the passivation layer at the interface.

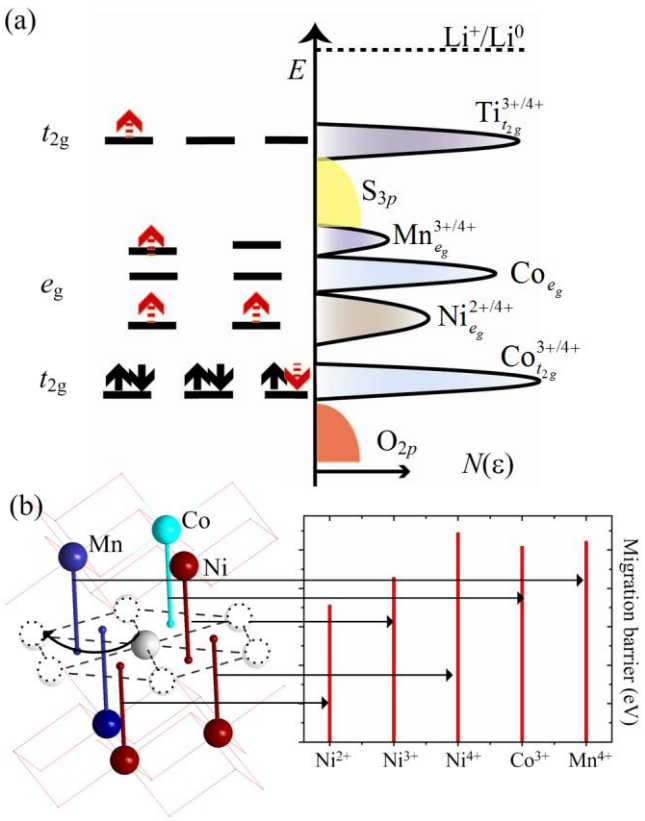

Figure 5. (a) Schematic of the possible electronic contribution of transition metal *M* (*M*=Co, Ni, Mn) and Ti to the densities of states of Li_xMO_2, NMC and Li_xTiS_2, data obtained from Ref.[31, 172]. (b) Migration barriers in NMC along the pathways surrounded by different types of cations, data obtained from Ref.[173].

2.3.3. 3D channel

Like in the case of 2D channels, 3D channels can also be classified into two types of pathways. One corresponds to the crosslinked channels connected by the coordinated sites in the 3D space. The other corresponds to the 2D planes with large interlayer spaces supported by pillars that allow the ions to move in the 3D continuous spaces.

Typical configuration of the first-type 3D channels exists in the spinel structure. The representative systems include isostructural $Li_xTi_2O_4$ and $Li_xMn_2O_4$ ($0<x\leq2$). In the system of $Li_xTi_2O_4$ under the low-concentration condition ($x<1$), the energetically

favorable sites for Li are tetrahedral interstitials with the octahedral sites acting as the intermediate connection points in the migration pathways (see Figure 2(g)). Increasing the concentration of Li within the range of $0<x<1$ gives rise to a solid-solution configuration with Li gradually filling up the tetrahedral sites as indicated in the V(x) (x<1) curve[68] (see Figure 2(g)). Repulsive interactions among the guest ions play the dominant role of controlling the concentration-dependent diffusion in this region as confirmed by DFT calculations.[178] It leads to the decreasing migration barrier with increasing Li concentration (see Figure 2(g)). A significant feature differing from the layered structure is that the insertion/extraction of Li^+ ions are usually accompanied with negligible variations of lattice parameters due to the large mechanical tolerance of this system, especially in the $Li_x(Li_{1/6}Ti_{5/6})_2O_4$ (usually referred by $Li_4Ti_5O_{12}$) composition.[179-181] $Li_x(Li_{1/6}Ti_{5/6})_2O_4$ can be denoted by $(Li_x)_{8a}[(Li_{1/6}Ti_{5/6})_2]_{16d}O_4$ to identify the occupations (see Figure 2(g)), where 8*a* and 16*d* are the Wyckoff notations to represent the tetrahedral and octahedral sites in the spinel structure. The excess Li in the 16*d* sites make it more durable for the cycling of guest Li^+ ions. While x is increased from 1 to 2, the intermediate octahedral sites (16*c*) gradually become the equilibrium sites for the Li occupation. Full lithiation can transform the structure of $(Li)_{8a}[Ti_2]_{16d}O_4$ (tetrahedral occupation) to $(Li_2)_{16c}[Ti_2]_{16d}O_4$ (octahedral occupation) configuration. According to the diamond-type network formed by the tetrahedral 8*a* sites as shown in Figure 2(g), the strong repulsive interactions between the excess octahedral Li (16*c*) and the initial tetrahedral Li (8*a*) will push the Li^+ ions to move from the tetrahedral to the nearest-neighboring octahedral sites through the two-phase reaction process during the range of $1<x<2$, as indicated by the plateau in the V(x) curve (see Figure 2(g)). Under the condition of x>1, it can be found that the short diffusion distance and multiple pathways between the tetrahedral and octahedral sites, combined with the lower stabilities of the ions ($\mu_{Li} \approx 1.34$ eV in $Li_{1+y}Ti_2O_4$ and 1.56 eV in $Li_{1+y}(Li_{1/6}Ti_{5/6})_2O_4$, where $x=1+y$ and $0<y\leq1$)[68] relative to the layered Li_xMO_2, result in the intrinsic advantages in Li diffusion capability in this two-phase mixture. This superiority has been proved by the

highly reversible Li-excess anode materials $Li_{1+y}(Li_{1/6}Ti_{5/6})_2O_4$ as indicated by the very stable diffusion coefficient as a function of x (see Figure 2(g))[60] even under the two-phase-boundary-dominated mechanism (see Section 3). However, the state-of-the-art $Li_4Ti_5O_{12}$ performance cannot satisfy the high capacity demand. The challenge requires constructing the stabilized and reversible electrode architecture by employing the improved phase transition kinetics of overlithiation, such as the reported heterogeneous phase $Li_4Ti_5O_{12}$-rutile TiO_2 composite electrodes, which has the potential to reach the theoretical capacity beyond 250 mAh/g.[180]

A similar first-order transition can also be observed in $Li_xMn_2O_4$ from the spinel $LiMn_2O_4$ (λ-MnO_2) to the rocksalt $Li_2Mn_2O_4$ with tetragonal symmetry as indicated by the constant voltage plateau in the V(x) curve near 3 V (see Figure 2(h)).[39, 182] A two-phase reaction process moves progressively from the surface into the bulk region, validating the phase-dependent diffusion process. However, differing from $Li_xTi_2O_4$ with the solid-solution state while x<1, a phase-transition process can be observe in the spinel $Li_xMn_2O_4$ (x<1) before x=0.5, which triggers the disorder-order phase-dependent diffusion process near this concentration area (see Section 3) due to the formation of ordered occupation of Li at one half of the 8a sites in $Li_{0.5}Mn_2O_4$.[183-184] Under the dilute condition, many experimental results have shown a decreasing trend of $D(x)$ in $Li_xMn_2O_4$ with increasing x (see Figure 2(h)) while x<0.5 due to the two-phase boundary effects (see Section 3).[61, 185-187] A decreasing trend of $D(x)$ can be found while x is close to 1. Local vacancy-cluster-dominated mechanism can be excluded in this case because each intermediate octahedral site can only be connected by one pair of tetrahedral sites (see Figure 2(g)). The intermediate states may be the local minima or maxima. In this structure, the octahedral sites act as the activated states instead of the local minima. There are four equivalent intermediate octahedral sites for each tetrahedral site to choose to pass over, but the barriers are not equivalent. It has been found that different valence states of host cations around the activated states can significantly influence the migration barriers (see Figure 6).[188] Lower barriers can be obtained under the Mn^{4+} rich condition compare with the Mn^{3+}

rich condition. This feature can lead the ion to give preference to the pathway with the octahedral site surrounded by more Mn^{4+}. Moreover, experimental and DFT calculated results have provided the evidences that suppressing the reduction of Mn^{4+} in $Li_xMn_2O_4$, such as by doping the lower valence-state cations, can lead to the improved rate capability of doped samples.[189-192] Furthermore, $LiMn_2O_4$ samples doped by M (M=Co, Ni, Fe, Cr, Al) have also been synthesized to investigate their electrochemical performances. The results show much better cycling stability of the doped samples compared with pristine $LiMn_2O_4$. For example, $LiMn_{1.85}Cr_{0.15}O_4$ demonstrated the high capacity retention of 96.6% after 100 cycles, surpassing the referenced value measured in $LiMn_2O_4$ phase over 23%.[193] The enhancement of cycling stability is obviously induced by the substitution of M for Mn that can significantly affect the kinetics of microstrain and phase transformation. These results indicate that a cation-valence-state-dominated mechanism (denoted by V in Figure 2) should be responsible for the decreasing trend of $D(x)$ under the high concentration condition by decreasing the local concentration of Mn^{4+} around the octahedral site. The effectiveness of this mechanism can be understood by the Jahn-Teller effect of Mn^{3+}.[188, 194] It can distort the octahedrons and induce the internal strains around the activated site while the averaged Mn oxidation state is close to 3.5, and then make the guest Li more unstable at the activated state, leading to the increase of the migration barrier in this range.

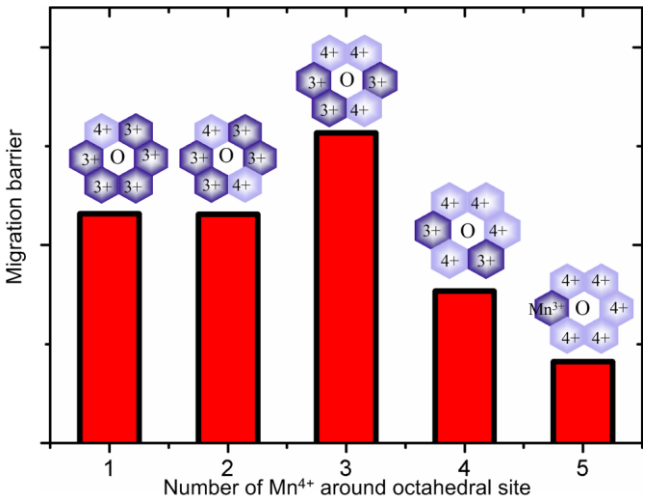

Figure 6. Trend of migration barriers along the pathways with different numbers of Mn^{4+} around the intermediate octahedral site in $Li_xMn_2O_4$ (x<1), data obtained from

Ref.[188].

For the second type of 3D channels, the existence of the continuous 3D space needs some extra pillars to support the atomic layers. One typical system is the layered $Ti_3C_2T_x$,[195-198] where T_x represent the different types of surface functional groups (such as –O, –OH, –F). This system belongs to a large group of 2D layered materials commonly referred by MXenes. They are stacked by $M_{n+1}X_nT_x$ (n=1, 2, or 3) atomic blocks along the c axis of hexagonal unit cell, where X is C and/or N and M denotes the early transition metal (such as Ti, V, Nb). A large variety of cations (such as Li^+, Na^+, K^+, Mg^{2+}, NH_4^+) and polar molecules (such as H_2O, $N_2H_4{\cdot}H_2O$, urea) can be intercalated into the $Ti_3C_2T_x$.[8, 199] The intercalated water molecules and cations,[200] or organic polymer,[201] acting as the pillars,[202] can expand the c-axis value by 5~25 Å. The large interlayer space allow the guest ions to transport in the 3D continuous space under the assistance of water molecules.[200, 203] Different equilibrium sites under the oxygen covered sample $Ti_3C_2O_2$ for the occupation of intercalated alkali-metal cations, protons, and H_2O have been predicted by DFT calculations, which are located on the top of C atoms (close to 2c sites along the c axis), on the top of O atoms (4e sites), and on the top of O atoms (2b sites) in the middle of interlayer spaces, respectively (see Figure 7), where the Wyckoff notations correspond to the symmetry sites in space group $P6_3/mmc$.[203-204] These different initial sites can lead to different 3D migration pathways for alkali-metal cations and protons as shown in Figure 7. Differing from the 2D diffusion in the layered transition-metal oxides, most of the capacity contribution in $Ti_3C_2T_x$ thin film arises from the non-diffusion limited process in the bulk state as confirmed by the experimental results.[199] These non-coordinated sites and intercalated water molecules may invalidate the limiting factors of solid-state diffusion[205-206] as exhibited in the supercapacitor applications (see Section 5). For example,[206] a electrode architecture of macroporous $Ti_3C_2T_x$ MXene was designed for improving the ion accessibility to redox-active sites, which can improve the reaction kinetics to the level of carbon-based materials, as confirmed by the measured capacitance of up to 210 F g^{-1} at scan rates of 10 V s^{-1}.

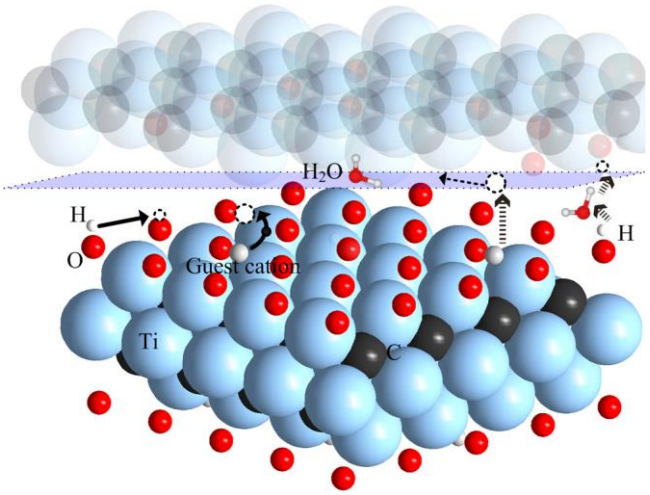

Figure 7. Schematic diagram of the 3D transport pathways for a guest ion and proton in the expanded interlayer space of $Ti_3C_2T_x$ MXene, data obtained from Ref.[203].

The similar behaviors also have been observed in birnessite-type layered Li_xMnO_2 (δ-MnO_2). There are several MnO_2 polymorphs that can exhibit the layered configurations, such as $Li(Li_{1/3}Mn_{2/3})O_2$ (or Li_2MnO_3), monoclinic and orthorhombic $LiMnO_2$.[46, 207-208] Layered $LiMnO_2$ with α-$NaFeO_2$ structure cannot be maintained well after delithiation due to the diffusion of Mn into the Li layers to form the spinel phase.[208] The birnessite MnO_2 (see Figure 4(e)) is a type of layered Li_xMnO_2 with structural water and cations remained in the interlayer space acting as the pillars, which can expand the interlayer distances to over 7 Å. Removal of water can lead to the intrinsic instability as proved by the poor cyclability in this structure during the lithiation/delithiation processes,[209] but this disadvantage does not take effects in the aqueous electrolyte for the supercapacitor applications.[125] As proved by the experimental results of mass-to-charge ratio,[127] the insertion/extraction of cations in different aqueous alkali salts are always accompanied by the change of content of water,[210] indicating the participation of the hydrated ions during the charge transfer processes. An enhanced rate performance exhibited in δ-MnO_2 compared with β-, γ-, and λ-MnO_2 emphasizes the diffusion advantage of the 3D space with the assistance of water in this structure (see Section 5).[125]

3. Concentration dependence of ion transport with phase transformation

3.1. Two-phase boundary effects

Phase transformation nearly occurs in most of the intercalation electrode materials as the concentration of guest ions is being increased.[82, 211] In contrast with the ion diffusion in solid-solution state, phase-transformation-dependent transport processes are not disordered but follow the collective kinetic behaviors under the guidance of symmetry. The symmetry arrangement is the requirement of the principle of energy minimum. The kinetics should be derived from the interactions among the atoms, including the Coulomb force and local strain, vibration, and the space occupation property described by entropy, which should be the reason for the formation of crystal with a specific symmetry structure under a specific temperature. Two types of transformation are usually observed during the charging/discharging processes. One corresponds to the structural transformation of host structure. The other includes the order-disorder or metal-insulator transformation without disturbing the host symmetry. Structural transformation of the host structure usually involves simultaneous movements of the entire host and guest particles along multiple directions. The displacements of host particles from their original symmetry sites to the other ones usually lead to the poor cycling performance, such as the degradations of different types of MnO_2 to the spinel phase during the insertion/desertion processes.[39] An intercalation electrode with good cycling stability generally requires that the host structure (or symmetry) can remain unchanged during the lithiation/delithiation processes and the phase transformation mainly relies on the movements of guest particles through the two-phase coexistence process as stressed below.

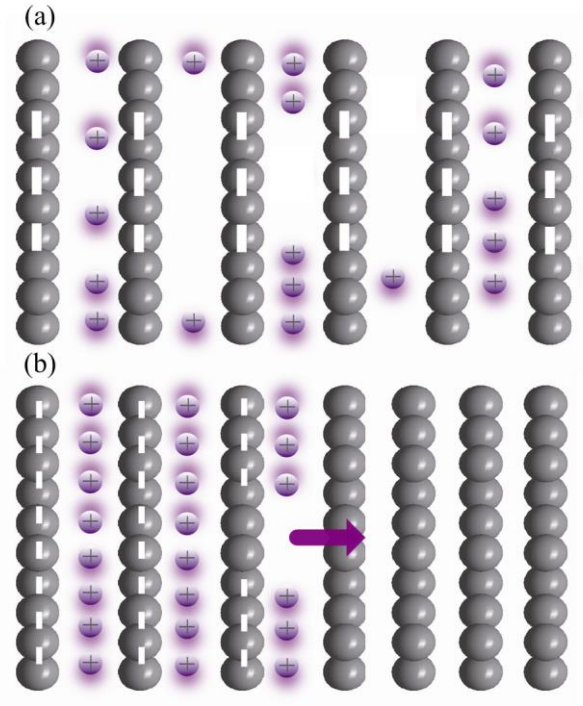

Figure 8. Schematic diagram for the difference between the solid-solution diffusion (a) and two-phase reaction process (b), including the different distributions of electrons and guest ions.

The two-phase coexistence process under the first-order phase transition can be observed in many systems, such as the (1-x)$LiFePO_4$/$xFePO_4$ in the range of $0 \le x \le 1$,[65] the spinel (1-x)$LiMn_2O_4$/$xLi_2Mn_2O_4$ ($x \le 1$),[39] or the Li_xC_6 ($x \le 1$) at different stages.[46] It usually can be observed from the galvanostatic measurement results, corresponding to a large plateau in the voltage curve (see Figure 2). In this case, the averaged chemical potentials μ of guest particles in the two-phase coexistence region are equal to each other, thus invalidating the diffusion coefficient defined in the transformed Fick's first law according to the relationship between the net particle flux J and μ: $J \propto -\nabla\mu$.[52-53] A schematic diagram in Figure 8 can be employed to illustrate a two-phase reaction process in contrast with the solid-solution diffusion process. An isotropic radial shrinking core model has been employed to illustrate the phase-boundary movement process for many systems, such as the graphite intercalation compounds, $Li_xMn_2O_4$ ($x>1$), especially for the evolution process at the

$LiFePO_4/FePO_4$ interface as shown in Figure 9(a).[97] Even though the progressive insertion/desertion of Li^+ ions from the surface to the inner region is conceivable based on the concentration gradient intuition, it still invoked controversy in $LiFePO_4$ because the dominant driving force for diffusion should be changed from $-\nabla\mu$ to the other sources and the 1D diffusion channels in $LiFePO_4$ have anisotropic characteristics. An oriented "core-shell model" has been proposed based on the electron-energy loss spectra (see Figure 9(b))[96, 212] for stressing that the cycling of the composite particles exhibit a $FePO_4$ core covered by a $LiFePO_4$ shell. The kinetics of this model has been supposed and then proved that the movement of Li^+ ion can couple with a hopping electron in a pair in consideration of the poor ionic and electronic conductivities in both $LiFePO_4$ and $FePO_4$ phases.[213] Therefore, the supposed migration sequence of Li^+ ions was proposed to be correlated with the accumulated number of exciton-like Li^+-e^- pairs in the channels and the boundaries between the two phases. Based on these results, the biphase-boundary reaction process and Li-ion migration sequence are modified by another "domino-cascade" reaction model (see Figure 8(b)).[95] They believed that the Li^+/vacancy and Fe^{2+}/Fe^{3+} polarons (see Section 5) localized in the biphase boundaries can destabilize the interfacial zone, leading to the wave-like movement of the interface during the reaction process. The driving force was ascribed to the elastic energy induced from the lattice mismatch between $LiFePO_4$ and $FePO_4$. Many researchers believed that the initial nucleation of the biphase interface should be the rate-limiting step that may start from the areas that have better contacts with the conducting matrix due to the prior electron transfer, as evidenced by the electrode composed of carbon-coated particles with significantly improved rate performance.[1, 214] The transferred electrons play a key role in this case as will be discussed in Section 5. Note that the measured $D(x)$ in this case is usually regarded as the "effective diffusion coefficient" in the literature to embody the two-phase boundary influence on the whole ionic transport process. The reaction process has been classified to the two-phase-boundary-dominated mechanism to clarify the measured trend of the

effective $D(x)$ as shown in Figure 2(d) (denoted by III). It always leads to an abrupt drop of the effective diffusion coefficient from the single-phase diffusion to the two-phase reaction process.

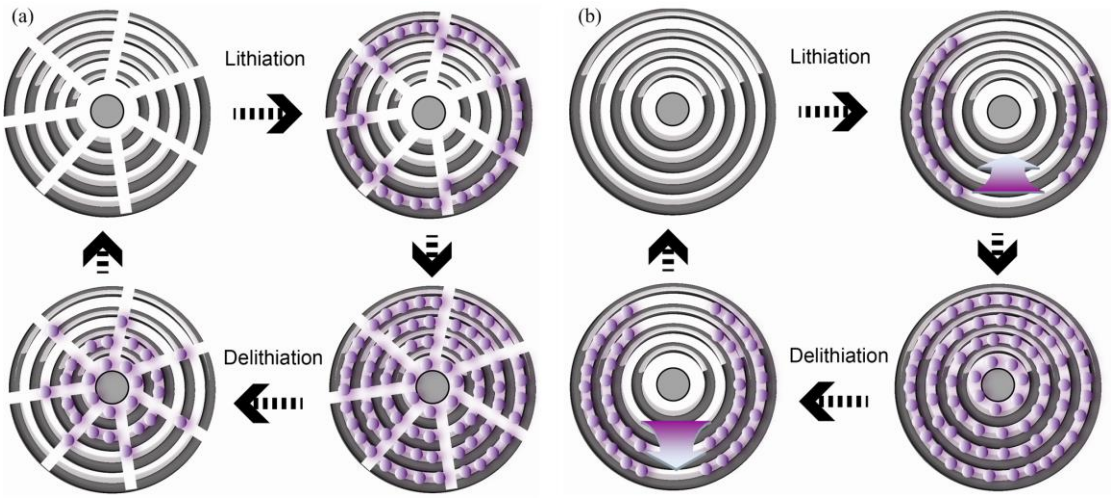

Figure 9. (a) Schematic diagram of the isotropic radial shrinking core model. (b) Schematic diagram of the oriented core-shell model.

Other analogous results of thetwo-phase reaction can be observed in $Li_x(Li_{1/6}Ti_{5/6})_2O_4$ at the region of $x>1$ as shown in Figure 2(g). The abrupt decrease of $D(x)$ near the voltage plateau corresponds to the two-phase coexistence region of $Li(Li_{1/6}Ti_{5/6})_2O_4$ and $Li_2(Li_{1/6}Ti_{5/6})_2O_4$ controlled by the two-phase-boundary-dominated mechanism. In similarity, the reactions of lithium-graphite intercalation compounds also exhibit the nonuniform nucleation and migration processes between the occupied and unoccupied boundaries by Li. Lithium ions are intercalated into the interlayer spaces from the prismatic surfaces of graphite according to the generally accepted stage-formation process from stage 4 to stage 1 as mentioned above (see Figure 10).[215-216] The transformation from stage 3 to 2 is still in a debate due to the lacking of very convincing stage information.[216] There are three two-phase coexistence regions can be observed in the three potential plateaus (see Figure 2(e)), which have been assigned to dilute stage 1 and stage 4, stage 2L (in-plane disorder) and stage 2, and stage 2 and stage 1, respectively.[217] The kinetics of these stepwise processes can be correlated with three types of driving force,

including the driving force between the transferred electrons (or accumulated polarized electrons) and guest ions (type I), the interlayer van der Waals force or structural deformation force (type II), and the repulsive force among the guest ions (type III). Competitive behaviors among these forces can lead to the rate-dependent phase-formation process. As evidenced by the *in situ* synchrotron XRD results under a high current density, the phase stages were suggested to be transformed to the sequence of dilute stage 1 → stage 2 → stage 1 instead of the traditional processes due to the increased contribution of type-I force under the polarization condition (see Section 5).[218] This nonequilibrium phenomenon has also been observed in $LiFePO_4$ system.[219-220] In the equilibrium state without considering the morphology and size effects, three possible rate-limiting kinetic processes have been found, including the insertion/extraction of Li^+ ions at the graphite/electrolyte interface, the two-phase boundary movement, and the diffusion of ions in each single phase, as disputed by different researchers.[217, 221-222] A process controlled by the interfacial reaction at the initial stage and then dominated by the interior ion transport has also been proposed.[95] If neglecting the interfacial effects (see Section 4), the clear decreasing trends can be observed in the measured $D(x)$ at different stages (see Figure 2(e)), indicating that the two-phase coexistence stages can decrease the mobility of Li^+ ions relative to the nearest neighboring single-phase stages in Li_xC_6. These features exhibit the dominant effect of the two-phase-boundary-dominated mechanism compared with the single-phase diffusion and give an enhanced role to the type-II force. It deserves noting that the second plateau in the voltage curve, corresponding to the coexistence of disordered stage 2L and stage 2, follows an order-disorder in-plane transformation process. This type of transformation process can give a general influence on the 2D Li diffusion as discussed below.

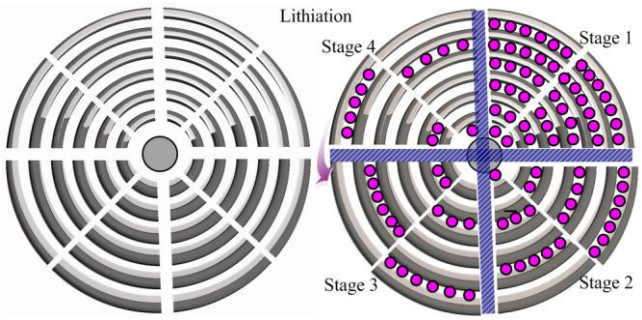

Figure 10. Stage model for the insertion processes of Li into graphite.

3.2. Order-disorder transformation effects

Order-disorder transformation of Li^+ ions on the 2D host sites can be observed in many intercalation systems, such as in Li_xCoO_2,[63] Li_xC_6,[137] or $Li_xMn_2O_4$[183] while x is close to 0.5, Li_xTaS_2 at x=1/3 and 2/3.[223] A more general disordered distribution can lead to the interlayer mixing of all of the cations, such as Li and Ni in the $Li_xNi_{2-x}O_2$.[224] In Li_xCoO_2, the transformation process corresponds to two small plateaus in the voltage curve between about 4.05 and 4.2 V (see Figure 2(b)).[63] The stable ordered in-plane distribution of Li has been confirmed by DFT calculations (see Figure 11).[79, 165, 225] In this concentration range, lithium can move in the 2D planes under the thermodynamic and symmetric guidance just like in the thermal formation process of a crystal, controlled by the long-range cooperative behavior in terms of the symmetry requirement. The transport of ions not only relies on the local variation of ionic concentration, but also correlates with the collective behavior of all of the in-plane ions. It can slow down the movement of ions from the single-phase region and lead to significant changes in the diffusion behavior. As shown in Figure 2(b), 2(e), 2(h), a common feature can be observed in the $D(x)$ curves of Li_xCoO_2, Li_xC_6 and $Li_xMn_2O_4$ that abrupt drops occur in the order-disorder two-phase regions followed with the increases in the subsequent single-phase areas. These trends of $D(x)$ can be ascribed to the two-phase-boundary-dominated mechanism. Although it is impracticable to evaluate the kinetic difference between the ordered and disordered single-phase states with the same concentrations by experiments, the calculated

results of $D(x)$ for Li_xCoO_2 show that[226] the value of ordered phase at x=0.5 is smaller than that in the neighboring disordered phase due to the increased activation barrier (see Figure 11). It is expected that the in-plane ordered ion occupation instead of the disordered configuration with the identical concentration can be regarded as another reason to affect the mobility of ions due to the increased stability of ions by the symmetry arrangement. It can lead to the decrease of energy at the equilibrium site in the migration energy curve and then increase the migration barrier in this case. Furthermore, it is intriguing that the phase transformation of Li_xCoO_2 in the region of $0.75<x<0.95$, as observed in the voltage curve (see Figure 2(b)), can not be reproduced by DFT calculations, indicating the existence of non-structural transformation in this region as discussed below.

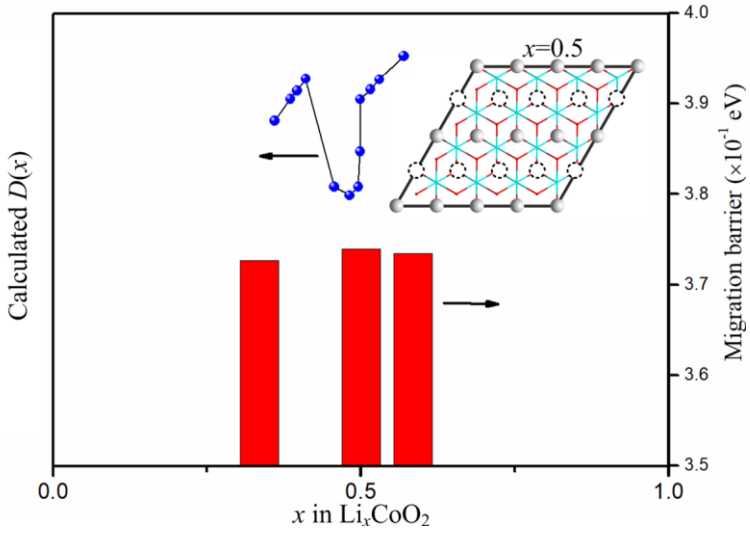

Figure 11. Calculated trend of $D(x)$ near the region of x=0.5 in Li_xCoO_2 and the corresponding trend of the migration barrier, data obtained from Ref.[226]. The inset corresponds to the in-plane ordered distribution of Li while x=0.5, data obtained from Ref.[225].

3.3. Electronic-structure transformation effects

A two-phase coexistence plateau can be observed in the Li_xCoO_2 voltage curve at about 3.9 V ($0.75<x<0.95$) as shown in Figure 2(b), corresponding to two hexagonal

cells with the same crystal symmetry but only a small difference of about 0.1 Å in the *c*-lattice parameters (see Figure 12).[63] This type of non-structural transformation has been proved that comes from the with the increasing *x* as indicated by the decreasing trend of electronic conduc metal to insulator transition tivity with *x* shown in Figure 12.[227-230] It has also been suggested that this phenomenon can be observed in $WO_3.2H_2O$.[231-232] The transformation mechanisms, usually induced by the electronic correlation in electronic structures (Mott) and/or the degree of disorder in the crystal structure (Anderson), involve a large special topic referred by Mott and/or Anderson transitions.[233-236] A Mott-type model was proposed for the first-order transition of $LiCoO_2$ from a Mott insulator ($x>0.95$) to metal at Li-vacancy rich state ($x<0.75$) due to that the mixture of isolated impurity band and t_{2g} bands of Co can form the partially filled valence bands during the deintercalation of Li^+ from $LiCoO_2$.[237] However, the disordered distribution of Li vacancies cannot completely exclude the effect of Anderson transition.[229] This electronic-structure transformation causes an unexpected increase of diffusion coefficient in the high-concentration single-phase region ($0.95<x\leq1$) and a decrease trend in the two-phase region ($0.75<x<0.95$) as observed in many experiments (see Figure 2(b)).[55, 238-240] These trends can still be ascribed to the two-phase-boundary-dominated mechanism. The driving force at the two-phase boundary has been phenomenologically ascribed to the electronic-state transformation from the delocalization to localization[227] because the boundary strain in this case may be negligible due to the small differences in their lattice parameters, but the observed deformation of oxygen octahedrons and changed Co-Co bond lengths (see the inset in Figure 12) with different values of *x* may account for the structural effect on the transformation.[227, 229] The increasing trend of diffusion coefficient at high concentration region is contrary to the decreasing trend of electronic conductivity (see Figure 12), indicating that the ion transport in the bulk state affected by the phase transformation is not always in positive correlation with the electronic conductivity as exhibited in $LiFePO_4$ (see Section 5).

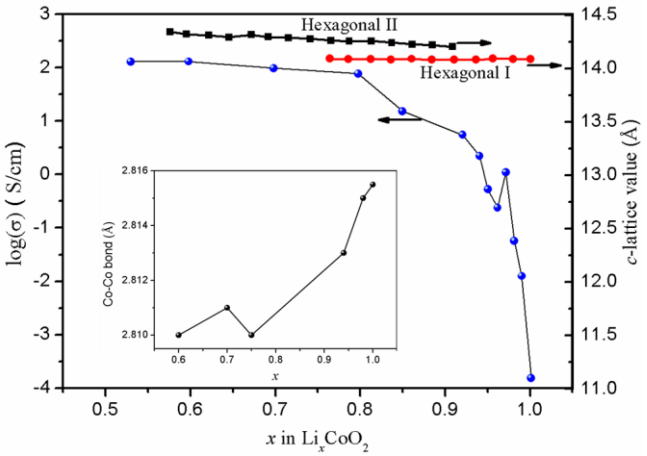

Figure 12. Measured electronic conductivity of Li_xCoO_2 as a function of x, data obtained from Ref.[229], and the corresponding c-lattice values, data obtained from Ref.[63]. The inset corresponds to the measured Co-Co bond length varied with x, data obtained from Ref.[227].

4. Geometry dependence

4.1 Size effects

It is generally believed that the intrinsic diffusion kinetics of ions in bulk state limits the rate capability, but extensive experimental results[14, 83, 241-243] have confirmed that the electrode composed of nanosized particles can significantly affect the reaction process at the electrolyte/electrode interface and that a higher rate of intercalation/deintercalation processes can be achieved owing to the shortened diffusion distances according to the relationship between the characteristic diffusion time t and the characteristic diffusion length L by $t = L^2 / D$.[13, 244] In addition, the size effects can also alleviate the defect hindrance on ion transports as exemplified by the defective $LiFePO_4$.[90] However, the improved rate performance may only be realized at the expense of cycling stability and capacity due to the unexpected surface reactions in some cases. For example, graphite particles at nanoscale can cause severe cycling and safety problems by the excessive formation of solid electrolyte interface

(SEI) layer and deposition of Li on the surface.[13, 245] This deficiency is also applied for the nanosized Si negative electrode.[246] Thus, thoroughly investigation of the reaction and diffusion kinetics during the charging/discharging processes with dependence on the grain size and boundary is required.

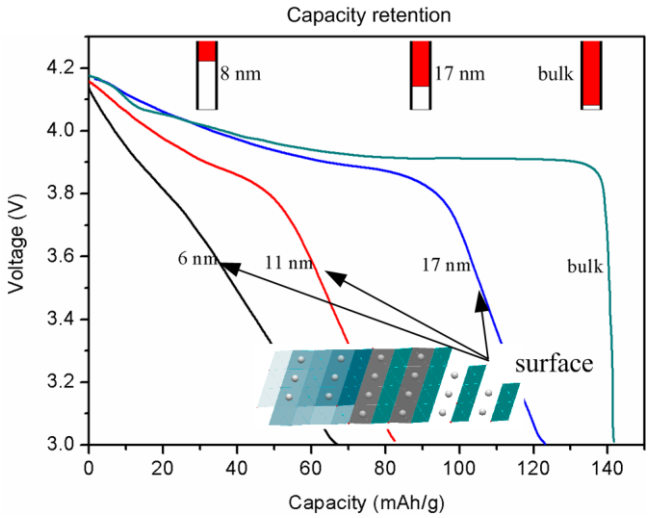

Figure 13. Galvanostatic voltage curves for Li_xCoO_2 nanoparticles with different sizes and their corresponding capacity retentions in contrast with that in bulk state, data obtained from Ref.[247].

In layered structure, such as Li_xCoO_2, it has been proposed that size-dependent intercalation process under the high rate occurs gradually from the outer to the inner layers due to the non-stoichiometry on the surface and only a few host layers involved in the configuration readjustment.[247] Smaller nanoparticles can enhance the kinetic properties of outer layers, leading to the diminishment of the two-phase coexistence region by substitution of a solid-solution process as indicated in the size-dependent voltage curves (see Figure 13). This surface-induced phenomenon has also been observed in the bulk graphite particles during the charging/discharging processes under high rates, corresponding to some intermediate Li-rich phases formed from the preferential occupation of the outer layers.[218] The edge preference for Li occupation in graphite has also been confirmed from the bright-field high-resolution transmission electron microscopy (BFTEM).[248] Within the scale of 10^0 nm, the electrode particles have chances to transform the diffusion kinetics from the two-phase boundary to the

solid-solution-state process completely. Correspondingly, the reaction process at the interface could become the rate-limiting step due to the increase of the surface-volume ratio and the improvement of the diffusion kinetics in the interior region. The enhanced interfacial reaction can also introduce significant influences on the cyclability of electrode as evidenced by the larger drop of capacity retention of Li_xCoO_2 nanoparticles compared with the bulk material (see Figure 13).[247] Combined with the other results, such as the high reaction activity of nanosized graphite to form the surface SEI layer,[13, 245] and the enhanced dissolution of manganese from the nanosized $Li_xMn_2O_4$ surfaces,[249-251] it can be deduced that the competition between the surface and cohesive energies of the host[252-253] in the very small particles can interrupt the symmetry movement (or the long-range collective behavior) of the host atoms in the bulk state, resulting in the disordered diffusion of Li and the disappearance of two-phase coexistence region while the nucleation condition is not satisfied. In this case, the mole surface energy can be increased to be larger than the heat of demixing transformation from the disordered solid-solution state to the two-phase mixture as estimated by $LiFePO_4$.[254-255] The driving force for the ion diffusion would be switched from two-phase boundary stress to the mixture of surface tension and coherency stresses (defined as the continuous strains across the interface[256]) in the multiphase particles.[254, 256-258] This feature pronounces that the lower limit of the particle size should exist to guarantee the bulk stability and kinetic transformation (about 10^0~10^1 nm). For example, a particle of $LiCoO_2$ with the size of about 6 nm has shown the complete violation from the solid-state diffusion defined in the bulk state (see Figure 13).[247] For the $LiFePO_4$ particle, a size of about 15 nm was predicted to be the critical size to completely transform the particle to the solid-solution-state Li_xFePO_4 from the two-phase region[254] and a particle size of 40 nm has been confirmed that can satisfy this condition.[259] Nanoparticles of $LiMn_2O_4$ smaller than 15 nm have been proved that can realize the full lithiation without obvious two-phase-boundary movement at the high discharge rates.[260]

In this small size region (about 10^0~10^1 nm), ion diffusion in the solid state of a

intercalation electrode has chance to be transformed to the capacitive behavior as identified by the signature of the slope line in the galvanostatic voltage curve (V(x)) or the distorted rectangular shape in the cyclic voltammogram (CV).[12, 41, 261-262] The appearance of intercalation capacitance blurs the boundary between the bulk diffusion and the surface capacitive behaviors, especially in some layered 2D materials, such as the MXenes with bulk-involved intercalation capacitances,[205, 263] or the porous materials, such as the small-pore carbon,[264-265] and the α-MnO_2, which exhibit the significant contribution of ionic intercalation in aqueous electrolytes.[125]

A very simple method to differentiate the diffusion and capacitive process is based on a power law between the peak current i and scan rate ν (ν=$\Delta V / \Delta t$) in the CV curves according to the relationship of $i \propto \nu^b$, where b=1/2 corresponding to the diffusion process and b=1 corresponding to the capacitive process.[266] It is feasible to separate the diffusion and capacitive current by defining the contribution of CV current from the two parts according to the fitted parameters of k_d and k_c in the relationship of $i = k_d \nu^{1/2} + k_c \nu$.[41, 267-268] The kinetic difference can be understood as that the ideal capacitive current is mainly driven by the surface force that comes from the change of local electrostatic potential ΔV_e at the electrical double layer (EDL) interface. Since the measured ΔV mainly comes from the contribution of ΔV_e with $\Delta V \approx \Delta V_e$ in this case, so the capacitance C should be independent of ν as indicated by $(i = C\nu) \propto \nu$. In contrast, the driving force for the diffusion current comes from the gradient of guest-element chemical potential $-\nabla\mu$, which includes the contributions of interactions among the host atoms, transferred electrons, and guest ions.[269] The nonlinear relationship between i and ν is inevitable. Note that this method cannot be employed to differentiate the contributions come from the intercalation pseudocapacitance, surface pseudocapacitance, and EDLC because all of them have been assumed to follow the consistent capacitive behavior in this model.[262]

In the medium size region (about 10^1~10^2 nm), the miscibility gap in the multiple-phase particles should be a monotonic function of the particle size as evidenced by the contracted miscibility gap between $LiFePO_4$ and $FePO_4$ with the decreasing particle size (see Figure 14).[254] The size-dependent two-phase region can also be found in the prominent voltage plateau of $LiFePO_4$ that gradually shortens the range by decreasing the size of particles, exhibiting a widened *x* range of non-stoichiometry as shown in Figure 14. These features ensure the possibility to get a tradeoff between the rate capability and capacity based on the different kinetics processes between the solid-solution and the two-phase coexistence states in terms of particle size. For example, a size of 17 nm has been suggested to be sufficient to reach a compromise between the rate enhancement and capacity loss for the Li_xCoO_2 sample.[247] Therefore, this scale (about 10^1~10^2 nm) can be regarded as the intermediate range for the kinetic transformation from the bulk-symmetry control to the solid-solution control.

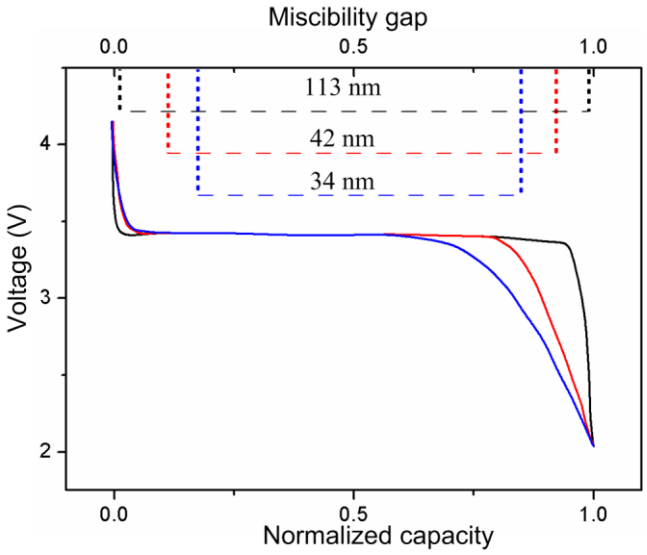

Figure 14. Galvanostatic voltage vs. normalized capacity curves for $LiFePO_4$ nanoparticles with different sizes and their corresponding miscibility gaps, data obtained from Ref.[254].

In the large size region (about 10^2~10^3 nm), the predictable size-dependent laws

should dominate the size effects on the diffusion process without changing the bulk kinetics. Specifically, the size effect on diffusion relies on the relationship of $t = L^2 / D_{\text{bulk}}$, where D_{bulk} represents the bulk diffusion coefficient. The improved rate performance in this scale mainly benefits from the shortened diffusion distance and larger specific surface area compared with that in the bulk state. As a prototype of the intrinsic insulator of ions and electrons, $LiFePO_4$ can be improved to the practical level by using the nanoparticles (~10^2 nm) free[270] or coated with carbon particles,[271-272] stressing this size effect. Some other systems validated by this size effect include $Li_4Ti_5O_{12}$[273-274] and alloys.[13, 275-276] To sum up, Figure 15 shows the effects of different size scales on the kinetics of ion diffusion. They can be coarsely divided into three regions denoted by the large-size region that follows the bulk-state kinetics, intermediate region between the two-phase reaction and solid-solution-state kinetics, and small-size region that belongs to the solid-solution state, respectively.

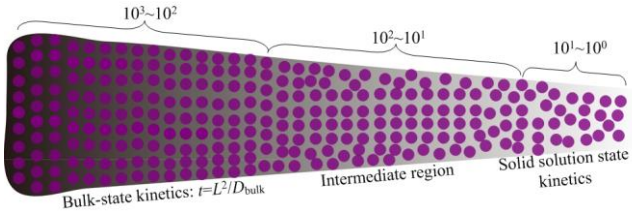

Figure 15. Schematic diagram of the size effects on the kinetics of ion transport within different scale ranges.

4.2 Interfacial and orientation effects

According to the path dependence of Li diffusion (see Section 2), it is expected that well-aligned crystalline particles under specific orientation should facilitate the diffusion process of ions, especially in the 1D- and 2D-pathway structures. For $LiCoO_2$, atomic force microscope study[277] has provided the direct microscopic evidence for the increased Li diffusion at certain grains and grain boundaries by mapping the spatial variation of ionic diffusion time on a polycrystalline film. Study on orientation effect on Li diffusion in $LiCoO_2$ has proved that the (104) oriented

facet is easier to diffuse Li than the (003) oriented samples with an increased diffusion coefficient by over one order of magnitude.[278] The staggered morphology in the (104) facet along the *c* axis can facilitate the insertion/removal of Li^+ ions into the 2D planes from the prismatic surfaces compared with the impenetrable (003) planes. It mainly benefits from the size effects based on the pyramid shape (see Figure 16(a)).[279] Analogously, the CV measurements on HOPG showed that an order of magnitude of current density induced from the edge planes larger than that from the basal planes can be observed.[280] As another example, many works have confirmed that the orientation of $LiFePO_4$ particles is one of the dominating factors to improve its electrochemical performance,[281-282] especially for the (010) oriented samples.[281, 283] These features emphasize the correlation between the transport pathway of ions and the exposed surface of the sample.

In addition to the orientation, the ion transport at the surface region also depends on the interfacial reaction kinetics during the intercalation/deintercalation processes, which is usually estimated by charge transfer resistance R_{ct}. This part of kinetic contribution can usually be observed in the EIS with a semicircle profile at the lower frequency region in the experimental Nyquist plot (see Figure 16(b)) and can be simulated by using the Randles equivalent circuits.[284-285] They are usually referred by a special topic on interfacial reaction kinetics[286-287] described by many models, such as the Butler-Volmer kinetics,[288-289] Frumkin isotherm model,[290] and so on.[289] The phenomena stressed here are the details of microscopic charge transfer process at the interface as shown in Figure 16(b). The value of ΔE_{ct}, defined as the activation energy of interfacial reaction, can be employed to illustrate the hindrance role on the charge transfer process according to the relationship of $1/R_{ct} \propto e^{-\Delta E_{ct}/kT}$, which depends on the solvent species due to that the process usually involves the desolvation steps of solvated ions.[291-292] Incompletely desolvated ions can decrease the barrier if they can be inserted into the pores or the expanded interlayer spaces of electrode particles. The passivation layer, such as the anodic SEI film formed at the interface,

can also introduce resistance for the conduction of ions as usually observed in the EIS with a semicircle at the high frequency region (see Figure 16(b)). The charge transfer process at the grain boundary (electrode/electrolyte interface) can become a rate-limiting step while the bulk diffusion is very fast, corresponding to a much larger activation energy ΔE_{ct} than the migration barrier in the interior. Such as in graphite with the intrinsic solid-solution-state diffusion coefficient of 10^{-6} cm^2/s,[27] the value of diffusion coefficient dominated by the interfacial effect can exhibit surface-dependent feature in the curves of concentration-dependent $D(x)$ obtained from the natural and artificial graphites (see Figure 16(c)).[293-294] In this case, the two-phase-boundary-dominated trends as exhibited in the thin-film sample (see Figure 2(e)) are obscured and the diffusion time t is mainly contributed from the initial Li-ion transfer process under the low-concentration condition, which can be correlated with the surface area and the specific boundary orientation without considering the SEI layers. The observed decreasing trend in $D(x)$ with x[293-296] can be reproduced by the simulation with a model dominated by the interfacial reaction process.[297] This feature can be understood as that the initial lithiation process strongly depends on the interfacial reaction process. The decreasing trend of $D(x)$ corresponds to the transfer of the limiting step from the interfacial reaction to the interior diffusion control as evidenced by the decreasing trend of charge transfer resistance with the increasing x[296, 298] (see Figure 16(c)) and the results of kinetic study on graphite from the initial dilute stage 1 to stage 4 as mentioned before.[217] Note that the decreasing trend of charge transfer resistance can also match the increasing trend of electronic conductivity (σ_e) in Li_xC_6 with x.[299-300] The inverse match, corresponding to the increasing trend of R_{ct}[175] and the decreasing trend of σ_e with x,[227] can also be observed in Li_xCoO_2, indicating the important role of electronic transport in the interfacial reaction kinetics (see Section 5).

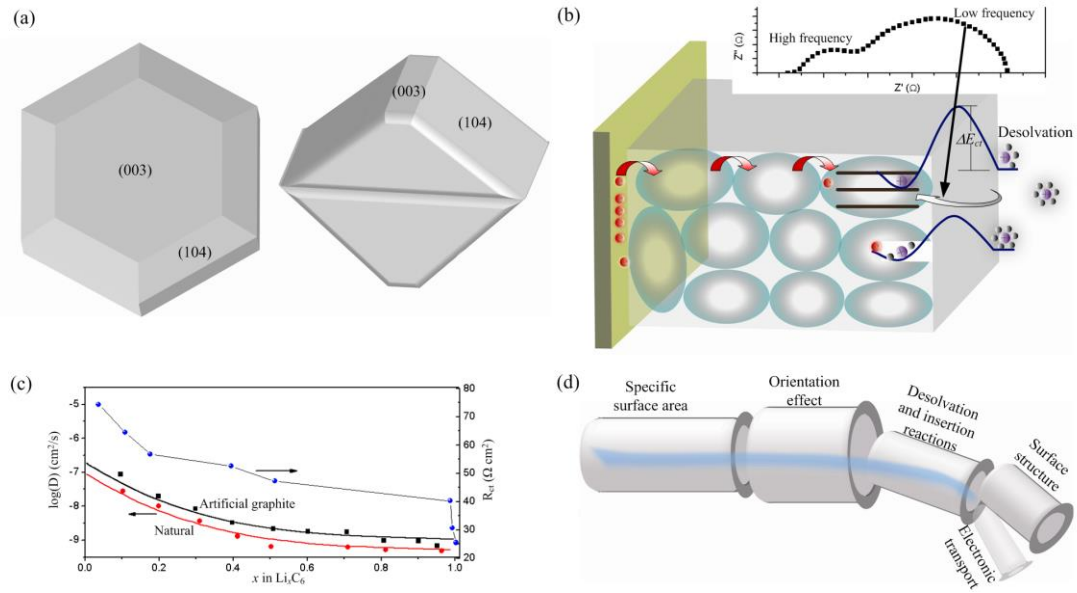

Figure 16. (a) Morphologies of different oriented particles of $LiCoO_2$, data obtained from Ref.[279]. (b) Schematic of interfacial reaction involving the desolvation process that can be estimated from EIS. (c) Measured (dots)[293] and simulated (solid lines)[297] $D(x)$ of natural and artificial graphite and their corresponding R_{ct},[298] data obtained from Refs.[293, 297-298]. (d) Schematic of effect factors on the interfacial reactions with different competitive kinetics in analogy with the different gravitational potentials.

The interfacial reaction kinetics also depends on the surface structure and grain boundaries of the electrode particles.[301] Comparative study on the nanocrystalline and amorphous Li_xTiS_2 has suggested that the surface-confined pathways with lower activation barriers may act as the dominant tracks for the interfacial diffusion.[302] The other example is the surface-modified $LiFePO_4$,[1] which has been reported to be improved to a rate capability of about 20s full discharge by using an off-stoichiometry nanosized sample with amorphous surface, demonstrating the role of surface phase for ion conduction. The measured rate capabilities (10-20s) clearly demonstrate the enhancement of electrochemical performance of the $LiFePO_4$ particles through modifying their interfacial reaction kinetics by constructing a fast ion-conducting surface. Although the results are controversial due to the large-ratio coating of carbon black and binder (over 70 wt%), the improved performance induced by surface modification provides a guidance to improve the kinetics. The interfacial reaction

kinetics of $LiFePO_4$ is different from the layered compounds. The insertion models of $LiFePO_4$ mentioned above (see Section 3) have provided us a picture that the interfacial reaction, nucleation and two-phase boundary movement should mix together at the same time to control the ion transport in this special structure, not like in the layered systems that follow the sequential processes. However, the determination of rate-limiting step on this structure still invoked controversy[87, 303-304] due to its poor electronic conductivity that can vary within the range of 10^{-7}~10^{-11} S/cm as measured in the bulk states.[305-307] The kinetic source for the ionic insertion process usually needs the presence of transferred electrons, hence many researchers believed that the electronic transport plays the dominant role in the rate-limiting step because the additive of conductive carbon or doping of specific ions (such as Nb, Zr, Mg, Ti) can improve the rate performance of this system significantly by forming the percolating conducting networks, which can increase the electronic conductivity by over 7 orders of magnitude correspondingly.[306, 308] On the other hand, the reported values on a single-crystal sample by using the electronic blocking cell gives a smaller ionic conductivity range ($<10^{-9}$ S/cm) than electronic conductivity, suggesting the dominant role of ion transport.[305] As a comprehensive evaluation, many studies reported that the transports of ions and electrons should be coupled together[213, 309] and the real kinetic processes should be different from the separately measuring processes for electrons and ions, as supported by a better rate performance obtained from a mixed electronic/ionic conductive doped $LiFePO_4$ compared with the electronic or ionic conductive samples.[310] The study indicates that the competitive and cooperative behaviors between the transferred electrons and guest ions exist on the surface or the two-phase interface in the insulating particles as discussed in the following Section.

To sum up, the interface-controlled condition relies on the kinetic process at the interface in addition to the specific surface area. Particle orientation, surface structure, and electronic transport can render a significant influence on this process as illustrated in the schematic diagram (see Figure 16(d)) about the possible limiting factors on the interfacial ionic transport process with different kinetics in analogy to the

gravitational potentials.

5. Cooperative dependence

5.1. Transferred electron effects

In a lithium-ion battery under the ideal open-circuit state, the two electrodes are difficult to transfer Li^+ ions without considering the self-discharge mechanism.[311] Once an electron can be spontaneously transferred from a higher Fermi-level electrode (anode) to the lower one (cathode) through a conductor, the instantaneous local electric fields near the two electrodes will be enhanced and the field strength can be increased along with the accumulated number of electrons. While the field strength is enhanced enough to push the Li^+ ions into or out from the electrodes over the equilibrium state, the deviation from the neutral states of the electrodes will be relieved and the transfer of a pair of charges is completed. It can be deduced that the movement of Li^+ ions in the host structure should depend on the instantaneous local potential formed from the interactions among the host atoms and the transferred species (electrons and guest ions), site distribution, temperature, and so on. The kinetic effects come from these factors are usually described by using the gradient of guest-atom chemical potential $-\nabla\mu$ under the neutral condition.[53] In some cases, the transferred electrons may play the dominate role on the instantaneous local potential field as will be stressed here, especially for the high-rate condition or the poor electronic conductive system.

Four competitive rate-limiting ionic transport processes can be identified from Figure 17(a) according to the different kinetic properties of the transferred electrons. At process 1, the transferred electrons act as the role of inducing local applied voltage

on the activation barrier in the initial ions insertion/removal processes. The equilibrium barrier can be lowered by the electrostatic interaction. If the electrons at the interface between the current collector and electrode or in the electrode are accumulated too fast, the enhanced desolvation process will happen, leading to a faster interfacial adsorption of ions and the blocking of active sites at the surface of the electrode due to the slow unmatched bulk diffusion process,[312] which can enhance the polarization.[313] In this case, a common phenomenon can be observed in most of intercalation electrodes that the capacity always decreases with the C-rate as shown in Figure 17(b).[314-316] Process 2 corresponds to the general ionic diffusion process in the solid-solution state under the charge neutrality environment. It seems that part of the transferred electrons act as the role of delocalized electrons to contribute to the driving force of $-\nabla\mu$ for the movement of ion under the disordered state as studied in graphite,[299, 317] because the V(x) curve always exhibits a slope line feature just like the capacitive behavior as exhibited in the hard carbon (see Figure 17(c)).[318] The similar trends can be found in Li_xCoO_2 ($0.5<x<0.75$) under the mental state, and Li_xTiS_2 ($0.1<x<0.8$) with high electronic conductivity (10^3 S/cm)[319] as shown in Figure 2. The delocalized electrons also take part in the redox reactions of transition metal ions. These electrons may be concentrated at the electrode/electrolyte interface, but they are different from the free electrons in metal. They can be denoted by the quasi-delocalized electrons,[319] because the kinetics induced by these transferred electrons is superior to the localized electrons participating in the two-phase transformation process as denoted by process 3 in Figure 17(a) and inferior to the electrons populated in the EDL capacitor that are driven by the pure electrostatic force between the guest charges. Process 2 is usually regarded as the analogy to the pseudocapacitive behavior as identified by the voltage slope curve due to their similar kinetics contributed from the transferred electrons and the disordered ion distribution.[261, 269, 320] Process 3 corresponds to the two-phase process including the kinetic combination of the localized transferred electrons and ions along the two-phase boundaries as exhibited in the $LiFePO_4$ with a large plateau exhibited in

the V(x) curve (see Figure 2(d)). The polaron model has been introduced to emphasize the effect of the transferred electron on the ionic transport process.[309] The small polaron, defined as the excess localized electron (or hole) accompanied by the self-induced local lattice distortions,[321-322] can be localized near the redox couple of Fe^{2+}/Fe^{3+} in the $FePO_4/LiFePO_4$ two-phase boundary region.[323] The movement of transferred electron (or hole) polarons can be realized by the hopping process between the transition metal sites accompanied with the transfer of local distortion, which can be facilitated by the cooperative coupled movement of the guest Li^+ ion.[213] Many researchers believed that the coupled movement of the exciton-like Li^+-electron pairs along the two-phase boundary should be the dominant charge transport process,[95-96, 213, 309] exemplifying the cooperative role of localized electrons on the ionic transport process. However, in addition to the proposed driving force mentioned in Section 3, the dominant kinetic mechanism to drive this cooperative behavior and kinetic transformation still need to be further explored because many factors can affect its rate capability significantly, such as doping, coating, particle size, porosity, and surface-phase modification as mentioned before. As another representative, process 4 corresponds to the transport process of ions under the assistance of solvent molecules, such as the water molecules in aqueous electrolytes. In this case, the role of transferred electrons may be more close to the free electrons in the EDL capacitor in contrast with that in process 2 because the presence of water can act as the role of dielectric layer as will be discussed in the following Section, which can intervene the bonding between the guest ions and the host by shielding the electrostatic interactions among the ions (such as H^+, Na^+, Mg^{2+}, Zn^{2+}) and the host blocks as exemplified by the large channel system (such as MnO_2,[324-325] V_2O_5,[326] MXenes[203, 206, 327-329]), leading to the quasi-delocalized distribution of the transferred electrons as identified by the slope line in Figure 17(d). As far as the rate capability is concerned, it can be found that the kinetics for the ion transport in process 4 should be superior to process 2 but inferior to the geometrical metal capacitor. It has chance to behave like the EDL capacitor in process 4 even involving the bulk transport of ions as evidenced by the MXenes family.[263] A sample of $Ti_3C_2T_x$ MXene has been reported[206] that can achieve

a capacitance of over 200 F/g in no more than 0.1 s based on the intercalation pseudocapacitance mechanism (corresponding to process 4),[205] which is comparable with the carbon supercapacitor.[330]

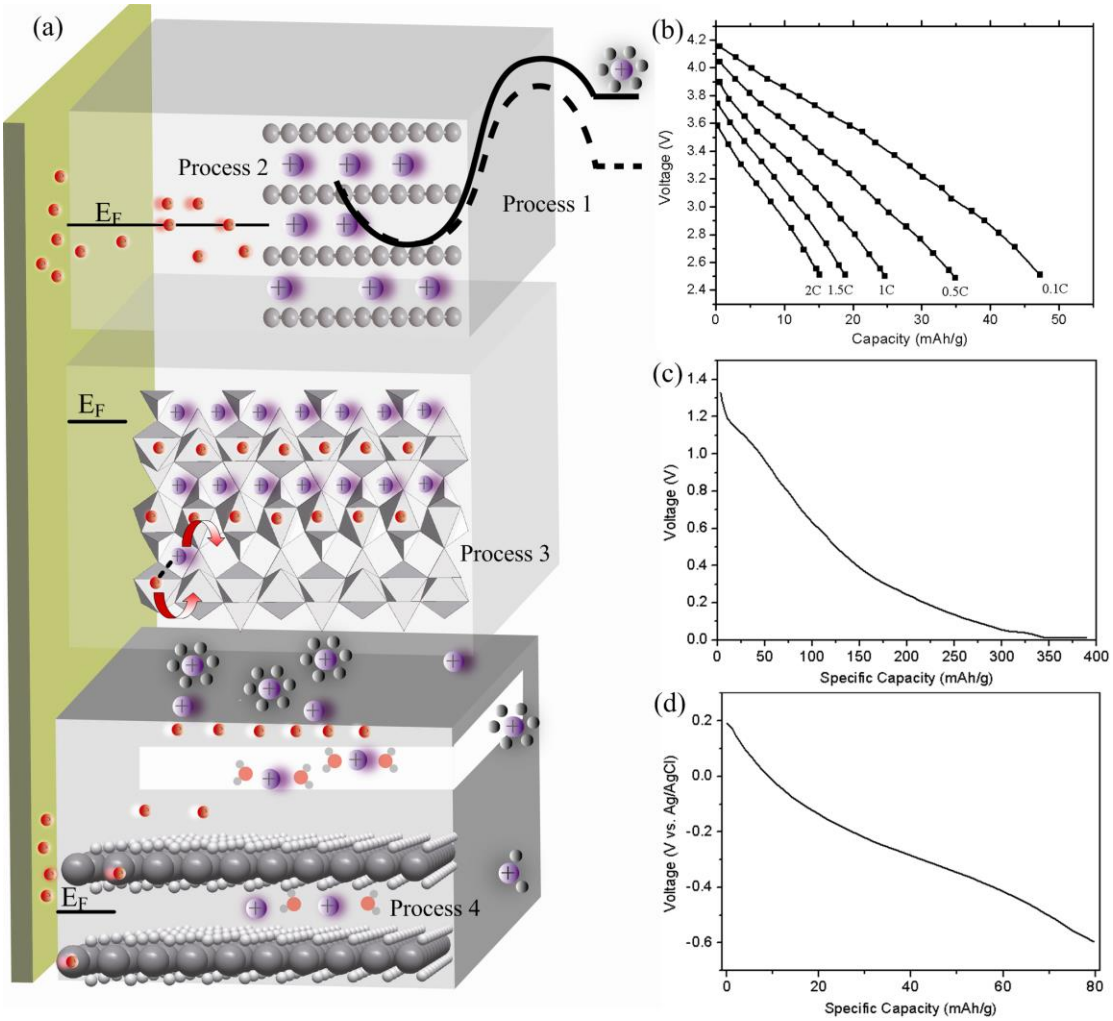

Figure 17. (a) Schematic diagram of four types of processes for the ion transport based on different kinetic properties of the transferred electrons. (b) C-rate correlated galvanostatic voltage curves for a $LiCoO_2$-Carbon full cell, data obtained from Ref.[314] (c) Trend of voltage-capacity curve for the hard carbon, data obtained from Ref.[318]. (d) Trend of voltage-capacity curve for the $Ti_3C_2T_x$ MXene, data obtained from Ref.[327].

Based on these different microscopic processes, the pseudocapacitive and battery-type behaviors may be differentiated by the different kinetics of the

transferred electrons. It can be found that the increase of electronic conductivity can introduce significant improvements on processes 2 and 4 based on the pseudocapacitive kinetics contributed from the quasi-delocalized electrons, but the improvement on process 1 and 3 should come from the enhancement of the charge transfer kinetics or the two-phase boundary kinetics induced from the fast (localized or delocalized) electron transfer, as evidenced by the consistent trends between R_{ct} and electronic resistance ($1/\sigma_e$) with x exhibited in Li_xC_6 and Li_xCoO_2 as mentioned before, which is also supported by the significant improvement of electrochemical performance in $LiFePO_4$ by carbon coating.[331] Hence, intrinsic poor electronic conductivity in the electrode material can lead to the decreased rate capability through decreased kinetics in processes 2 and 4, but not always take effect in processes 1 and 3 as evidenced by $LiFePO_4$[65, 94, 177, 332] and the insulating $Li_4Ti_5O_{12}$.[333-334] Compared with the ionic transport process, the transferred electrons in processes 2 and 4 can act as a part of kinetic source to affect the ionic diffusion under the parallel process, but the transferred electrons in process 1 and 3 have chances to become a competitive role to determine the limiting step under the sequential process as exemplified by $LiFePO_4$ mentioned before.

5.2 Water molecule effects

Early studies on Li intercalation compounds in non-aqueous electrolyte believed that the presence of water in Li-ion batteries is harmful to the cycling performance because it can react with electrolyte,[335] such as with $LiPF_6$ to produce the acidic species,[336-337] and react with anode electrodes,[338-339] such as the reaction process on the Li/H_2O interface to form the LiOH and Li_2O,[336] and reformations of SEI at the carbon[340] and Li anodes,[341] which can consume the electrolyte and electrode surface (or SEI). In addition, the electrolysis of water at high voltage is also another problem. Therefore, the water needs to be removed before the electrochemical tests. However, the structural water in the electrode seems that can play the multiple roles if it can be

inhibited to be liberated to contaminate the electrolyte.[338] As exhibited in the 1D-channel MnO_2,[342] the residual water has been identified into two main groups. One corresponds to the surface adsorbed molecules that can be removed below 150 ºC. The other corresponds to the chemisorbed structural water in the structure associated with two types of protons connected with Mn^{4+} vacancies and Mn^{3+} redox sites,[113, 343] which can be dissociated over 200 ºC.[344] Some studies indicated that a part of chemisorbed structural water has chance to be stabilized in the structure during the lithiation process,[338, 345] and can even take the positive effects on the Li storage capacity and cycling capability, due to its improved kinetics on ionic diffusion as exemplified by using the sol-gel MnO_2 samples.[346-347] The water molecules also play the role of pillar to affect the cycling stability of the structure. The beneficial effects of a small residue of structural water on Li^+ and Mg^{2+} ions storage have also been observed in Vanadium oxides,[348-350] WO_3[351], and birnessite δ-MnO_2.[352] However, the residual proton associated with water still has chance to experience the ion exchange process with Li^+ ions as evidenced in the dehydration processes of α-MnO_2.[353] The Li^+/H^+ exchange is a common phenomena in these hygroscopic compounds,[354-355] so it is generally believed that the gradually departure of water from the structure is inevitable and the dehydration procedure is a necessary step for the Li-ion battery applications.

On the other hand, these negative effects induced by water contamination in the non-aqueous electrolytes can be circumvented by using the aqueous electrolytes, or the multivalent guest ions with the non-aqueous electrolytes insensitive to react with water.[20] In the non-aqueous electrolytes, many studies on the layered materials with large interlayer distances have shown that the presence of water in the interlayer space or in the electrolyte can significantly improve the capacity and kinetics of ionic diffusion for the multivalent ion storage as shown in Figure 18. Figure 18(a) lists the comparative test capacities and cycling capacity retentions for several potential electrode materials for Mg^{2+} storage with and without water in the non-aqueous electrolytes (or in the structures). In the case of V_2O_5,[356] it can be found that the

water-containing organic electrolyte is determinant to realize the reversibility of Mg^{2+} storage. A phenomenon can be observed that the storage capacity can increase with the exchanged content of water in the structure and electrolyte during the initial cycles and decrease after the capacity reaching a maximum value as exemplified in δ-MnO_2[357] and MoO_3.[358] The reason can be correlated with the modification of the interlayer pillar species and the reformation of the solvation-shell configuration of ions in the electrolyte with the participation of water during the initial cycling processes. The associated water can significantly improve the charge transfer kinetics at the interface due to the change of desolvation energy or the co-intercalation of the solvation shell (see processes 1 and 2 in Figure 18(b)), and also can modify the diffusion kinetics in the interlayer space due to the shielding effect of the water-solvation shell[326] that can weaken the interactions between the multivalent ions and host layers as illustrated in the δ-MnO_2[352, 357, 359] and V_2O_5.[349, 360] Studies of R_{ct} on $LiMn_2O_4$ in aqueous and non-aqueous electrolytes also have shown that the interfacial reactions involving the desolvation of ions can give a smaller activation barrier in aqueous electrolytes,[361] confirming the possibility that the interfacial reaction kinetics can be improved by solvating a water shell around the multivalent ions in non-aqueous electrolytes (see process 1 in Figure 18(b)). According to their different stabilities, it can be found that the residual water molecules in the host structure and electrolyte can be classified into two types. One corresponds to the stable structural water remained in the structure during the synthesis and electrochemical processes, like in the cases of $V_2O_5.nH_2O$.[349] It plays the role of pillar to stabilize the structure and accommodate the volume expansion/contraction. The other corresponds to the hydrated ions that can be co-intercalated/deintercalated during the electrochemical or synthesis processes, such as exhibited in $Ti_3C_2T_x$ MXene,[203, 362] α- and δ-MnO_2[125, 210] in aqueous electrolytes. These intercalated water molecules can be stabilized by the ions and can facilitate the movement of ions in the interlayer space.[203] The structural water is expected to be more stable and less mobile than the intercalated solvent water. As evidenced by HF-acid etched $Ti_3C_2T_x$ MXene, the residual water can be spontaneously de-intercalated from the interlayer space due to the absence of ions,[363]

but a part of structural water in V_2O_5 can remain stable during the Mg-ion insertion/extraction processes.[349] Under the condition of water deficiency, these multivalent-ion storages always exhibit the poor cycling performance due to the coexistence of conversion reactions and topotactic insertion/extraction processes as suggested in the studies of $Ti_3C_2T_x$ MXene[364], δ-MnO_2,[357] and α-MnO_2.[365] For the part of Mg-ion storage, the sluggish reaction process can be partially ascribed to the competing driving forces for the formation of Mg-compounds (such as MgO).[36] It can be expected that the water-solvation shell can play the positive role to hinder the conversion reaction, but the stable structural water associated with the hydroxyl groups may not behave like the solvent water. Furthermore, it was reported that the stability of a part of structural water can be maintained while the guest ion is replaced by Na^+ in δ-MnO_2,[325] but this case cannot be applied to the Li^+ ion due to the undesirable reactions between the water and the electrodes or electrolytes as mentioned above. These results indicate that the positive effects of water on the charge storage process in non-aqueous electrolytes strongly depend on the type of guest ions, and water concentration in addition to the host structure, which needs to be further explored.

In aqueous electrolytes, the intercalation electrodes can encounter protons and water involved co-intercalation/deintercalation reactions differing from that in non-aqueous electrolytes.[366-367] In many cases, the pseudocapacitance behaviors may dominate the kinetic processes of charge and mass transports[9, 41, 49, 368-370] accompanied by the disappearance of the plateau of V(x) as exemplified in $Ti_3C_2T_x$ MXene[205] and MnO_2.[126] The existence of insertion/extraction processes at the interface also make it different from the EDLC kinetics.[371-372] Figure 18(c) lists the reported rate and cycling performances of several intercalation structures based on different types of guest ions that have been improved by water. From these results, it can be found that the effects of water on ionic diffusion in these cases can be divided into two scenarios.

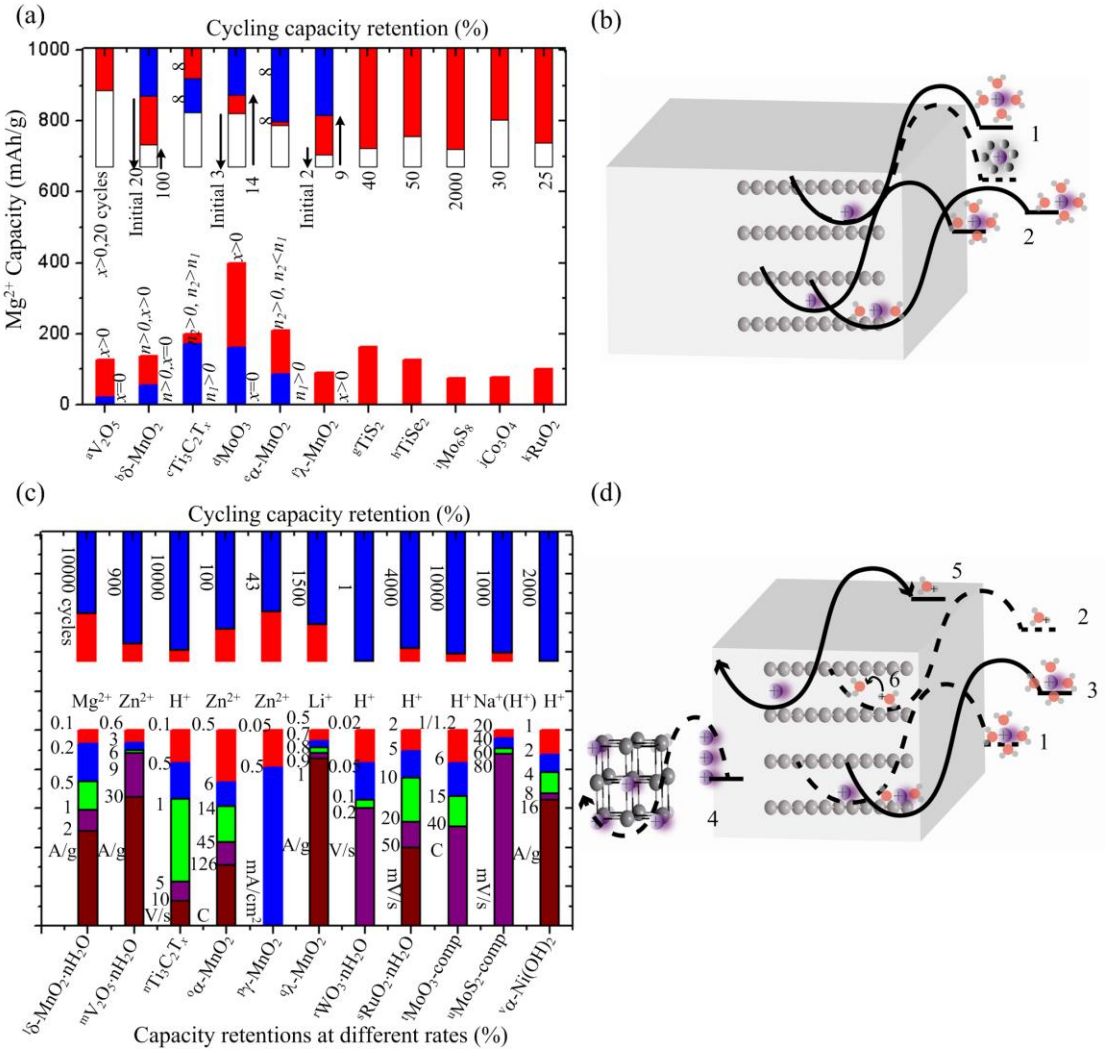

Figure 18. (a) Measured initial capacities and capacity retentions after the specific cycles as listed on the columns for some potential electrode materials for Mg^{2+} storage in non-aqueous electrolytes, where *x* and *n* denote the water content in the electrolytes and the host structures of different samples, respectively. Data were obtained from a[356], b[357], c[364], d[358], e[373], f[374], g[375], h[376], i[377], j[378], h[379]. (b) Schematic diagram of desolvation processes with different solvation shells and activation barriers. (c) Measured capacity retentions at different rates and capacity retentions after the specific cycles as listed beside the columns for some intercalation electrodes in aqueous electrolytes, where the ions denote the guest ions that may take part in the redox reactions in the host structures and comp denote the composite structure. Data were obtained from l[359], m[380], n[206], o[381], p[382], q[383], r[232], s[384-385], t[386], u[387], v[388]. (d) Schematic diagram of different types of desolvation processes in aqueous electrolytes.

One corresponds to the interfacial reaction process (see Figure 18(d)). Differing from the intercalation-pseudocapacitance behavior in organic electrolytes as exhibited in *T*-Nb_2O_5,[389] the intercalated species in aqueous electrolytes always involve multiple guest ions to take part in the redox reaction due to the presence of protons in addition to the cations in the electrolytes. The multiple processes include the competitions among the intercalation reaction of cations from electrolyte (process 1 in Figure 18(d)), the co-intercalation of hydrated ions (hydronium and hydrated cations, corresponding to the processes 2 and 3, respectively), the conversion reaction (process 4), and the ion-exchange process (process 5). Co-intercalation of solvation shells and ions has been observed in many systems as mentioned before.[125, 203, 210] It can effectively lower the activation energy of interfacial reaction by circumventing the process of complete desolvation as exemplified by δ-MnO_2 in Mg^{2+} ion storage.[359] Competitive processes between protons and cations always complicate the dominant contribution of the guest-ion species for the redox reactions such as observed in MnO_2 systems.[126-127, 210, 390] For example, investigation on ε-type MnO_2 in several aqueous solutions based on the mass-to-charge ratio measurements proposed that H_3O^+ should be the dominant species to contribute the charge storage reaction.[127] The ion-exchange model between H^+ and K^+ in KCl solution has also been suggested that the electrochemically active species may be H^+ instead of K^+ in δ-MnO_2.[210] Another typical example is γ-MnO_2 in alkaline KOH solution.[108, 391] Protons can surpass the K^+ to become the major guest ions, but the major contribution may be changed to Li^+ while the electrolyte is replaced by LiOH,[392] indicating the competitive behavior between the protons and cations in terms of the ion size, host-channel size, and pH value.[366] Furthermore, reversible extraction/insertion of cations (such as K^+, Li^+) and H^+ in aqueous solutions based on $LiMn_2O_4$ electrodes proposed that the intercalation potential of H^+ may be higher than the cations in this system.[390] Although the evidences are not sufficient,[390] they still provide a guidance to identify the type of guest ions based on the intercalation potentials. Note that the experimental evidences to prove the intercalation of cations usually depend on the surface-sensitive X-ray

photoelectron spectroscopy (XPS) data. The possible surface conversion reactions as observed in δ-MnO_2[357] and α-MnO_2[365] may obscure the presence and occupation sites of cations, which can further complicate the process to identify the dominant guest ions.[36]

The other scenario corresponds to the diffusion process of ions and hydrate ions in the interlayer space. As exemplified by $Ti_3C_2T_x$ MXene,[203] the solvent water is more mobile than the guest ions as confirmed from the MD simulations. It can stabilize the ions[200] and drive the ions to move more easily in the 3D spaces that have been expanded by the pillars of hydrated ions. Compared with the Li diffusion process in the empty space, the water molecules play the role of dielectric media to suppress the bonding of the guest ions and localization of the transferred electrons, leading to the gradual transformation of driving forces from the gradient of local chemical potential of guest atoms to the electrostatic force between the transferred electrons and guest ions, which can transform the solid-state diffusion process to the pseudocapacitive behavior.[206] In addition to $Ti_3C_2T_x$ MXene, comparative study on WO_3 and $WO_3 \cdot 2H_2O$ in acid electrolytes has also shown the transformation phenomenon from the battery-like behavior to the capacitive behavior under high scan rates due to the presence of structural water.[20, 232] In consideration of the guest H^+ in this case, the structural water at the stable sites may assist the movement of ions through the water molecule networks by employing the Grotthuss mechanism (process 6 in Figure 18(d)),[393-394] emphasizing the role of water content in the interlayer space. As observed in dichalcogenides (such as layered TiS_2),[395] the stable layer numbers of water shell in the interlayer space depend on the type of guest cations. Two layers of water have been observed for Li^+, Na^+, Ca^{2+}, but only one layer for K^+. The similar results have also been found in $Ti_3C_2T_x$ MXene with only one layer of water shell for K^+, but two layers for Li^+, Na^+, Ca^{2+}, and Mg^{2+}.[396] The trend of hydrate enthalpy ΔH_{hyd} of ions has been suggested[396] to correlate the stability and layer number of the solvation shell because they follow the consistent trend of

$|\Delta H_{hyd}^{K^+}| < |\Delta H_{hyd}^{Na^+}| < |\Delta H_{hyd}^{Li^+}| < |\Delta H_{hyd}^{Ca^{2+}}| < |\Delta H_{hyd}^{Mg^{2+}}|$,[397] which indicates the hydrate enthalpy of different types of ions can significant affect their diffusion and interfacial reaction kinetics in the layered structure as exemplified by Mg^{2+} ion storage. The water-solvation shell on Mg^{2+} is stable during the electrochemical cycling process in contrast with other cations as evidenced by the experimental results of δ-MnO_2 and V_2O_5 as mentioned above,[20, 349, 357]. Comparative studies among Mg^{2+}-, Li^+-, and Na^+-intercalated δ-MnO_2 for Li^+ storage also supported this conclusion.[209] Furthermore, the comparative studies of capacity on $Ti_3C_2T_x$ MXene in different electrolytes (LiOH, NaOH, KOH) indicated that the capacity follows the order of KOH>NaOH~LiOH.[8] The similar trend has also been found in δ-MnO_2 with KCl~NaCl>LiCl.[210] These results have shown that the correlation of hydrate enthalpy with the content of interlayer water, desolvation process at the interface and the blocking role of water molecules on the redox sites, but their effects on ionic transport kinetics at the interface and interlayer space need to be further explored in the future.[20, 370]

6. Summary and outlook

We have summarized and classified the ionic transport phenomena based on several well-studied intercalation systems, including the single-phase diffusion, phase transition, size dependence, and water assisted diffusion. Differing from the electron transport, the ion transport in intercalation electrodes always depends on the specific system and participation of electrons. Many geometry factors, such as the particle size, grain boundary, and morphology, can render significant influences on the properties of ion transport, hence complicating the generalization of these phenomena. However, different kinetic properties can still be classified according to their different influences on ion transport. For example, the solid-solution-state diffusion of ions is significantly different from the collective ion transport based on the long-range symmetric cooperative behavior. The driving forces contributed from the transferred

electrons are different between the capacitive and battery-type behaviors. Since the ionic transport process always depend on the ionic concentration in the electrode and the scan rate, many steps combined with the experimental and theoretical tools are needed to clarify the transport details and rate limiting factors in a specific electrode sample. Based on the results obtained from the well-studied electrode materials, some routes can be established, such as predicting the dominant mechanism of concentration-dependent ion diffusion from the $D(x)$ and V(x) curves and DFT calculations; confirming the microscopic migration pathways and movement details through computational simulations; combining the V(x), $D(x)$, R_{ct}(x), and $\sigma(x)$ to estimate the phase-dependent transport process and charge transfer controlled process. It is expected that these generalized results can help us accelerate the step to find out and optimize the high-power electrode materials.

Based on the fundamental principle of quantum mechanics, it can be predicted that all of the kinetic properties shown in the ionic transport processes should mainly result from the space configuration of electron clouds and their evolution with time and the new incorporated charged particles, but the accurate calculations and predictions about these kinetic evolution processes still have hindrances due to the existence of many-body effects and the large number of particles. Hence, phenomenological models usually prevail in this field, but they normally neglect many factors that may be negligible in one system but dominant in another. It usually provokes controversies such as exhibited in the structural evolution process of $LiFePO_4$. The incomplete description usually exaggerate the prominence of one-part contribution but evade the other losses, so quantitatively differentiating the kinetic transformation processes of electrode materials with the incorporation of the dominant factors is still a challenge in this field.

Based on the knowledge of ion transport, it has been realized that the kinetics of ion insertions within each constituent particle are governed by the local electrochemical

potentials of electrons and ions near the interfaces, but their quantitative correlations are not so obvious. Their kinetic processes are obviously correlated with the particle geometries and dimensions, interface phases, configurations of interconnected particles, phase transformations, and so on, which can be reflected by the experimental observations, such as polarizations or capacity changes. Therefore, current studies on these well-studied electrode materials mainly focus on the design and construction of electrode architectures, aiming at reaching the goal of completely reversible access of their entire interior volumes for ion storage. However, the progress is slow in contrast with the development of microelectronic techniques due to their difficulty in quantitative descriptions and control of the kinetic parameters in terms of the particle microstructures as mentioned above. We can expect that the studies on the quantitative differences between the local electrochemical potentials of ions in the particles and electrolytes near the interfaces in terms of the particle microstructures may accelerate the step to find out the optimized electrode architectures for a specific material, because these studies can directly correlate the experimental results with the kinetics origin quantitatively. Although little is known about these quantitative results, leaving a gap and challenge in the literature, we believe the current research can make a major breakthrough by employing the advanced experimental techniques and theoretical models.

Acknowledgements:

This work was partially supported by the National Natural Science Foundation of China (No. 52072099), Team Program of the Natural Science Foundation of Heilongjiang Province in China (No. JJ2021TD0011), and Graduate Innovation Project of Harbin Normal University (No. HSDSSCX2022-147). BW appreciates funding from the U.S. National Science Foundation (Award number: 2129982).

Data Availability Statement:

The data that support the findings of this study are available from the corresponding authors upon reasonable request.

Conflict of Interest:

The authors have no conflicts to disclose.

Corresponding Authors:

*Email: xtzhangzhang@hotmail.com

*Email: wang_cbme@ou.edu

ORCID:

Jing Wen: 0000-0002-9107-8377

Xitian Zhang: 0000-0001-6111-8844

Bin Wang: 0000-0001-8246-1422

References:

1. B. Kang, and G. Ceder, Nature **458**, 190 (2009).
2. G. Wang, M. Yu, and X. Feng, Chem. Soc. Rev. **50**, 2388-2443 (2021).
3. M. S. Stark, K. L. Kuntz, S. J. Martens, and S. C. Warren, Adv. Mater. **31**, 1808213 (2019).
4. J. Zhou, Z. Lin, H. Ren, X. Duan, I. Shakir, Y. Huang, and X. Duan, Adv. Mater. **33**, 2004557 (2021).
5. M. S. Whittingham, C. Siu, and J. Ding, Accounts. Chem. Res. **51**, 258-264 (2018).
6. X. Judez, G. G. Eshetu, C. Li, L. M. Rodriguez-Martinez, H. Zhang, and M. Armand, Joule **2**, 2208-2224 (2018).
7. Y. Li, Y. Lu, P. Adelhelm, M.-M. Titirici, and Y.-S. Hu, Chem. Soc. Rev. **48**, 4655-4687 (2019).
8. M. R. Lukatskaya, O. Mashtalir, C. E. Ren, Y. Dall'Agnese, P. Rozier, P. L. Taberna, M. Naguib, P. Simon, M. W. Barsoum, and Y. Gogotsi, Science **341**, 1502-1505 (2013).
9. D. Chao, and H. J. Fan, Chem **5**, 1359-1361 (2019).
10. Y. Liu, S. P. Jiang, and Z. Shao, Mater. Today Adv. **7**, 100072 (2020).
11. Y. Jiang, and J. Liu, Energy Environ. Mater. **2**, 30-37 (2019).
12. S. Fleischmann, J. B. Mitchell, R. Wang, C. Zhan, D.-e. Jiang, V. Presser, and V. Augustyn, Chem. Rev. **120**, 6738-6782 (2020).
13. P. G. Bruce, B. Scrosati, and J. M. Tarascon, Angew. Chem. Int. Ed. **47**, 2930-2946 (2008).

14. E. Pomerantseva, F. Bonaccorso, X. Feng, Y. Cui, and Y. Gogotsi, Science **366**, eaan8285 (2019).
15. H. Li, and H. Zhou, Chem. Commun. **48**, 1201-1217 (2012).
16. P. Guan, L. Zhou, Z. Yu, Y. Sun, Y. Liu, F. Wu, Y. Jiang, and D. Chu, J. Energy Chem. **43**, 220-235 (2020).
17. W. Chen, X. Zhan, R. Yuan, S. Pidaparthy, A. X. B. Yong, H. An, Z. Tang, K. Yin, A. Patra, H. Jeong, C. Zhang, K. Ta, Z. W. Riedel, R. M. Stephens, D. P. Shoemaker, H. Yang, A. A. Gewirth, P. V. Braun, E. Ertekin, J.-M. Zuo, and Q. Chen, Nature Mater. **22**, 92-99 (2023).
18. J. Zheng, and L. A. Archer, Chem. Rev. **122**, 14440-14470 (2022).
19. R. Usiskin, and J. Maier, Adv. Energy Mater. **11**, 2001455 (2021).
20. V. Augustyn, and Y. Gogotsi, Joule **1**, 443-452 (2017).
21. M. Jaugstetter, N. Blanc, M. Kratz, and K. Tschulik, Chem. Soc. Rev. **51**, 2491-2543 (2022).
22. E. Markevich, M. Levi, and D. Aurbach, J. Electroanal. Chem. **580**, 231-237 (2005).
23. S. D. Kang, and W. C. Chueh, J. Electrochem. Soc. **168**, 120504 (2021).
24. T. Q. Nguyen, and C. Breitkopf, J. Electrochem. Soc. **165**, E826-E831 (2018).
25. N. Meddings, M. Heinrich, F. Overney, J.-S. Lee, V. Ruiz, E. Napolitano, S. Seitz, G. Hinds, R. Raccichini, M. Gaberšček, and J. Park, J. Power Sources **480**, 228742 (2020).
26. N. A. Kaskhedikar, and J. Maier, Adv. Mater. **21**, 2664-2680 (2009).
27. K. Persson, V. A. Sethuraman, L. J. Hardwick, Y. Hinuma, Y. S. Meng, A. Van Der Ven, V. Srinivasan, R. Kostecki, and G. Ceder, J. Phys. Chem. Lett. **1**, 1176-1180 (2010).
28. M. S. Whittingham, Chem. Rev. **104**, 4271-4302 (2004).
29. M. S. Whittingham, Chem. Rev. **114**, 11414-11443 (2014).
30. J. B. Goodenough, J. Power Sources **174**, 996-1000 (2007).
31. J. B. Goodenough, and Y. Kim, Chem. Mater. **22**, 587-603 (2009).
32. S. P. Ong, V. L. Chevrier, G. Hautier, A. Jain, C. Moore, S. Kim, X. Ma, and G. Ceder, Energy Environ. Sci. **4**, 3680-3688 (2011).
33. G. Ceder, MRS Bull. **35**, 693-701 (2010).
34. M. D. Radin, S. Hy, M. Sina, C. Fang, H. Liu, J. Vinckeviciute, M. Zhang, M. S. Whittingham, Y. S. Meng, and A. Van der Ven, Adv. Energy Mater. **7**, 1602888 (2017).
35. J. Reed, and G. Ceder, Chem. Rev. **104**, 4513-4534 (2004).
36. P. Canepa, G. Sai Gautam, D. C. Hannah, R. Malik, M. Liu, K. G. Gallagher, K. A. Persson, and G. Ceder, Chem. Rev. **117**, 4287-4341 (2017).
37. M. Armand, and J.-M. Tarascon, Nature **451**, 652 (2008).
38. M. M. Thackeray, C. Wolverton, and E. D. Isaacs, Energy Environ. Sci. **5**, 7854-7863 (2012).
39. M. M. Thackeray, Prog. Solid State Chem. **25**, 1-71 (1997).
40. P. Simon, and Y. Gogotsi, Nature Mater. **7**, 845-854 (2008).
41. V. Augustyn, P. Simon, and B. Dunn, Energy Environ. Sci. **7**, 1597-1614 (2014).
42. J. Dahn, A. Sleigh, H. Shi, B. Way, W. Weydanz, J. Reimers, Q. Zhong, and U. Von Sacken, Industrial Chemistry Library Vol. **5**, ed. G. Pistoia (1994).
43. B. L. Ellis, K. T. Lee, and L. F. Nazar, Chem. Mater. **22**, 691-714 (2010).
44. V. Etacheri, R. Marom, R. Elazari, G. Salitra, and D. Aurbach, Energy Environ. Sci. **4**, 3243-3262 (2011).
45. J. W. Choi, and D. Aurbach, Nat. Rev. Mater. **1**, 16013 (2016).
46. M. Winter, J. O. Besenhard, M. E. Spahr, and P. Novak, Adv. Mater. **10**, 725-763 (1998).
47. M. Reddy, G. Subba Rao, and B. Chowdari, Chem. Rev. **113**, 5364-5457 (2013).

48. M. Winter, and R. J. Brodd, Chem. Rev. **10**, 4245-4270 (2004).
49. X. Yu, S. Yun, J. S. Yeon, P. Bhattacharya, L. Wang, S. W. Lee, X. Hu, and H. S. Park, Adv. Energy Mater. **8**, 1702930 (2018).
50. M. Weiss, R. Ruess, J. Kasnatscheew, Y. Levartovsky, N. R. Levy, P. Minnmann, L. Stolz, T. Waldmann, M. Wohlfahrt-Mehrens, D. Aurbach, M. Winter, Y. Ein-Eli, and J. Janek, Adv. Energy Mater. **11**, 2101126 (2021).
51. M. Park, X. Zhang, M. Chung, G. B. Less, and A. M. Sastry, J. Power Sources **195**, 7904-7929 (2010).
52. A. Van der Ven, J. Bhattacharya, and A. A. Belak, Accounts. Chem. Res. **46**, 1216-1225 (2012).
53. R. Gomer, Rep. Prog. Phys. **53**, 917 (1990).
54. K. Kanehori, F. Kirino, T. Kudo, and K. Miyauchi, J. Electrochem. Soc. **138**, 2216-2219 (1991).
55. H. Xia, L. Lu, Y. Meng, and G. Ceder, J. Electrochem. Soc. **154**, A337-A342 (2007).
56. P. Bruce, and M. Saidi, J. Solid State Chem. **88**, 411-418 (1990).
57. X.-C. Tang, L.-X. Li, Q.-L. Lai, X.-W. Song, and L.-H. Jiang, Electrochim. Acta **54**, 2329-2334 (2009).
58. M. D. Levi, and D. Aurbach, J. Phys. Chem. B **101**, 4641-4647 (1997).
59. Y. Bai, X. Wang, X. Zhang, H. Shu, X. Yang, B. Hu, Q. Wei, H. Wu, and Y. Song, Electrochim. Acta **109**, 355-364 (2013).
60. Y. H. Rho, and K. Kanamura, J. Solid State Chem. **177**, 2094-2100 (2004).
61. X.-C. Tang, X.-W. Song, P.-Z. Shen, and D.-Z. Jia, Electrochim. Acta **50**, 5581-5587 (2005).
62. M. S. Whittingham, Science **192**, 1126-1127 (1976).
63. J. N. Reimers, and J. Dahn, J. Electrochem. Soc. **139**, 2091-2097 (1992).
64. S. Sinha, and D. Murphy, Solid State Ionics **20**, 81-84 (1986).
65. L.-X. Yuan, Z.-H. Wang, W.-X. Zhang, X.-L. Hu, J.-T. Chen, Y.-H. Huang, and J. B. Goodenough, Energy Environ. Sci. **4**, 269-284 (2011).
66. J.-S. Filhol, C. Combelles, R. Yazami, and M.-L. Doublet, J. Phys. Chem. C **112**, 3982-3988 (2008).
67. S. Yang, X. Wang, X. Yang, Y. Bai, Z. Liu, H. Shu, and Q. Wei, Electrochim. Acta **66**, 88-93 (2012).
68. K. Colbow, J. Dahn, and R. Haering, J. Power Sources **26**, 397-402 (1989).
69. J. Reimers, and J. Dahn, Phys. Rev. B **47**, 2995 (1993).
70. A. Van der Ven, J. C. Thomas, Q. Xu, B. Swoboda, and D. Morgan, Phys. Rev. B **78**, 104306 (2008).
71. J. Dahn, and R. Haering, Solid State Commun. **40**, 245-248 (1981).
72. G. Amatucci, J. Tarascon, and L. Klein, J. Electrochem. Soc. **143**, 1114-1123 (1996).
73. A. Van der Ven, and G. Ceder, Electrochem. Solid-State Lett. **3**, 301-304 (2000).
74. Y. Lyu, X. Wu, K. Wang, Z. Feng, T. Cheng, Y. Liu, M. Wang, R. Chen, L. Xu, J. Zhou, Y. Lu, and B. Guo, Adv. Energy Mater. **11**, 2000982 (2021).
75. S. Castro-Garcıa, A. Castro-Couceiro, M. Senarıs-Rodrıguez, F. Soulette, and C. Julien, Solid State Ionics **156**, 15-26 (2003).
76. J. Bhattacharya, and A. Van der Ven, Phys. Rev. B **83**, 144302 (2011).
77. W. Küchler, P. Heitjans, A. Payer, and R. Schöllhorn, Solid State Ionics **70**, 434-438 (1994).
78. M. Wilkening, and P. Heitjans, Phys. Rev. B **77**, 024311 (2008).
79. M. Catti, Phys. Rev. B **61**, 1795 (2000).

80. C. Delmas, D. Carlier, and M. Guignard, Adv. Energy Mater. **11**, 2001201 (2021).
81. P. F. Wang, Y. You, Y. X. Yin, and Y. G. Guo, Adv. Energy Mater. **8**, 1701912 (2018).
82. A. Van der Ven, Z. Deng, S. Banerjee, and S. P. Ong, Chem. Rev. **120**, 6977-7019 (2020).
83. R. Jain, A. S. Lakhnot, K. Bhimani, S. Sharma, V. Mahajani, R. A. Panchal, M. Kamble, F. Han, C. Wang, and N. Koratkar, Nat. Rev. Mater. **7**, 736-746 (2022).
84. J. Yang, and J. S. Tse, J. Phys. Chem. A **115**, 13045-13049 (2011).
85. M. S. Islam, D. J. Driscoll, C. A. Fisher, and P. R. Slater, Chem. Mater. **17**, 5085-5092 (2005).
86. C. Ouyang, S. Shi, Z. Wang, X. Huang, and L. Chen, Phys. Rev. B **69**, 104303 (2004).
87. D. Morgan, A. Van der Ven, and G. Ceder, Electrochem. Solid-State Lett. **7**, A30-A32 (2004).
88. S.-i. Nishimura, G. Kobayashi, K. Ohoyama, R. Kanno, M. Yashima, and A. Yamada, Nature Mater. **7**, 707 (2008).
89. S.-Y. Chung, S.-Y. Choi, T. Yamamoto, and Y. Ikuhara, Phys. Rev. Lett. **100**, 125502 (2008).
90. R. Malik, D. Burch, M. Bazant, and G. Ceder, Nano Lett. **10**, 4123-4127 (2010).
91. J. Li, W. Yao, S. Martin, and D. Vaknin, Solid State Ionics **179**, 2016-2019 (2008).
92. P. P. Prosini, M. Lisi, D. Zane, and M. Pasquali, Solid State Ionics **148**, 45-51 (2002).
93. J. Xie, N. Imanishi, T. Zhang, A. Hirano, Y. Takeda, and O. Yamamoto, Electrochim. Acta **54**, 4631-4637 (2009).
94. A. K. Padhi, K. S. Nanjundaswamy, and J. B. Goodenough, J. Electrochem. Soc. **144**, 1188-1194 (1997).
95. C. Delmas, M. Maccario, L. Croguennec, F. Le Cras, and F. Weill, Nature Mater. **7**, 665 (2008).
96. L. Laffont, C. Delacourt, P. Gibot, M. Y. Wu, P. Kooyman, C. Masquelier, and J. M. Tarascon, Chem. Mater. **18**, 5520-5529 (2006).
97. A. Andersson, and J. O. Thomas, J. Power Sources **97**, 498-502 (2001).
98. F. Wang, K. Yang, M. Ge, J. Wang, J. Wang, X. Xiao, W.-K. Lee, L. Li, and M. Tang, ACS Energy Lett. **7**, 1648-1656 (2022).
99. T. Yoshinari, T. Mori, K. Otani, T. Munesada, K. Yamamoto, T. Uchiyama, K. Fukuda, Y. Koyama, R. Hagiwara, Y. Orikasa, and Y. Uchimoto, Chem. Mater. **31**, 7160-7166 (2019).
100. V. D. Sumanov, O. A. Tyablikov, A. V. Morozov, S. S. Fedotov, S. Y. Vassiliev, and V. A. Nikitina, Electrochim. Acta **368**, 137627 (2021).
101. T. Hatakeyama, H. Li, N. L. Okamoto, K. Shimokawa, T. Kawaguchi, H. Tanimura, S. Imashuku, M. Fichtner, and T. Ichitsubo, Chem. Mater. **33**, 6983-6996 (2021).
102. J. E. Post, Proc. Natl. Acad. Sci. **96**, 3447-3454 (1999).
103. D. A. Kitchaev, S. T. Dacek, W. Sun, and G. Ceder, J. Am. Chem. Soc. **139**, 2672-2681 (2017).
104. F. Jiao, and P. G. Bruce, Adv. Mater. **19**, 657-660 (2007).
105. S. Bach, J. Pereira-Ramos, and P. Willmann, Electrochim. Acta **56**, 10016-10022 (2011).
106. J. A. Dawson, and I. Tanaka, ACS Appl. Mater. Interfaces **7**, 8125-8131 (2015).
107. K. He, Y. Yuan, W. Yao, K. You, M. Dahbi, J. Alami, K. Amine, R. Shahbazian-Yassar, and J. Lu, Angew. Chem. Int. Ed. **61**, e202113420 (2022).
108. Y. Chabre, and J. Pannetier, Prog. Solid State Chem. **23**, 1-130 (1995).
109. P. K. Gupta, A. Bhandari, J. Bhattacharya, and R. G. S. Pala, J. Phys. Chem. C **122**, 11689-11700 (2018).
110. K. Hwang, C. Lee, T. Yoon, and Y. Son, J. Power Sources **79**, 225-230 (1999).
111. M. F. Dupont, A. D. Cross, A. Morel, M. Drozd, A. F. Hollenkamp, and S. W. Donne, J. Electrochem. Soc. **160**, A1219-A1231 (2013).

112. I. Vasiliev, B. A. Magar, J. Duay, T. N. Lambert, and B. Chalamala, J. Electrochem. Soc. **165**, A3517 (2018).
113. Y. Paik, W. Bowden, T. Richards, and C. P. Grey, J. Electrochem. Soc. **152**, A1539-A1547 (2005).
114. D. Qu, Electrochim. Acta **49**, 657-665 (2004).
115. C. Li, S. Jin, L. A. Archer, and L. F. Nazar, Joule **6**, 1733-1738 (2022).
116. X. Gao, H. Wu, W. Li, Y. Tian, Y. Zhang, H. Wu, L. Yang, G. Zou, H. Hou, and X. Ji, Small **16**, 1905842 (2020).
117. F. Wang, L. E. Blanc, Q. Li, A. Faraone, X. Ji, H. H. Chen-Mayer, R. L. Paul, J. A. Dura, E. Hu, K. Xu, L. F. Nazar, and C. Wang, Adv. Energy Mater. **11**, 2102016 (2021).
118. X. Jia, C. Liu, Z. G. Neale, J. Yang, and G. Cao, Chem. Rev. **120**, 7795-7866 (2020).
119. L. Li, T. K. A. Hoang, J. Zhi, M. Han, S. Li, and P. Chen, ACS Appl. Mater. Interfaces **12**, 12834-12846 (2020).
120. Y. Yuan, R. Sharpe, K. He, C. Li, M. T. Saray, T. Liu, W. Yao, M. Cheng, H. Jin, S. Wang, K. Amine, R. Shahbazian-Yassar, M. S. Islam, and J. Lu, Nat. Sustain. **5**, 890-898 (2022).
121. Y. Kadoma, S. Oshitari, K. Ui, and N. Kumagai, Electrochim. Acta **53**, 1697-1702 (2007).
122. L. M. Housel, L. Wang, A. Abraham, J. Huang, G. D. Renderos, C. D. Quilty, A. B. Brady, A. C. Marschilok, K. J. Takeuchi, and E. S. Takeuchi, Accounts. Chem. Res. **51**, 575-582 (2018).
123. R. Kempaiah, H. Chan, S. Srinivasan, S. K. R. S. Sankaranarayanan, B. Narayanan, and A. Subramanian, ACS Appl. Energy Mater. **4**, 12099-12111 (2021).
124. D. A. Tompsett, and M. S. Islam, Chem. Mater. **25**, 2515-2526 (2013).
125. S. Devaraj, and N. Munichandraiah, J. Phys. Chem. C **112**, 4406-4417 (2008).
126. M. Toupin, T. Brousse, and D. Bélanger, Chem. Mater. **16**, 3184-3190 (2004).
127. S.-L. Kuo, and N.-L. Wu, J. Electrochem. Soc. **153**, A1317-A1324 (2006).
128. W. Wei, X. Cui, W. Chen, and D. G. Ivey, Chem. Soc. Rev. **40**, 1697-1721 (2011).
129. M. J. Young, A. M. Holder, S. M. George, and C. B. Musgrave, Chem. Mater. **27**, 1172-1180 (2015).
130. R. Yazami, and P. Touzain, J. Power Sources **9**, 365-371 (1983).
131. A. M. Dimiev, K. Shukhina, N. Behabtu, M. Pasquali, and J. M. Tour, J. Phys. Chem. C **123**, 19246-19253 (2019).
132. L. Zhao, B. Ding, X.-Y. Qin, Z. Wang, W. Lv, Y.-B. He, Q.-H. Yang, and F. Kang, Adv. Mater. **34**, 2106704 (2022).
133. V. Meunier, J. Kephart, C. Roland, and J. Bernholc, Phys. Rev. Lett. **88**, 075506 (2002).
134. S. Thinius, M. M. Islam, P. Heitjans, and T. Bredow, J. Phys. Chem. C **118**, 2273-2280 (2014).
135. K. Toyoura, Y. Koyama, A. Kuwabara, F. Oba, and I. Tanaka, Phys. Rev. B **78**, 214303 (2008).
136. H. Yang, H. J. Bang, and J. Prakash, J. Electrochem. Soc. **151**, A1247-A1250 (2004).
137. J. Dahn, Phys. Rev. B **44**, 9170 (1991).
138. D. Billaud, F. Henry, M. Lelaurain, and P. Willmann, J. Phys. Chem. Solids **57**, 775-781 (1996).
139. Y. Imai, and A. Watanabe, J. Alloy. Compd. **439**, 258-267 (2007).
140. E. Lee, and K. A. Persson, Nano Lett. **12**, 4624-4628 (2012).
141. H. Yildirim, A. Kinaci, Z.-J. Zhao, M. K. Chan, and J. P. Greeley, ACS Appl. Mater. Interfaces **6**, 21141-21150 (2014).
142. P. V. Medeiros, F. de Brito Mota, A. J. Mascarenhas, and C. M. de Castilho, Nanotechnology **21**, 115701 (2010).

143. X. Fan, W. Zheng, and J.-L. Kuo, ACS Appl. Mater. Interfaces **4**, 2432-2438 (2012).
144. R. E. Mapasha, and N. Chetty, Comp. Mater. Sci. **49**, 787-791 (2010).
145. G. Wang, X. Shen, J. Yao, and J. Park, Carbon **47**, 2049-2053 (2009).
146. D. Pan, S. Wang, B. Zhao, M. Wu, H. Zhang, Y. Wang, and Z. Jiao, Chem. Mater. **21**, 3136-3142 (2009).
147. T. Bhardwaj, A. Antic, B. Pavan, V. Barone, and B. D. Fahlman, J. Am. Chem. Soc. **132**, 12556-12558 (2010).
148. E. Pollak, B. Geng, K.-J. Jeon, I. T. Lucas, T. J. Richardson, F. Wang, and R. Kostecki, Nano Lett. **10**, 3386-3388 (2010).
149. J. Zhou, Q. Sun, Q. Wang, and P. Jena, Phys. Rev. B **90**, 205427 (2014).
150. J. R. Dahn, T. Zheng, Y. Liu, and J. Xue, Science **270**, 590-593 (1995).
151. C. Uthaisar, and V. Barone, Nano Lett. **10**, 2838-2842 (2010).
152. E. G. Leggesse, C.-L. Chen, and J.-C. Jiang, Carbon **103**, 209-216 (2016).
153. F. Yao, F. Gunes, H. Q. Ta, S. M. Lee, S. J. Chae, K. Y. Sheem, C. S. Cojocaru, S. S. Xie, and Y. H. Lee, J. Am. Chem. Soc. **134**, 8646-8654 (2012).
154. L.-J. Zhou, Z. Hou, and L.-M. Wu, J. Phys. Chem. C **116**, 21780-21787 (2012).
155. A. G. Olabi, M. A. Abdelkareem, T. Wilberforce, and E. T. Sayed, Renew. Sust. Energ. Rev. **135**, 110026 (2021).
156. T. Gao, Y. Han, D. Fraggedakis, S. Das, T. Zhou, C.-N. Yeh, S. Xu, W. C. Chueh, J. Li, and M. Z. Bazant, Joule **5**, 393-414 (2021).
157. M. Kühne, F. Paolucci, J. Popovic, P. M. Ostrovsky, J. Maier, and J. H. Smet, Nat. Nanotechnol. **12**, 895-900 (2017).
158. X. Wang, Y.-L. Ding, Y.-P. Deng, and Z. Chen, Adv. Energy Mater. **10**, 1903864 (2020).
159. I. Baccouche, S. Jemmali, B. Manai, A. Nikolian, N. Omar, and N. Essoukri Ben Amara, Int. J. Energ. Res. **46**, 3843-3859 (2022).
160. J. Barker, R. Pynenburg, R. Koksbang, and M. Saidi, Electrochim. Acta **41**, 2481-2488 (1996).
161. M. Aydinol, A. Kohan, G. Ceder, K. Cho, and J. Joannopoulos, Phys. Rev. B **56**, 1354 (1997).
162. H. Li, N. Zhang, J. Li, and J. Dahn, J. Electrochem. Soc. **165**, A2985-A2993 (2018).
163. K. Kang, and G. Ceder, Phys. Rev. B **74**, 094105 (2006).
164. M. A. y de Dompablo, A. Van der Ven, and G. Ceder, Phys. Rev. B **66**, 064112 (2002).
165. A. Van der Ven, M. Aydinol, G. Ceder, G. Kresse, and J. Hafner, Phys. Rev. B **58**, 2975 (1998).
166. C. Wolverton, and A. Zunger, Phys. Rev. Lett. **81**, 606 (1998).
167. M. Broussely, F. Perton, P. Biensan, J. Bodet, J. Labat, A. Lecerf, C. Delmas, A. Rougier, and J. Peres, J. Power Sources **54**, 109-114 (1995).
168. A. Rougier, I. Saadoune, P. Gravereau, P. Willmann, and C. Delmasa, Solid State Ionics **90**, 83-90 (1996).
169. K. Nakamura, H. Ohno, K. Okamura, Y. Michihiro, I. Nakabayashi, and T. Kanashiro, Solid State Ionics **135**, 143-147 (2000).
170. J. Fan, and P. S. Fedkiw, J. Power Sources **72**, 165-173 (1998).
171. P. G. Bruce, A. Lisowska-Oleksiak, M. Y. Saidi, and C. A. Vincent, Solid State Ionics **57**, 353-358 (1992).
172. G. Cherkashinin, M. Motzko, N. Schulz, T. Späth, and W. Jaegermann, Chem. Mater. **27**, 2875-2887 (2015).
173. Y. Wei, J. Zheng, S. Cui, X. Song, Y. Su, W. Deng, Z. Wu, X. Wang, W. Wang, and M. Rao, J.

Am. Chem. Soc. **137**, 8364-8367 (2015).
174. P.-C. Tsai, B. Wen, M. Wolfman, M.-J. Choe, M. S. Pan, L. Su, K. Thornton, J. Cabana, and Y.-M. Chiang, Energy Environ. Sci. **11**, 860-871 (2018).
175. E. E. Levin, S. Y. Vassiliev, and V. A. Nikitina, Electrochim. Acta **228**, 114-124 (2017).
176. R. Amin, and Y.-M. Chiang, J. Electrochem. Soc. **163**, A1512-A1517 (2016).
177. R. Malik, A. Abdellahi, and G. Ceder, J. Electrochem. Soc. **160**, A3179-A3197 (2013).
178. J. Bhattacharya, and A. Van der Ven, Phys. Rev. B **81**, 104304 (2010).
179. T. Ohzuku, A. Ueda, and N. Yamamoto, J. Electrochem. Soc. **142**, 1431-1435 (1995).
180. H. Zhang, Y. Yang, H. Xu, L. Wang, X. Lu, and X. He, InfoMat **4**, e12228 (2022).
181. S. Natarajan, K. Subramanyan, and V. Aravindan, Small **15**, 1904484 (2019).
182. M. M. Thackeray, J. Am. Ceram. Soc. **82**, 3347-3354 (1999).
183. W. Liu, K. Kowal, and G. Farrington, J. Electrochem. Soc. **145**, 459-465 (1998).
184. T. Ohzuku, M. Kitagawa, and T. Hirai, J. Electrochem. Soc. **137**, 769-775 (1990).
185. M. Mohamedi, D. Takahashi, T. Uchiyama, T. Itoh, M. Nishizawa, and I. Uchida, J. Power Sources **93**, 93-103 (2001).
186. E. Deiss, Electrochim. Acta **47**, 4027-4034 (2002).
187. A.-K. Hjelm, and G. Lindbergh, Electrochim. Acta **47**, 1747-1759 (2002).
188. B. Xu, and S. Meng, J. Power Sources **195**, 4971-4976 (2010).
189. J. Molenda, J. Marzec, K. Świerczek, D. Pałubiak, W. Ojczyk, and M. Ziemnicki, Solid State Ionics **175**, 297-304 (2004).
190. M. Wakihara, L. Guohua, H. Ikuta, and T. Uchida, Solid State Ionics **86**, 907-909 (1996).
191. M. Nakayama, M. Kaneko, and M. Wakihara, Phys. Chem. Chem. Phys. **14**, 13963-13970 (2012).
192. R. Tyagi, A. Lanjan, and S. Srinivasan, ChemElectroChem **9**, e202101626 (2022).
193. H. Gu, G. Wang, C. Zhu, Y. Hu, X. Zhang, W. Wen, X. Yang, B. Wang, X. Gao, X. Zhan, J. Li, Z.-F. Ma, and Q. He, Electrochim. Acta **298**, 806-817 (2019).
194. M. Eckhoff, P. E. Blöchl, and J. Behler, Phys. Rev. B **101**, 205113 (2020).
195. M. Naguib, M. Kurtoglu, V. Presser, J. Lu, J. Niu, M. Heon, L. Hultman, Y. Gogotsi, and M. W. Barsoum, Adv. Mater. **23**, 4248-4253 (2011).
196. L. Li, J. Wen, and X. Zhang, ChemSusChem **13**, 1296-1329 (2020).
197. M. Naguib, M. W. Barsoum, and Y. Gogotsi, Adv. Mater. **33**, 2103393 (2021).
198. K. R. G. Lim, M. Shekhirev, B. C. Wyatt, B. Anasori, Y. Gogotsi, and Z. W. Seh, Nat. Synth. **1**, 601-614 (2022).
199. M. Ghidiu, M. R. Lukatskaya, M.-Q. Zhao, Y. Gogotsi, and M. W. Barsoum, Nature **516**, 78-81 (2014).
200. N. C. Osti, M. Naguib, A. Ostadhossein, Y. Xie, P. R. C. Kent, B. Dyatkin, G. Rother, W. T. Heller, A. C. T. van Duin, Y. Gogotsi, and E. Mamontov, ACS Appl. Mater. Interfaces **8**, 8859-8863 (2016).
201. M. Boota, B. Anasori, C. Voigt, M. Q. Zhao, M. W. Barsoum, and Y. Gogotsi, Adv. Mater. **28**, 1517-1522 (2016).
202. J. Wen, X. T. Zhang, and H. Gao, Physica B **537**, 155-161 (2018).
203. J. Wen, Q. Fu, W. Wu, H. Gao, X. Zhang, and B. Wang, ACS Appl. Mater. Interfaces **11**, 7087-7095 (2019).
204. J. Wen, X. T. Zhang, and H. Gao, Phys. Chem. Chem. Phys. **19**, 9509-9518 (2017).
205. M. Okubo, A. Sugahara, S. Kajiyama, and A. Yamada, Accounts. Chem. Res. **51**, 591-599 (2018).

206. M. R. Lukatskaya, S. Kota, Z. Lin, M.-Q. Zhao, N. Shpigel, M. D. Levi, J. Halim, P.-L. Taberna, M. W. Barsoum, and P. Simon, Nat. Energy **2**, 17105 (2017).
207. A. R. Armstrong, and P. G. Bruce, Nature **381**, 499 (1996).
208. Y. Shao‐Horn, S. Hackney, A. Armstrong, P. Bruce, R. Gitzendanner, C. Johnson, and M. Thackeray, J. Electrochem. Soc. **146**, 2404-2412 (1999).
209. M. Nakayama, T. Kanaya, J.-W. Lee, and B. N. Popov, J. Power Sources **179**, 361-366 (2008).
210. H. Kanoh, W. Tang, Y. Makita, and K. Ooi, Langmuir **13**, 6845-6849 (1997).
211. N. C. Bartelt, Y. Li, J. D. Sugar, K. Fenton, A. L. D. Kilcoyne, D. A. Shapiro, T. Tyliszczak, W. C. Chueh, and F. El Gabaly, Phys. Rev. Appl. **10**, 044056 (2018).
212. G. Chen, X. Song, and T. J. Richardson, Electrochem. Solid-State Lett. **9**, A295-A298 (2006).
213. B. Ellis, L. K. Perry, D. H. Ryan, and L. Nazar, J. Am. Chem. Soc. **128**, 11416-11422 (2006).
214. K. Striebel, J. Shim, V. Srinivasan, and J. Newman, J. Electrochem. Soc. **152**, A664-A670 (2005).
215. N. Daumas, and A. Herold, Comptes Rendus Hebdomadaires Des Seances De L Academie Des Sciences Serie C **268**, 373 (1969).
216. D. Allart, M. Montaru, and H. Gualous, J. Electrochem. Soc. **165**, A380-A387 (2018).
217. A. Funabiki, M. Inaba, T. Abe, and Z. Ogumi, J. Electrochem. Soc. **146**, 2443-2448 (1999).
218. H. He, C. Huang, C.-W. Luo, J.-J. Liu, and Z.-S. Chao, Electrochim. Acta **92**, 148-152 (2013).
219. Y.-H. Kao, M. Tang, N. Meethong, J. Bai, W. C. Carter, and Y.-M. Chiang, Chem. Mater. **22**, 5845-5855 (2010).
220. Y.-M. Chiang, Science **330**, 1485-1486 (2010).
221. S.-I. Pyun, and Y.-G. Ryu, J. Power Sources **70**, 34-39 (1998).
222. S. H. A. Axdal, and D. D. L. Chung, Carbon **25**, 377-389 (1987).
223. J. Dahn, and W. McKinnon, J. Phys. C: Solid State Phys. **17**, 4231 (1984).
224. W. Li, J. Reimers, and J. Dahn, Phys. Rev. B **46**, 3236 (1992).
225. C. Wolverton, and A. Zunger, Phys. Rev. Lett. **81**, 606 (1998).
226. A. Van der Ven, G. Ceder, M. Asta, and P. Tepesch, Phys. Rev. B **64**, 184307 (2001).
227. M. Ménétrier, I. Saadoune, S. Levasseur, and C. Delmas, J. Mater. Chem. **9**, 1135-1140 (1999).
228. J. Molenda, A. Stokłosa, and T. Bąk, Solid State Ionics **36**, 53-58 (1989).
229. A. Milewska, K. Świerczek, J. Tobola, F. Boudoire, Y. Hu, D. Bora, B. Mun, A. Braun, and J. Molenda, Solid State Ionics **263**, 110-118 (2014).
230. N. Nadkarni, T. Zhou, D. Fraggedakis, T. Gao, and M. Z. Bazant, Adv. Funct. Mater. **29**, 1902821 (2019).
231. L. Liang, J. Zhang, Y. Zhou, J. Xie, X. Zhang, M. Guan, B. Pan, and Y. Xie, Sci. Rep. **3**, 1936 (2013).
232. J. B. Mitchell, W. C. Lo, A. Genc, J. LeBeau, and V. Augustyn, Chem. Mater. **29**, 3928-3937 (2017).
233. D. Belitz, and T. Kirkpatrick, Rev. Mod. Phys. **66**, 261 (1994).
234. M. Imada, A. Fujimori, and Y. Tokura, Rev. Mod. Phys. **70**, 1039 (1998).
235. M. Pollak, Eur. Phys. J. Spec. Top. **227**, 2221-2240 (2019).
236. D. Unruh, A. Camjayi, C. Hansen, J. Bobadilla, M. J. Rozenberg, and G. T. Zimanyi, Nano Lett. **20**, 8569-8575 (2020).
237. C. A. Marianetti, G. Kotliar, and G. Ceder, Nature Mater. **3**, 627 (2004).
238. M. Levi, G. Salitra, B. Markovsky, H. Teller, D. Aurbach, U. Heider, and L. Heider, J. Electrochem. Soc. **146**, 1279-1289 (1999).

239. J. M. McGraw, C. S. Bahn, P. A. Parilla, J. D. Perkins, D. W. Readey, and D. S. Ginley, Electrochim. Acta **45**, 187-196 (1999).
240. G. Hasegawa, N. Kuwata, Y. Tanaka, T. Miyazaki, N. Ishigaki, K. Takada, and J. Kawamura, Phys. Chem. Chem. Phys. **23**, 2438-2448 (2021).
241. J. Yan, S. Li, B. Lan, Y. Wu, and P. S. Lee, Adv. Funct. Mater. **30**, 1902564 (2020).
242. L. S. Roselin, R.-S. Juang, C.-T. Hsieh, S. Sagadevan, A. Umar, R. Selvin, and H. H. Hegazy, Materials **12**, 1229 (2019).
243. L. Yu, X. Zhou, L. Lu, X. Wu, and F. Wang, ChemSusChem **13**, 5361-5407 (2020).
244. A. Aricò, P. Bruce, B. Scrosati, J. Tarascon, and W. van Schalkwijk, Nature Mater. **4**, 366 (2005).
245. K. Zaghib, G. Nadeau, and K. Kinoshita, J. Electrochem. Soc. **147**, 2110-2115 (2000).
246. Y. Oumellal, N. Delpuech, D. Mazouzi, N. Dupre, J. Gaubicher, P. Moreau, P. Soudan, B. Lestriez, and D. Guyomard, J. Mater. Chem. **21**, 6201-6208 (2011).
247. M. Okubo, E. Hosono, J. Kim, M. Enomoto, N. Kojima, T. Kudo, H. Zhou, and I. Honma, J. Am. Chem. Soc. **129**, 7444-7452 (2007).
248. F. Wang, J. Graetz, M. S. Moreno, C. Ma, L. Wu, V. Volkov, and Y. Zhu, ACS Nano **5**, 1190-1197 (2011).
249. J. C. Hunter, J. Solid State Chem. **39**, 142-147 (1981).
250. Y. Wang, L. Chen, Y. Wang, and Y. Xia, Electrochim. Acta **173**, 178-183 (2015).
251. A. Bhandari, and J. Bhattacharya, J. Electrochem. Soc. **164**, A106-A127 (2017).
252. M. Wagemaker, F. M. Mulder, and A. Van der Ven, Adv. Mater. **21**, 2703-2709 (2009).
253. A. Van der Ven, K. Garikipati, S. Kim, and M. Wagemaker, J. Electrochem. Soc. **156**, A949-A957 (2009).
254. N. Meethong, H.-Y. S. Huang, W. C. Carter, and Y.-M. Chiang, Electrochem. Solid-State Lett. **10**, A134-A138 (2007).
255. J. Dodd, R. Yazami, and B. Fultz, Electrochem. Solid-State Lett. **9**, A151-A155 (2006).
256. R. W. Balluffi, S. Allen, and W. C. Carter, *Kinetics of Materials*, John Wiley & Sons (2005).
257. N. Meethong, Y.-H. Kao, M. Tang, H.-Y. Huang, W. C. Carter, and Y.-M. Chiang, Chem. Mater. **20**, 6189-6198 (2008).
258. D. A. Cogswell, and M. Z. Bazant, ACS Nano **6**, 2215-2225 (2012).
259. P. Gibot, M. Casas-Cabanas, L. Laffont, S. Levasseur, P. Carlach, S. Hamelet, J.-M. Tarascon, and C. Masquelier, Nature Mater. **7**, 741 (2008).
260. M. Okubo, Y. Mizuno, H. Yamada, J. Kim, E. Hosono, H. Zhou, T. Kudo, and I. Honma, ACS Nano **4**, 741-752 (2010).
261. P. Simon, Y. Gogotsi, and B. Dunn, Science **343**, 1210-1211 (2014).
262. C. Costentin, T. R. Porter, and J.-M. Savéant, ACS Appl. Mater. Interfaces **9**, 8649-8658 (2017).
263. B. Anasori, M. R. Lukatskaya, and Y. Gogotsi, Nat. Rev. Mater. **2**, 16098 (2017).
264. J. Chmiola, G. Yushin, Y. Gogotsi, C. Portet, P. Simon, and P.-L. Taberna, Science **313**, 1760-1763 (2006).
265. M. Salanne, B. Rotenberg, K. Naoi, K. Kaneko, P.-L. Taberna, C. P. Grey, B. Dunn, and P. Simon, Nat. Energy **1**, 16070 (2016).
266. T. C. Liu, W. Pell, B. Conway, and S. Roberson, J. Electrochem. Soc. **145**, 1882-1888 (1998).
267. J. Wang, J. Polleux, J. Lim, and B. Dunn, J. Phys. Chem. C **111**, 14925-14931 (2007).
268. Y. Shao, M. F. El-Kady, J. Sun, Y. Li, Q. Zhang, M. Zhu, H. Wang, B. Dunn, and R. B. Kaner, Chem. Rev. **118**, 9233-9280 (2018).

269. J. Wen, W. Zhang, L. Zhang, X. Zhang, and Y.-X. Yu, Chem. Phys. Lett. **775**, 138666 (2021).
270. C. Delacourt, P. Poizot, S. Levasseur, and C. Masquelier, Electrochem. Solid-State Lett. **9**, A352-A355 (2006).
271. M. Konarova, and I. Taniguchi, J. Power Sources **195**, 3661-3667 (2010).
272. H. Huang, S.-C. Yin, and L. s. Nazar, Electrochem. Solid-State Lett. **4**, A170-A172 (2001).
273. A. Jansen, A. Kahaian, K. Kepler, P. Nelson, K. Amine, D. Dees, D. Vissers, and M. Thackeray, J. Power Sources **81**, 902-905 (1999).
274. A. Birrozzi, M. Copley, J. von Zamory, M. Pasqualini, S. Calcaterra, F. Nobili, A. Di Cicco, H. Rajantie, M. Briceno, and E. Bilbé, J. Electrochem. Soc. **162**, A2331-A2338 (2015).
275. S. Goriparti, E. Miele, F. De Angelis, E. Di Fabrizio, R. P. Zaccaria, and C. Capiglia, J. Power Sources **257**, 421-443 (2014).
276. X. Zhao, and V.-P. Lehto, Nanotechnology **32**, 042002 (2021).
277. N. Balke, S. Jesse, A. Morozovska, E. Eliseev, D. Chung, Y. Kim, L. Adamczyk, R. Garcia, N. Dudney, and S. Kalinin, Nat. Nanotechnol. **5**, 749 (2010).
278. J. Xie, N. Imanishi, T. Matsumura, A. Hirano, Y. Takeda, and O. Yamamoto, Solid State Ionics **179**, 362-370 (2008).
279. D. Kramer, and G. Ceder, Chem. Mater. **21**, 3799-3809 (2009).
280. T. Tran, and K. Kinoshita, J. Electroanal. Chem. **386**, 221-224 (1995).
281. J. Wang, Y.-J. Gu, W.-L. Kong, H.-Q. Liu, Y.-B. Chen, and W. Liu, Solid State Ionics **327**, 11-17 (2018).
282. S. Ferrari, R. L. Lavall, D. Capsoni, E. Quartarone, A. Magistris, P. Mustarelli, and P. Canton, J. Phys. Chem. C **114**, 12598-12603 (2010).
283. Y. Zhao, L. Peng, B. Liu, and G. Yu, Nano Lett. **14**, 2849-2853 (2014).
284. B.-Y. Chang, and S.-M. Park, Annu. Rev. Anal. Chem. **3**, 207-229 (2010).
285. Z. Ogumi, Electrochemistry **78**, 319-324 (2010).
286. W. McKinnon, and R. Haering, Physical Mechanisms of Intercalation. In Modern Aspects of Electrochemistry, Springer, pp 235-304 (1983).
287. A. J. Bard, H. D. Abruna, C. E. Chidsey, L. R. Faulkner, S. W. Feldberg, K. Itaya, M. Majda, O. Melroy, and R. W. Murray, J. Phys. Chem. **97**, 7147-7173 (1993).
288. E. Laviron, J. Electroanal. Chem. **101**, 19-28 (1979).
289. L. R. Faulkner, and A. J. Bard, *Electrochemical Methods: Fundamentals and Applications*, John Wiley & Sons (2002).
290. M. Levi, and D. Aurbach, Electrochim. Acta **45**, 167-185 (1999).
291. Y. Yamada, Y. Iriyama, T. Abe, and Z. Ogumi, Langmuir **25**, 12766-12770 (2009).
292. S. Y. Vassiliev, V. V. Sentyurin, E. E. Levin, and V. A. Nikitina, Electrochim. Acta **302**, 316-326 (2019).
293. N. Takami, A. Satoh, M. Hara, and T. Ohsaki, J. Electrochem. Soc. **142**, 371-379 (1995).
294. A. Funabiki, M. Inaba, Z. Ogumi, S. i. Yuasa, J. Otsuji, and A. Tasaka, J. Electrochem. Soc. **145**, 172-178 (1998).
295. T. Piao, S. M. Park, C. H. Doh, and S. I. Moon, J. Electrochem. Soc. **146**, 2794-2798 (1999).
296. P. Yu, B. N. Popov, J. A. Ritter, and R. E. White, J. Electrochem. Soc. **146**, 8-14 (1999).
297. M. W. Verbrugge, and B. J. Koch, J. Electrochem. Soc. **150**, A374-A384 (2003).
298. M. Umeda, K. Dokko, Y. Fujita, M. Mohamedi, I. Uchida, and J. Selman, Electrochim. Acta **47**, 885-890 (2001).

299. M. Dresselhaus, and G. Dresselhaus, Adv. Phys. **30**, 139-326 (1981).
300. E. McRae, D. Billaud, J. Mareche, and A. Herold, Physica B+C **99**, 489-493 (1980).
301. L. Fu, H. Liu, C. Li, Y. P. Wu, E. Rahm, R. Holze, and H. Wu, Solid State Sci. **8**, 113-128 (2006).
302. R. Winter, and P. Heitjans, J. Phys. Chem. B **105**, 6108-6115 (2001).
303. F. Sauvage, E. Baudrin, L. Gengembre, and J.-M. Tarascon, Solid State Ionics **176**, 1869-1876 (2005).
304. C. Fongy, A.-C. Gaillot, S. Jouanneau, D. Guyomard, and B. Lestriez, J. Electrochem. Soc. **157**, A885-A891 (2010).
305. R. Amin, J. Maier, P. Balaya, D. Chen, and C. Lin, Solid State Ionics **179**, 1683-1687 (2008).
306. C. Delacourt, L. Laffont, R. Bouchet, C. Wurm, J.-B. Leriche, M. Morcrette, J.-M. Tarascon, and C. Masquelier, J. Electrochem. Soc. **152**, A913-A921 (2005).
307. C. Zhu, K. Weichert, and J. Maier, Adv. Funct. Mater. **21**, 1917-1921 (2011).
308. P. S. Herle, B. Ellis, N. Coombs, and L. F. Nazar, Nature Mater. **3**, 147 (2004).
309. T. Maxisch, F. Zhou, and G. Ceder, Phys. Rev. B **73**, 104301 (2006).
310. C. Wang, and J. Hong, Electrochem. Solid-State Lett. **10**, A65-A69 (2007).
311. J. Vetter, P. Novák, M. R. Wagner, C. Veit, K.-C. Möller, J. Besenhard, M. Winter, M. Wohlfahrt-Mehrens, C. Vogler, and A. Hammouche, J. Power Sources **147**, 269-281 (2005).
312. A. Yanagita, T. Shibata, W. Kobayashi, and Y. Moritomo, APL Mater. **3**, 106104 (2015).
313. N. Perez, *Electrochemistry and Corrosion Science*, Springer, Vol. 412 (2004).
314. E. C. Self, E. C. McRen, R. Wycisk, and P. N. Pintauro, Electrochim. Acta **214**, 139-146 (2016).
315. M. Metzger, J. Sicklinger, D. Haering, C. Kavakli, C. Stinner, C. Marino, and H. A. Gasteiger, J. Electrochem. Soc. **162**, A1227-A1235 (2015).
316. N. Besnard, A. Etiemble, T. Douillard, O. Dubrunfaut, P. Tran‐Van, L. Gautier, S. Franger, J. C. Badot, E. Maire, and B. Lestriez, Adv. Energy Mater. **7**, 1602239 (2017).
317. N. Holzwarth, S. G. Louie, and S. Rabii, Phys. Rev. B **28**, 1013 (1983).
318. A. Shellikeri, V. Watson, D. Adams, E. Kalu, J. Read, T. Jow, J. Zheng, and J. Zheng, J. Electrochem. Soc. **164**, A3914-A3924 (2017).
319. L. Bernard, W. Glaunsinger, and P. Colombet, Solid State Ionics **17**, 81-89 (1985).
320. B. E. Conway, *Electrochemical Supercapacitors: Scientific Fundamentals and Technological Applications*, Springer Science & Business Media, (2013).
321. R. A. Marcus, Rev. Mod. Phys. **65**, 599 (1993).
322. K. V. Mikkelsen, and M. A. Ratner, Chem. Rev. **87**, 113-153 (1987).
323. K. Zaghib, A. Mauger, J. B. Goodenough, F. Gendron, and C. Julien, Chem. Mater. **19**, 3740-3747 (2007).
324. J. Lee, J. B. Ju, W. I. Cho, B. W. Cho, and S. H. Oh, Electrochim. Acta **112**, 138-143 (2013).
325. K. W. Nam, S. Kim, E. Yang, Y. Jung, E. Levi, D. Aurbach, and J. W. Choi, Chem. Mater. **27**, 3721-3725 (2015).
326. E. Levi, Y. Gofer, and D. Aurbach, Chem. Mater. **22**, 860-868 (2009).
327. X. Wang, Q. Fu, J. Wen, X. Ma, C. Zhu, X. Zhang, and D. Qi, Nanoscale **10**, 20828-20835 (2018).
328. Y. Ando, M. Okubo, A. Yamada, and M. Otani, Adv. Funct. Mater. **30**, 2000820 (2020).
329. H. Shao, K. Xu, Y.-C. Wu, A. Iadecola, L. Liu, H. Ma, L. Qu, E. Raymundo-Piñero, J. Zhu, Z. Lin, P.-L. Taberna, and P. Simon, ACS Energy Lett. **5**, 2873-2880 (2020).
330. D. Pech, M. Brunet, H. Durou, P. Huang, V. Mochalin, Y. Gogotsi, P.-L. Taberna, and P. Simon,

Nat. Nanotechnol. **5**, 651 (2010).
331. R. Dominko, M. Bele, M. Gaberscek, M. Remskar, D. Hanzel, S. Pejovnik, and J. Jamnik, J. Electrochem. Soc. **152**, A607-A610 (2005).
332. C. T. Love, A. Korovina, C. J. Patridge, K. E. Swider-Lyons, M. E. Twigg, and D. E. Ramaker, J. Electrochem. Soc. **160**, A3153-A3161 (2013).
333. C. Kim, N. S. Norberg, C. T. Alexander, R. Kostecki, and J. Cabana, Adv. Funct. Mater. **23**, 1214-1222 (2013).
334. B. Zhao, R. Ran, M. Liu, and Z. Shao, Mater. Sci. Eng. R Rep. **98**, 1-71 (2015).
335. J. Lüchtefeld, H. Hemmelmann, S. Wachs, K. J. Mayrhofer, M. T. Elm, and B. B. Berkes, J. Phys. Chem. C **126**, 17204-17211 (2022).
336. G. Zhuang, P. N. Ross, F. p. Kong, and F. McLarnon, J. Electrochem. Soc. **145**, 159-164 (1998).
337. U. Heider, R. Oesten, and M. Jungnitz, J. Power Sources **81**, 119-122 (1999).
338. D. Aurbach, I. Weissman, A. Zaban, and P. Dan, Electrochim. Acta **45**, 1135-1140 (1999).
339. D. Aurbach, A. Zaban, Y. Ein-Eli, I. Weissman, O. Chusid, B. Markovsky, M. Levi, E. Levi, A. Schechter, and E. Granot, J. Power Sources **68**, 91-98 (1997).
340. L. Fu, H. Zhang, Y. Wu, H. Wu, and R. Holze, Electrochem. Solid-State Lett. **8**, A456-A458 (2005).
341. T. Kawamura, A. Kimura, M. Egashira, S. Okada, and J.-I. Yamaki, J. Power Sources **104**, 260-264 (2002).
342. Z. Yang, D. C. Ford, J. S. Park, Y. Ren, S. Kim, H. Kim, T. T. Fister, M. K. Chan, and M. M. Thackeray, Chem. Mater. **29**, 1507-1517 (2017).
343. P. Ruetschi, J. Electrochem. Soc. **131**, 2737-2744 (1984).
344. J. Lee, C. Newnham, F. Stone, and F. Tye, J. Colloid Interface Sci. **45**, 289-294 (1973).
345. P. Le Goff, N. Baffier, S. Bach, and J.-P. Pereira-Ramos, J. Mater. Chem. **4**, 133-137 (1994).
346. S. Bach, J. Pereira-Ramos, and N. Baffier, Solid State Ionics **80**, 151-158 (1995).
347. S. Bach, J. Pereira-Ramos, N. Baffier, and R. Messina, Electrochim. Acta **36**, 1595-1603 (1991).
348. Y. Wang, H. Shang, T. Chou, and G. Cao, J. Phys. Chem. B **109**, 11361-11366 (2005).
349. S. Tepavcevic, Y. Liu, D. Zhou, B. Lai, J. Maser, X. Zuo, H. Chan, P. Král, C. S. Johnson, and V. Stamenkovic, ACS Nano **9**, 8194-8205 (2015).
350. D. Söllinger, G. J. Redhammer, J. Schoiber, G. A. Zickler, and S. Pokrant, Electrochim. Acta **434**, 141294 (2022).
351. R. Wang, S. Boyd, P. V. Bonnesen, and V. Augustyn, J. Power Sources **477**, 229015 (2020).
352. J. Song, M. Noked, E. Gillette, J. Duay, G. Rubloff, and S. B. Lee, Phys. Chem. Chem. Phys. **17**, 5256-5264 (2015).
353. J. Dai, S. F. Li, K. S. Siow, and Z. Gao, Electrochim. Acta **45**, 2211-2217 (2000).
354. R. Chitrakar, H. Kanoh, Y. Miyai, and K. Ooi, Chem. Mater. **12**, 3151-3157 (2000).
355. Q. Feng, Y. Miyai, H. Kanoh, and K. Ooi, Langmuir **8**, 1861-1867 (1992).
356. P. Novak, and J. Desilvestro, J. Electrochem. Soc. **140**, 140-144 (1993).
357. X. Sun, V. Duffort, B. L. Mehdi, N. D. Browning, and L. F. Nazar, Chem. Mater. **28**, 534-542 (2016).
358. M. Spahr, P. Novak, O. Haas, and R. Nesper, J. Power Sources **54**, 346-351 (1995).
359. K. W. Nam, S. Kim, S. Lee, M. Salama, I. Shterenberg, Y. Gofer, J.-S. Kim, E. Yang, C. S. Park, and J.-S. Kim, Nano Lett. **15**, 4071-4079 (2015).
360. N. Sa, T. L. Kinnibrugh, H. Wang, G. Sai Gautam, K. W. Chapman, J. T. Vaughey, B. Key, T. T.

Fister, J. W. Freeland, and D. L. Proffit, Chem. Mater. **28**, 2962-2969 (2016).
361. N. Nakayama, T. Nozawa, Y. Iriyama, T. Abe, Z. Ogumi, and K. Kikuchi, J. Power Sources **174**, 695-700 (2007).
362. Q. Gao, W. Sun, P. Ilani-Kashkouli, A. Tselev, P. R. C. Kent, N. Kabengi, M. Naguib, M. Alhabeb, W.-Y. Tsai, A. P. Baddorf, J. Huang, S. Jesse, Y. Gogotsi, and N. Balke, Energy Environ. Sci. **13**, 2549-2558 (2020).
363. H.-W. Wang, M. Naguib, K. Page, D. J. Wesolowski, and Y. Gogotsi, Chem. Mater. **28**, 349-359 (2016).
364. M.-Q. Zhao, C. E. Ren, M. Alhabeb, B. Anasori, M. W. Barsoum, and Y. Gogotsi, ACS Appl. Energy Mater. **2**, 1572-1578 (2019).
365. T. S. Arthur, R. Zhang, C. Ling, P.-A. Glans, X. Fan, J. Guo, and F. Mizuno, ACS Appl. Mater. Interfaces **6**, 7004-7008 (2014).
366. Y. Wang, J. Yi, and Y. Xia, Adv. Energy Mater. **2**, 830-840 (2012).
367. Y. Sun, Z. Lian, Z. Ren, Z. Yao, Y. Yin, P. Huai, F. Zhu, Y. Huang, W. Wen, X. Li, R. Tai, and D. Zhu, ACS Nano **15**, 14766-14775 (2021).
368. B. E. Conway, J. Electrochem. Soc. **138**, 1539-1548 (1991).
369. Y. Gogotsi, and R. M. Penner, ACS Nano **12**, 2081-2083 (2018).
370. M. Z. Iqbal, S. Zakar, and S. S. Haider, J. Electroanal. Chem. **858**, 113793 (2020).
371. L. L. Zhang, and X. Zhao, Chem. Soc. Rev. **38**, 2520-2531 (2009).
372. P. Simon, and A. Burke, Electrochem. Soc. Interface **17**, 38 (2008).
373. S. Rasul, S. Suzuki, S. Yamaguchi, and M. Miyayama, Solid State Ionics **225**, 542-546 (2012).
374. H. Kurihara, T. Yajima, and S. Suzuki, Chem. Lett. **37**, 376-377 (2008).
375. X. Sun, P. Bonnick, V. Duffort, M. Liu, Z. Rong, K. A. Persson, G. Ceder, and L. F. Nazar, Energy Environ. Sci. **9**, 2273-2277 (2016).
376. Y. Gu, Y. Katsura, T. Yoshino, H. Takagi, and K. Taniguchi, Sci. Rep. **5**, 12486 (2015).
377. D. Aurbach, Z. Lu, A. Schechter, Y. Gofer, H. Gizbar, R. Turgeman, Y. Cohen, M. Moshkovich, and E. Levi, Nature **407**, 724 (2000).
378. T. E. Sutto, and T. T. Duncan, Electrochim. Acta **80**, 413-417 (2012).
379. T. E. Sutto, and T. T. Duncan, Electrochim. Acta **79**, 170-174 (2012).
380. M. Yan, P. He, Y. Chen, S. Wang, Q. Wei, K. Zhao, X. Xu, Q. An, Y. Shuang, and Y. Shao, Adv. Mater. **30**, 1703725 (2018).
381. C. Xu, B. Li, H. Du, and F. Kang, Angew. Chem. Int. Ed. **51**, 933-935 (2012).
382. M. H. Alfaruqi, V. Mathew, J. Gim, S. Kim, J. Song, J. P. Baboo, S. H. Choi, and J. Kim, Chem. Mater. **27**, 3609-3620 (2015).
383. L. Tian, and A. Yuan, J. Power Sources **192**, 693-697 (2009).
384. J. Zheng, P. Cygan, and T. Jow, J. Electrochem. Soc. **142**, 2699-2703 (1995).
385. J. P. Zheng, Electrochem. Solid-State Lett. **2**, 359-361 (1999).
386. S. Okashy, M. Noked, T. Zimrin, and D. Aurbach, J. Electrochem. Soc. **160**, A1489-A1496 (2013).
387. S. Patil, A. Harle, S. Sathaye, and K. Patil, CrystEngComm **16**, 10845-10855 (2014).
388. Y. Zhu, C. Cao, S. Tao, W. Chu, Z. Wu, and Y. Li, Sci. Rep. **4**, 5787 (2014).
389. V. Augustyn, J. Come, M. A. Lowe, J. W. Kim, P.-L. Taberna, S. H. Tolbert, H. D. Abruña, P. Simon, and B. Dunn, Nature Mater. **12**, 518 (2013).
390. M. Jayalakshmi, M. Mohan Rao, and F. Scholz, Langmuir **19**, 8403-8408 (2003).

391. B. J. Hertzberg, A. Huang, A. Hsieh, M. Chamoun, G. Davies, J. K. Seo, Z. Zhong, M. Croft, C. Erdonmez, and Y. S. Meng, Chem. Mater. **28**, 4536-4545 (2016).
392. M. Minakshi, P. Singh, M. Carter, and K. Prince, Electrochem. Solid-State Lett. **11**, A145-A149 (2008).
393. N. Agmon, Chem. Phys. Lett. **244**, 456-462 (1995).
394. T. J. Day, U. W. Schmitt, and G. A. Voth, J. Am. Chem. Soc. **122**, 12027-12028 (2000).
395. R. Schöllhorn, E. Sick, and A. Lerf, Mater. Res. Bull. **10**, 1005-1012 (1975).
396. M. Ghidiu, J. Halim, S. Kota, D. Bish, Y. Gogotsi, and M. W. Barsoum, Chem. Mater. **28**, 3507-3514 (2016).
397. D. W. Smith, J. Chem. Edu. **54**, 540 (1977).

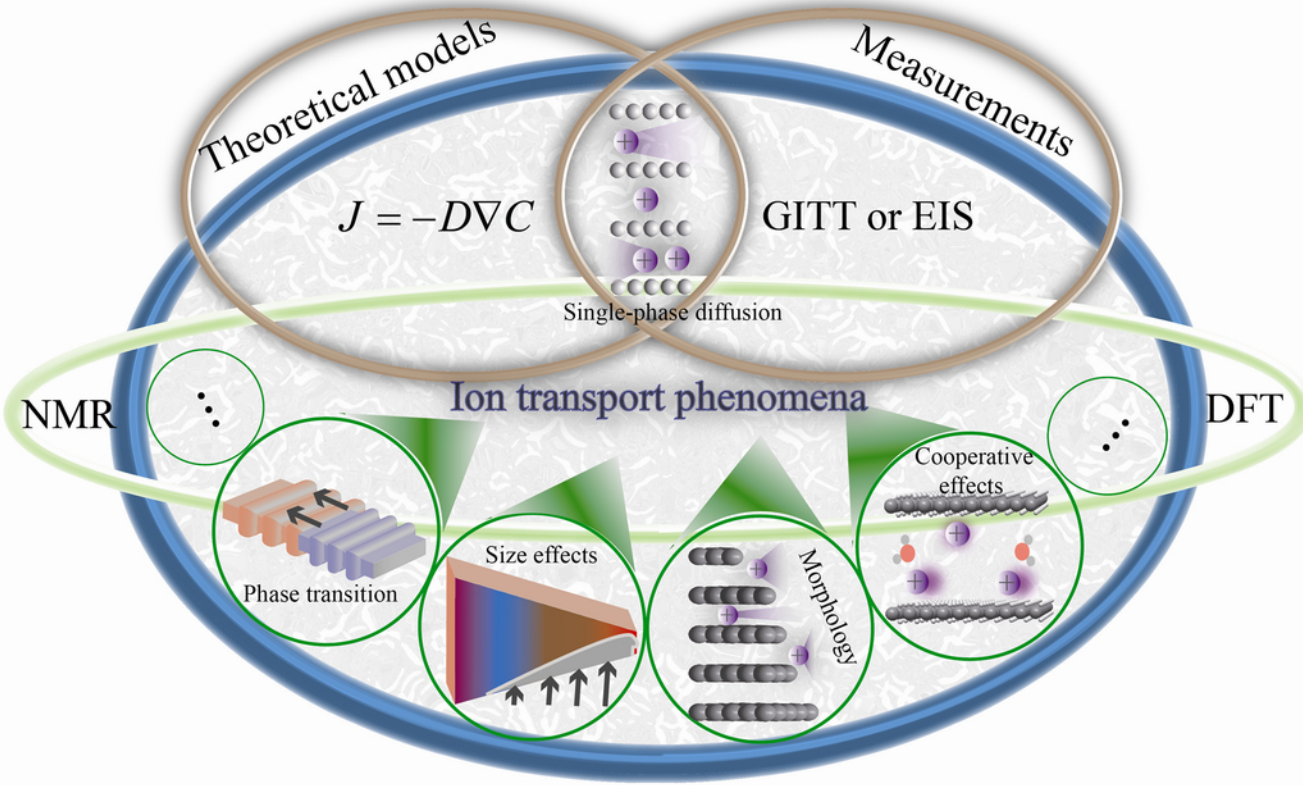
Theoretical models
Measurements
$J = -D\nabla C$
GITT or EIS
Single-phase diffusion
NMR
Ion transport phenomena
DFT
Phase transition
Size effects
Morphology
Cooperative effects

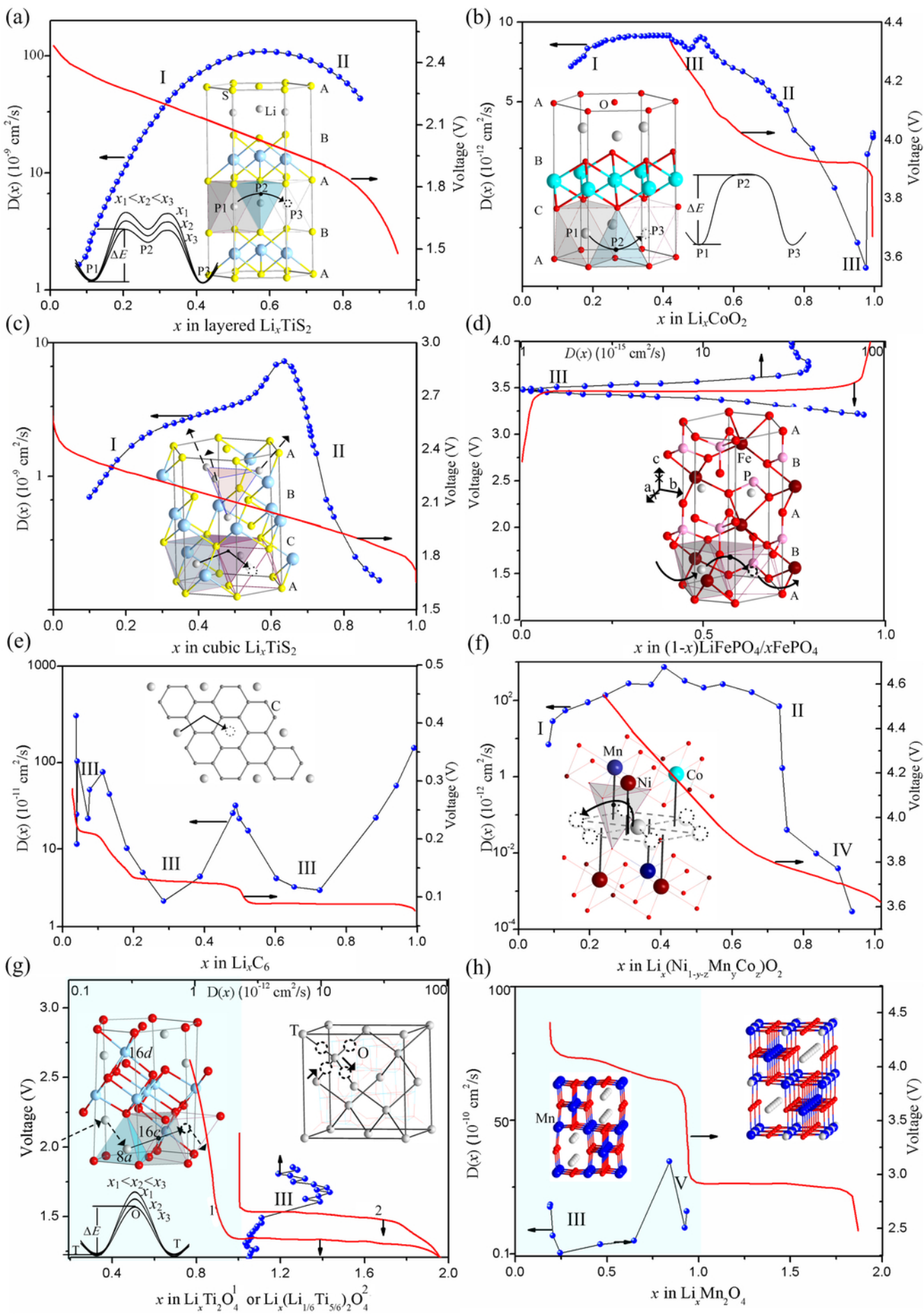
(a)
D(x) (10^-9 cm^2/s)
Voltage (V)
x in layered Li_xTiS_2
I
II
S
Li
A
B
P1
P2
P3
x1<x2<x3
ΔE
(b)
D(x) (10^-12 cm^2/s)
x in Li_xCoO_2
III
O
C
(c)
D(x) (10^-9 cm^2/s)
x in cubic Li_xTiS_2
(d)
D(x) (10^-15 cm^2/s)
x in (1-x)LiFePO_4/xFePO_4
Fe
P
(e)
D(x) (10^-11 cm^2/s)
x in Li_xC_6
(f)
D(x) (10^-12 cm^2/s)
x in Li_x(Ni_1-y-zMn_yCo_z)O_2
Mn
Ni
Co
IV
(g)
D(x) (10^-12 cm^2/s)
x in Li_xTi_2O_4^1 or Li_x(Li_1/6Ti_5/6)_2O_4^2
16d
16c
8a
T
O
(h)
D(x) (10^-10 cm^2/s)
x in Li_xMn_2O_4
V

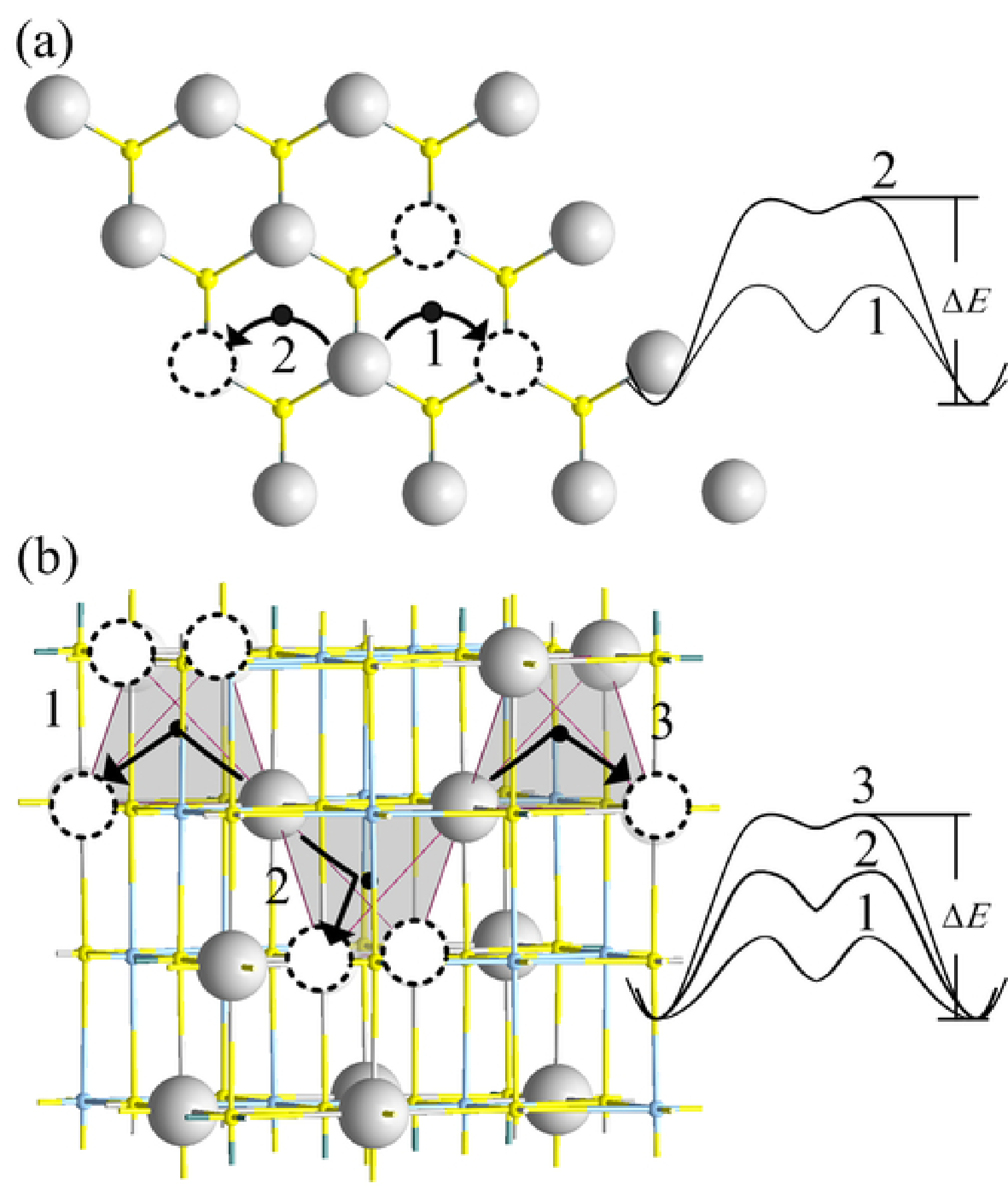
(a)
2
1
2
1
ΔE
(b)
1
3
2
3
2
1
ΔE

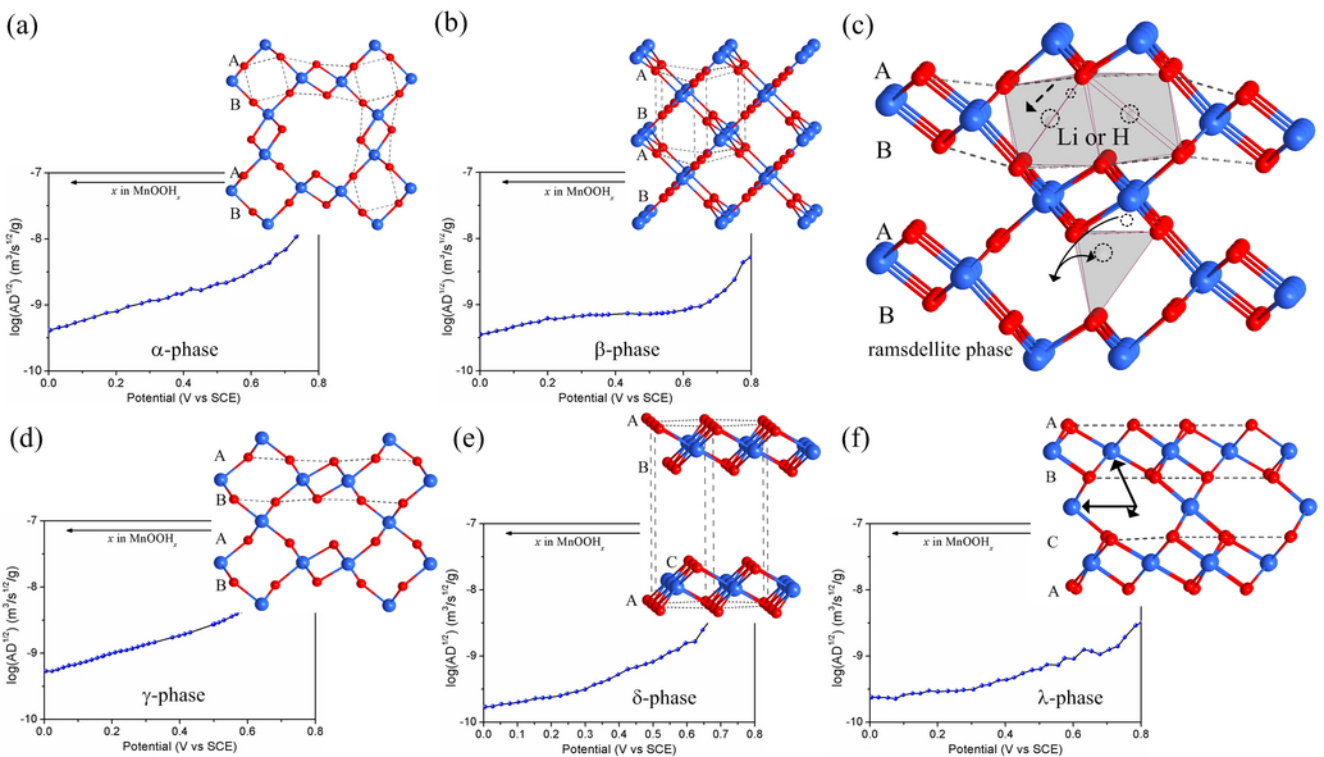
(a)
A
B
A
B
x in MnOOHx
log(AD1/2) (m3s-1/2/g)
-7
-8
-9
-10
α-phase
0.0
0.2
0.4
0.6
0.8
Potential (V vs SCE)
(b)
A
B
A
B
x in MnOOHx
log(AD1/2) (m3s-1/2/g)
β-phase
Potential (V vs SCE)
(c)
A
B
A
B
Li or H
ramsdellite phase
(d)
A
B
A
B
x in MnOOHx
log(AD1/2) (m3s-1/2/g)
γ-phase
Potential (V vs SCE)
(e)
A
B
C
A
x in MnOOHx
log(AD1/2) (m3s-1/2/g)
δ-phase
0.1
0.3
0.5
0.7
Potential (V vs SCE)
(f)
A
B
C
A
x in MnOOHx
log(AD1/2) (m3s-1/2/g)
λ-phase
Potential (V vs SCE)

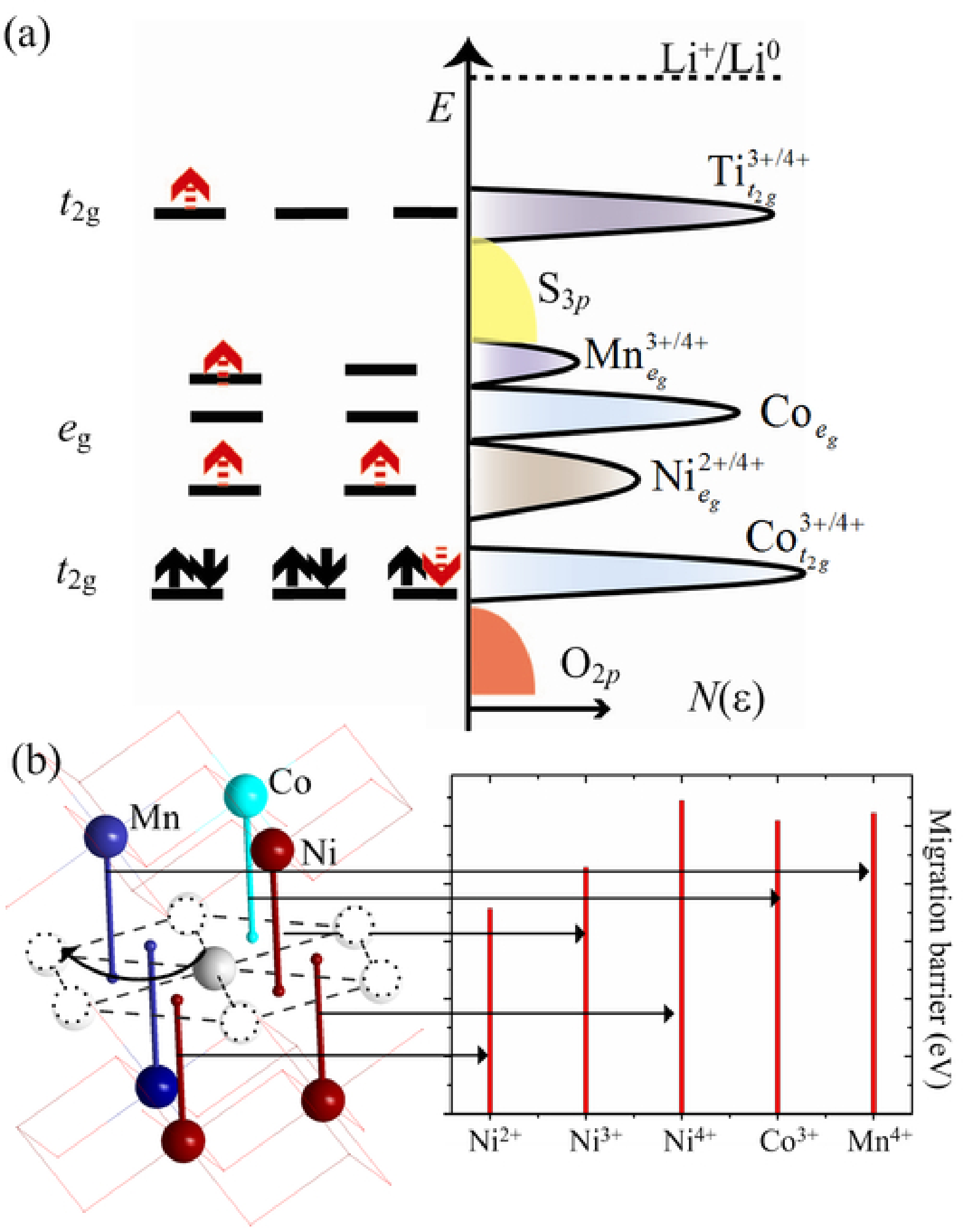
(a)
Li+/Li0
E
t2g
eg
t2g
Ti3+/4+ t2g
S3p
Mn3+/4+ eg
Co eg
Ni2+/4+ eg
Co3+/4+ t2g
O2p
N(ε)
(b)
Mn
Co
Ni
Migration barrier (eV)
Ni2+
Ni3+
Ni4+
Co3+
Mn4+

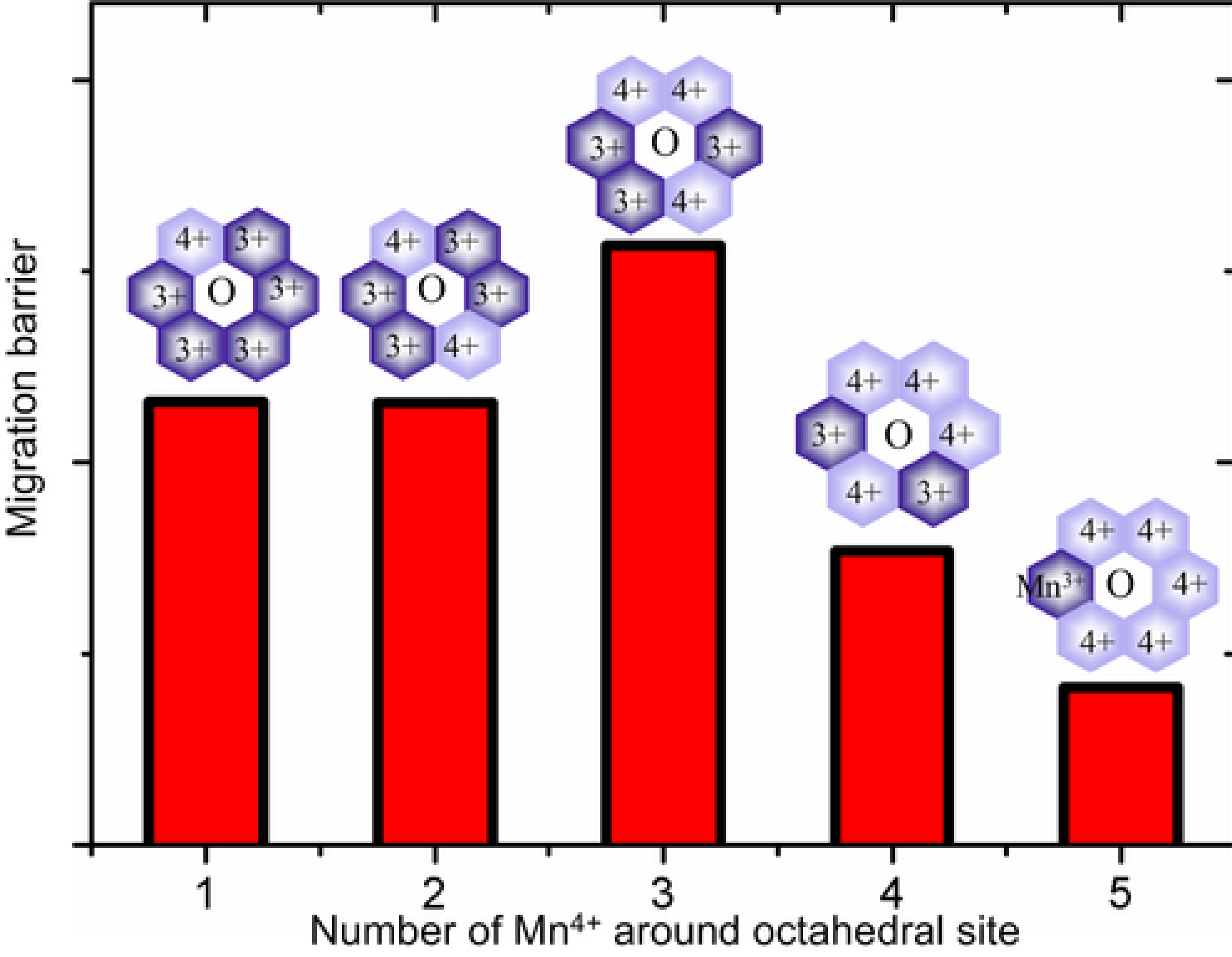
Migration barrier
4+ 3+
3+ O 3+
3+ 3+
4+ 3+
3+ O 3+
3+ 4+
4+ 4+
3+ O 3+
3+ 4+
4+ 4+
3+ O 4+
4+ 3+
4+ 4+
Mn3+ O 4+
4+ 4+
1
2
3
4
5
Number of Mn4+ around octahedral site

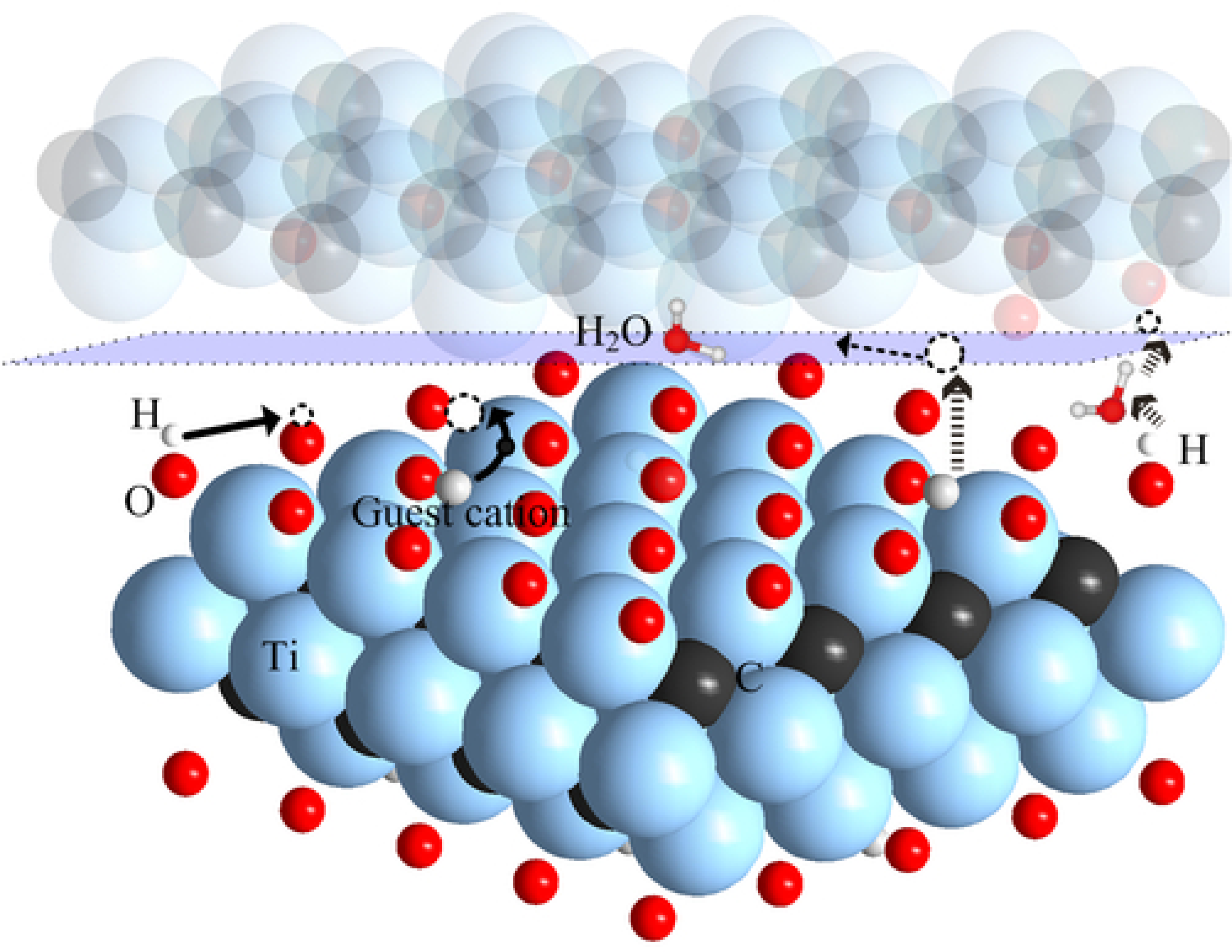
H_2O
H
O
Guest cation
Ti
C
H

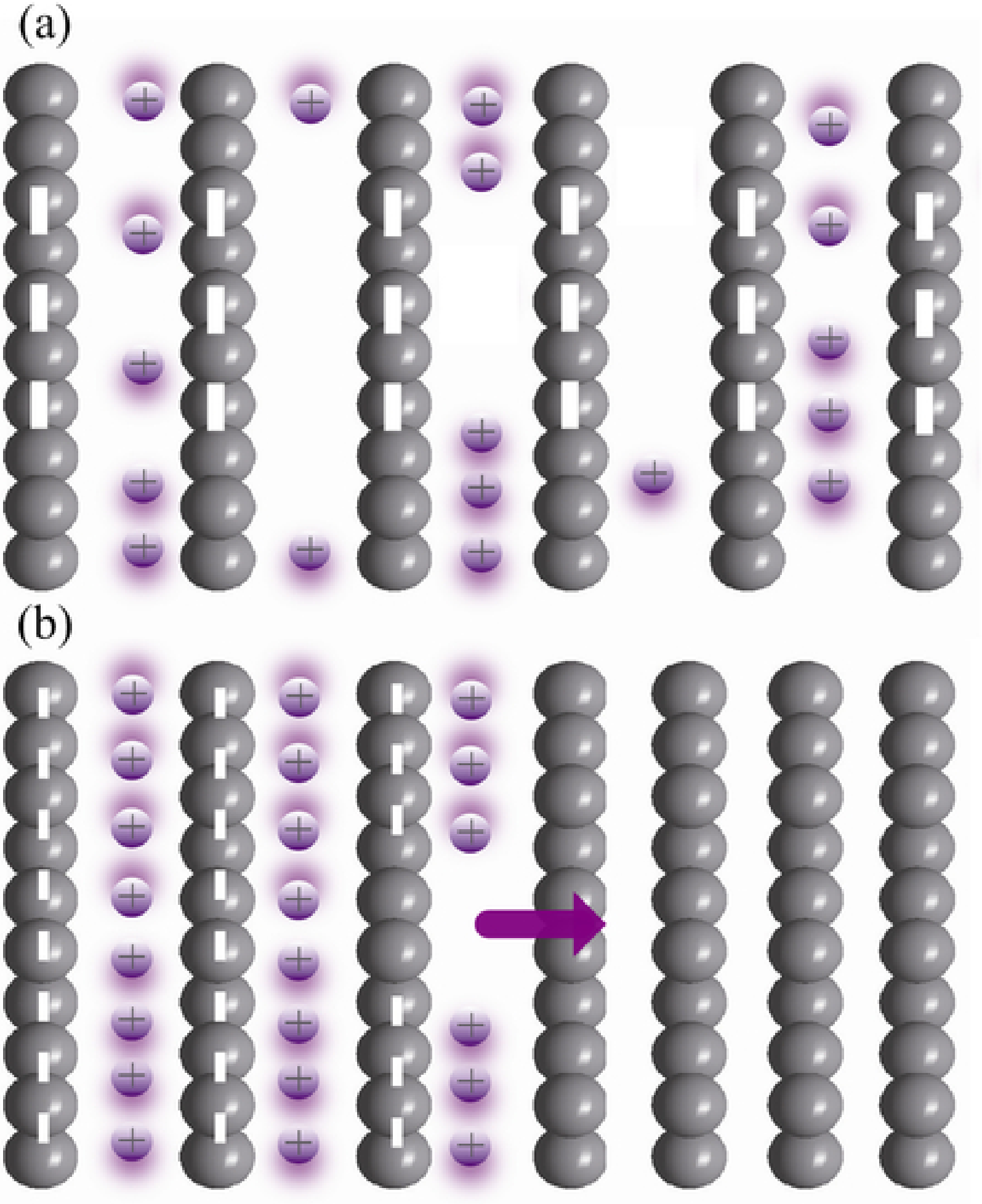
(a)
(b)

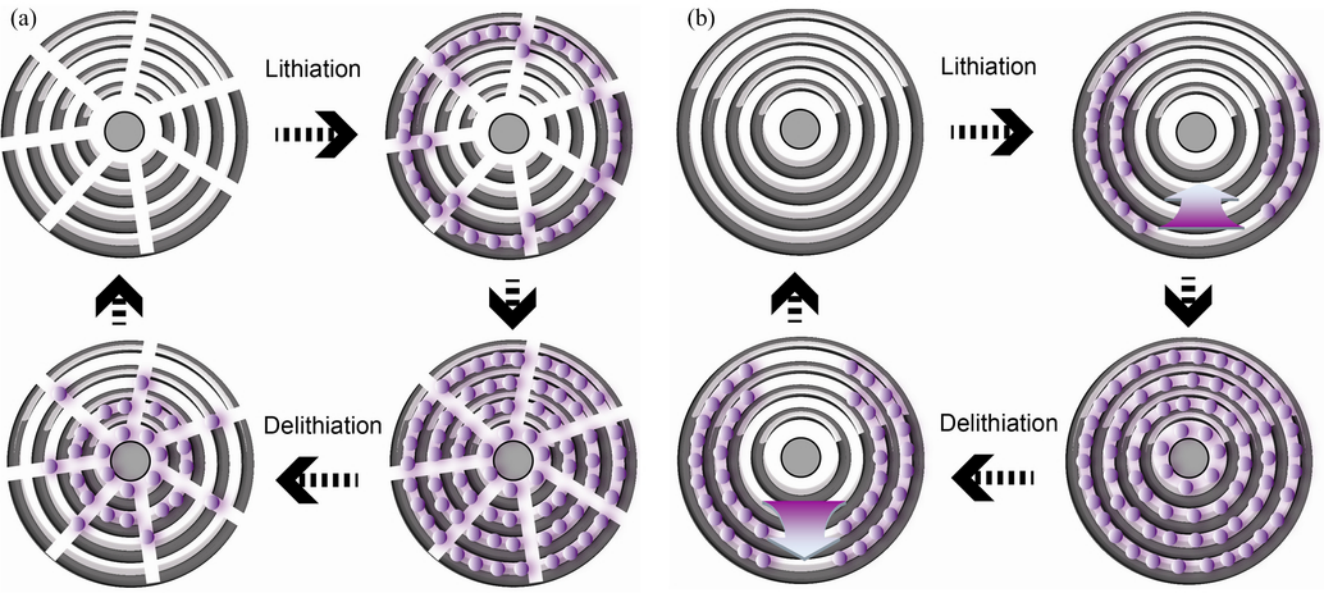
(a)
Lithiation
Delithiation
(b)
Lithiation
Delithiation

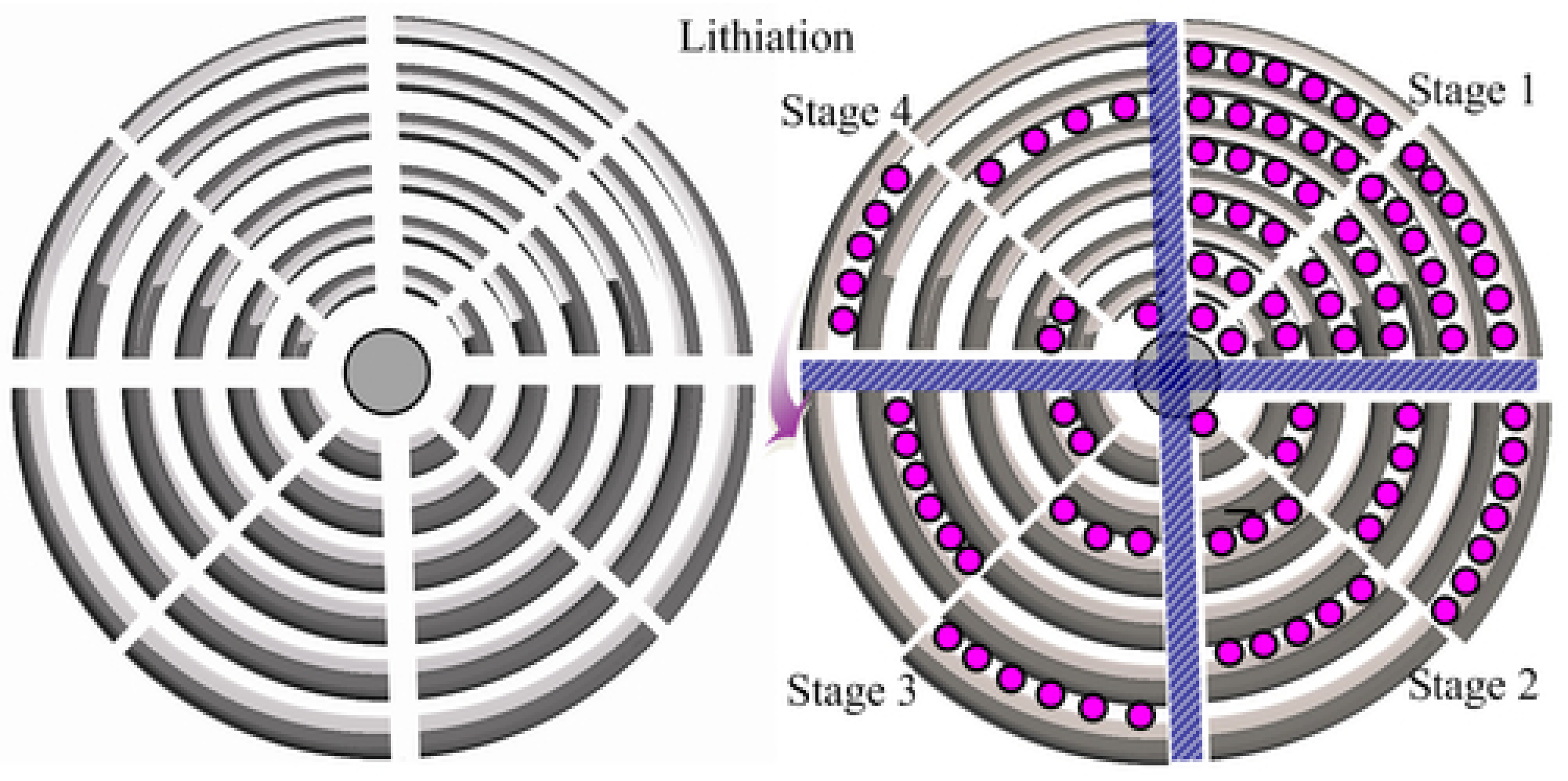
Lithiation
Stage 4
Stage 1
Stage 3
Stage 2

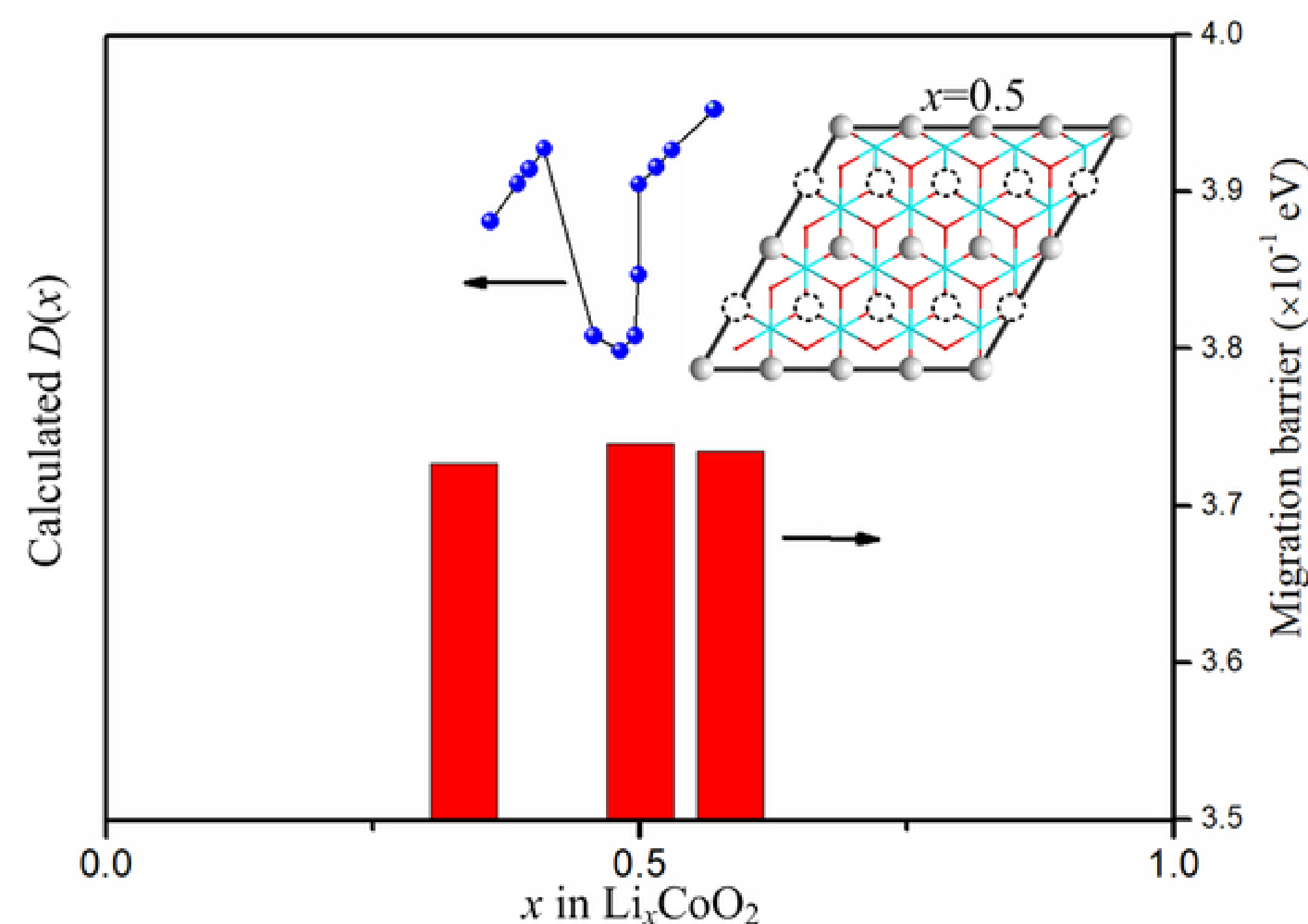
Calculated D(x)
Migration barrier (×10-1 eV)
x=0.5
4.0
3.9
3.8
3.7
3.6
3.5
0.0
0.5
1.0
x in LixCoO2

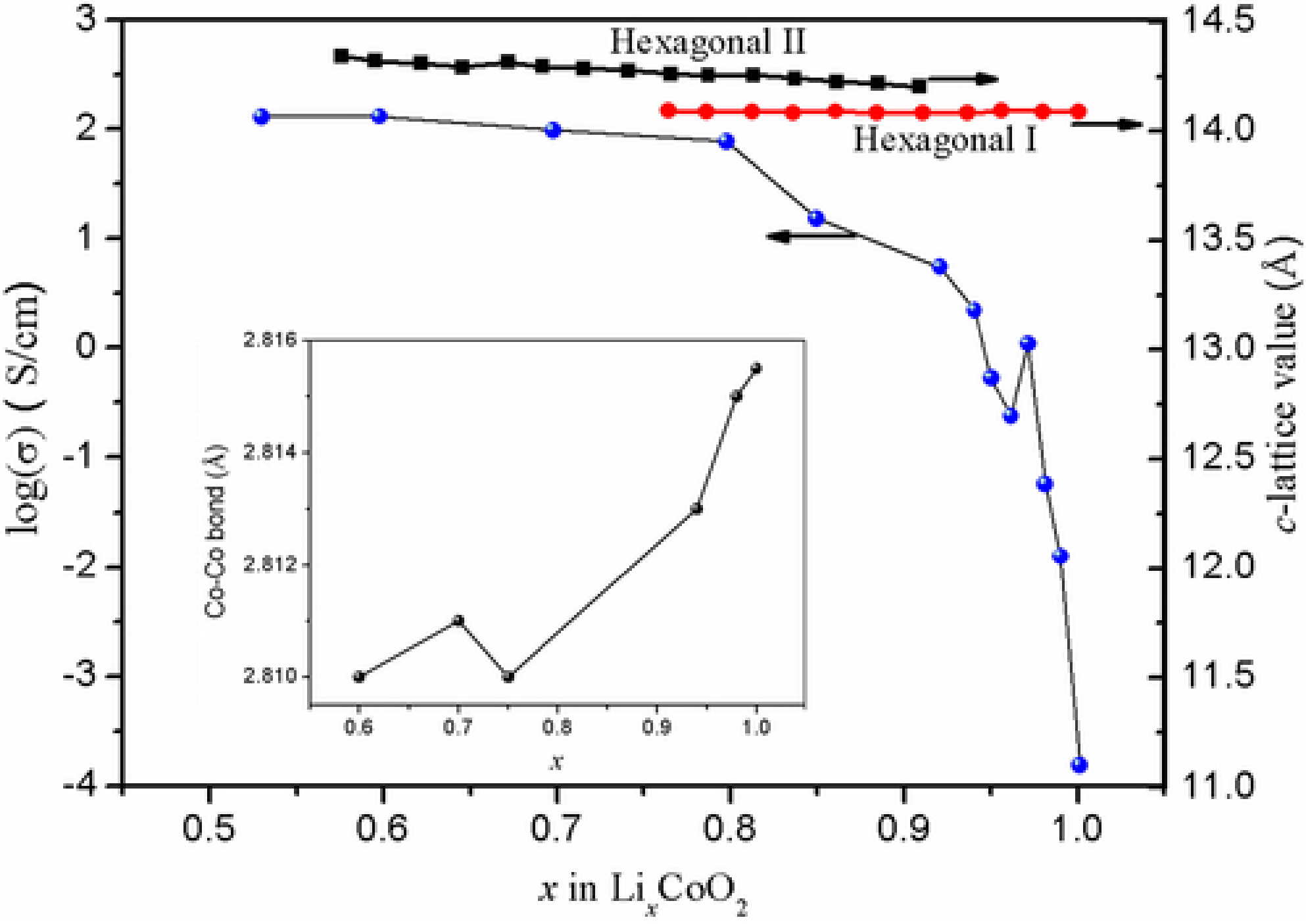
Hexagonal II
Hexagonal I
log(σ) (S/cm)
c-lattice value (Å)
x in Li_xCoO_2
Co-Co bond (Å)
x

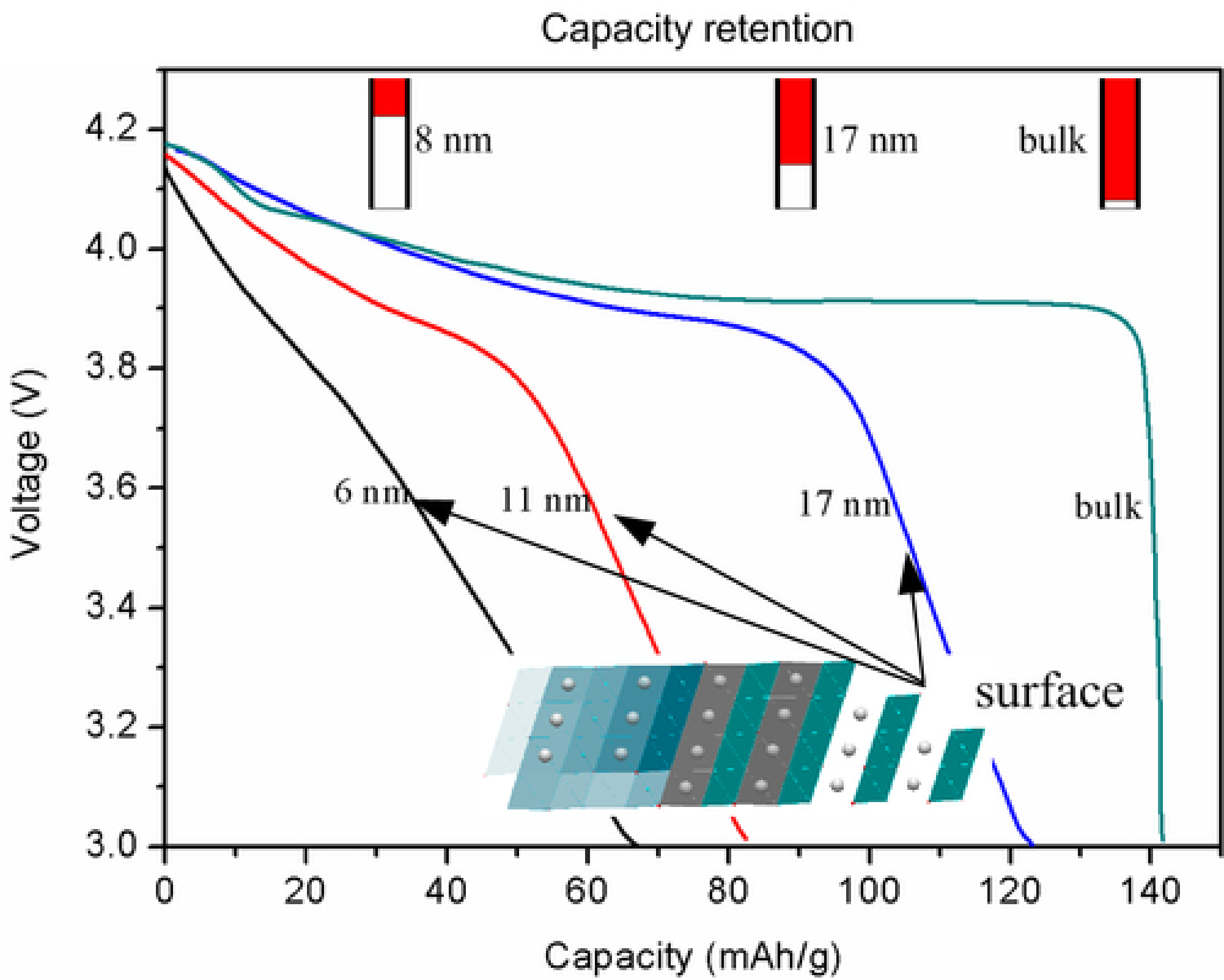
Capacity retention
8 nm
17 nm
bulk
6 nm
11 nm
17 nm
bulk
surface
Voltage (V)
Capacity (mAh/g)
4.2
4.0
3.8
3.6
3.4
3.2
3.0
0
20
40
60
80
100
120
140

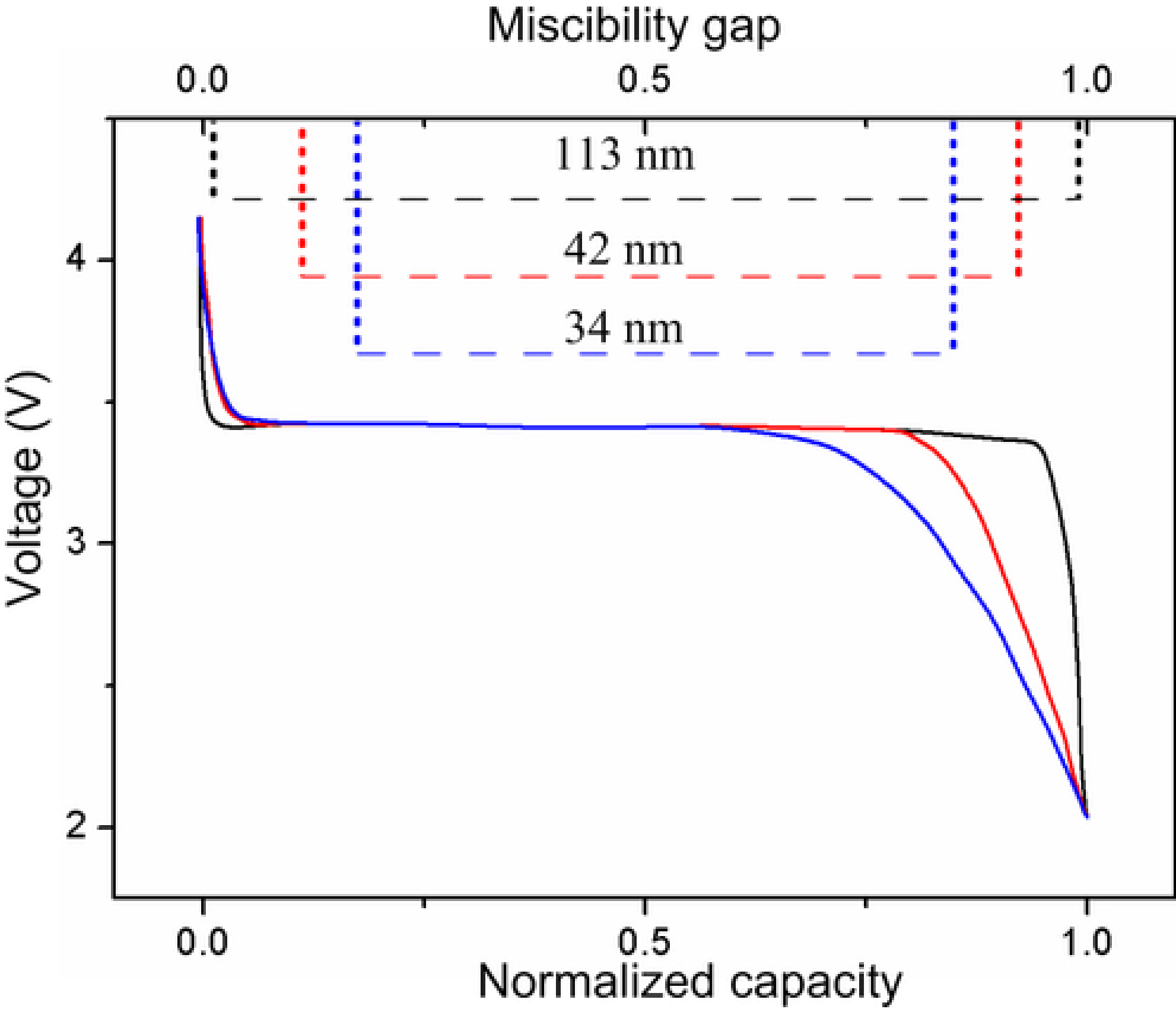
Miscibility gap
0.0
0.5
1.0
113 nm
42 nm
34 nm
4
3
2
Voltage (V)
0.0
0.5
1.0
Normalized capacity

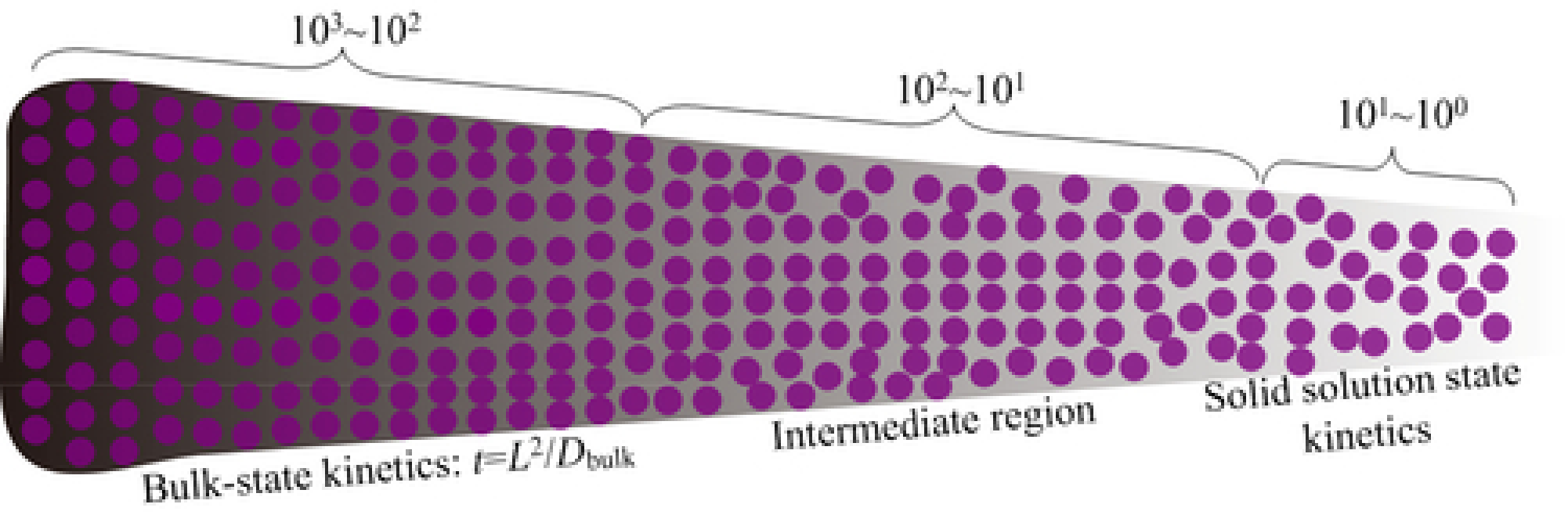
10^3~10^2
10^2~10^1
10^1~10^0
Bulk-state kinetics: $t=L^2/D_{bulk}$
Intermediate region
Solid solution state kinetics

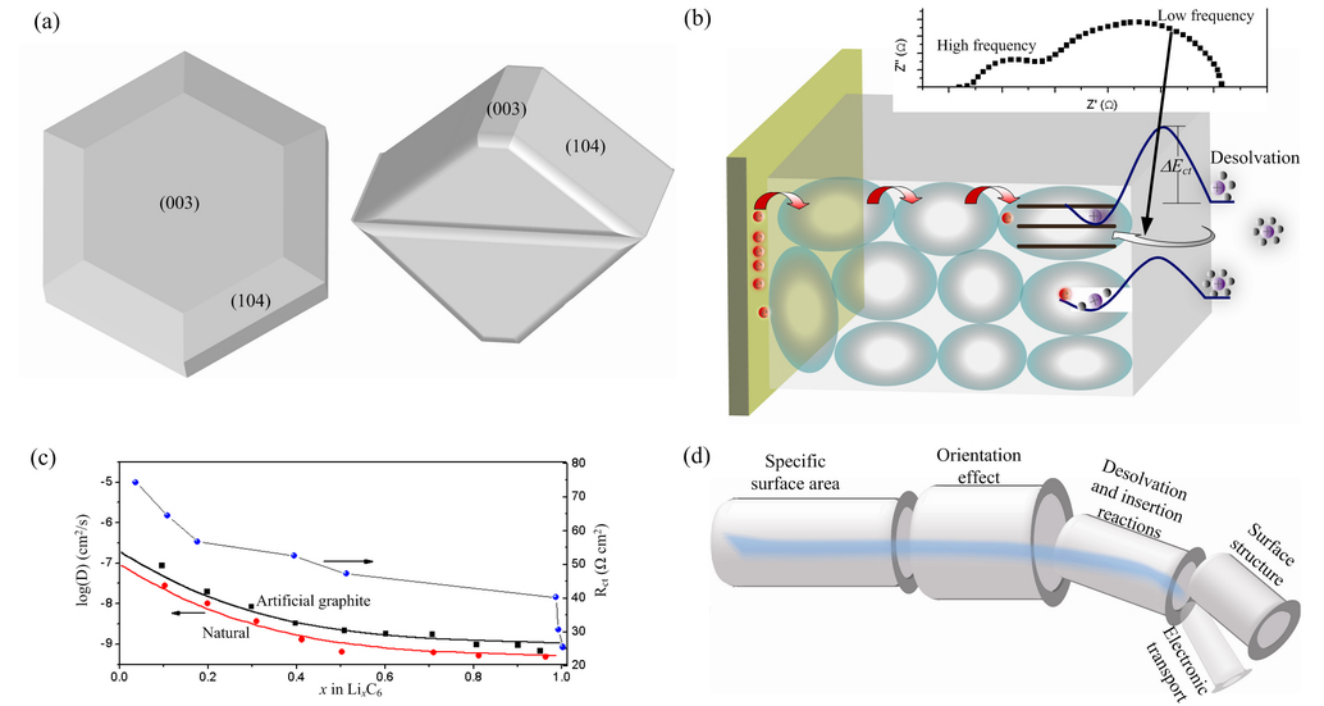
(a)
(003)
(104)
(003)
(104)
(b)
High frequency
Low frequency
Z'' (Ω)
Z' (Ω)
ΔE_{rct}
Desolvation
(c)
log(D) (cm²/s)
R_{ct} (Ω cm²)
Artificial graphite
Natural
x in Li_xC_6
(d)
Specific surface area
Orientation effect
Desolvation and insertion reactions
Surface structure
Electronic transport

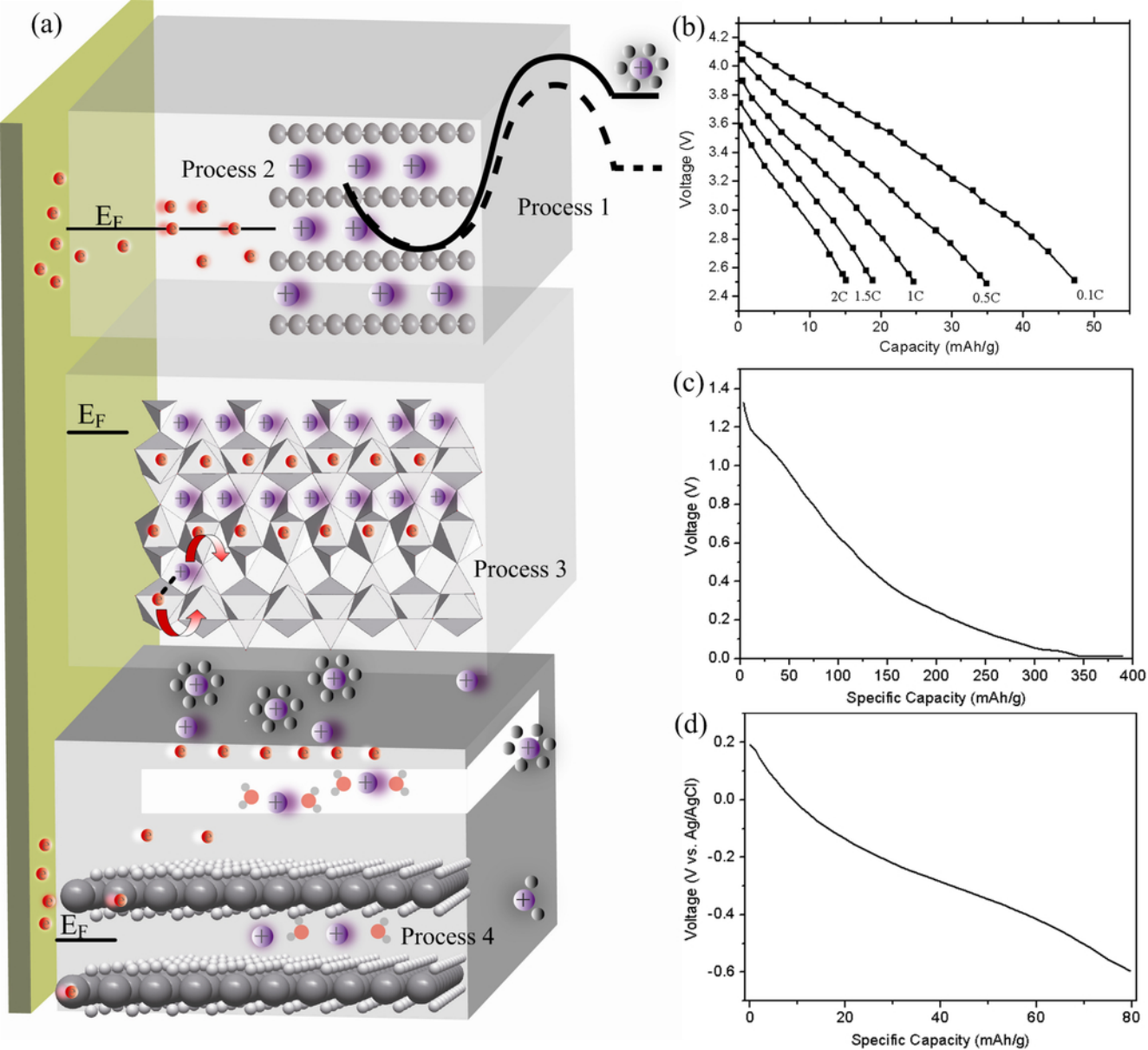
(a)
Process 2
Process 1
E_F
E_F
Process 3
E_F
Process 4
(b)
Voltage (V)
Capacity (mAh/g)
2C
1.5C
1C
0.5C
0.1C
(c)
Voltage (V)
Specific Capacity (mAh/g)
(d)
Voltage (V vs. Ag/AgCl)
Specific Capacity (mAh/g)

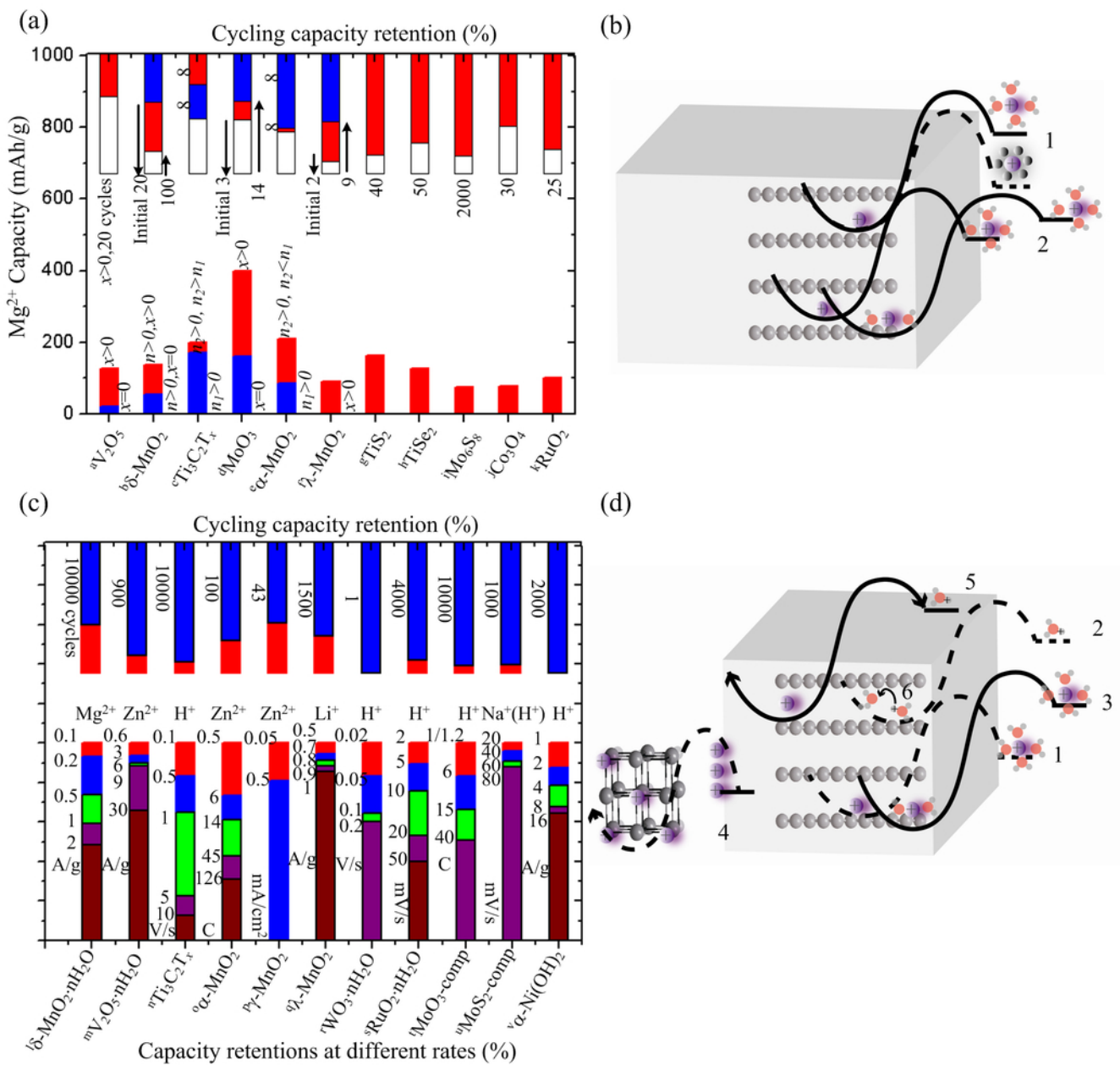
(a)
Cycling capacity retention (%)
Mg2+ Capacity (mAh/g)
1000
800
600
400
200
0
x>0,20 cycles
Initial 20
100
Initial 3
14
Initial 2
9
40
50
2000
30
25
aV2O5
bδ-MnO2
cTi3C2Tx
dMoO3
eα-MnO2
fγ-MnO2
gTiS2
hTiSe2
iMo6S8
jCo3O4
kRuO2
(b)
1
2
(c)
Cycling capacity retention (%)
10000 cycles
900
10000
100
43
1500
1
4000
10000
1000
2000
Mg2+ Zn2+ H+ Zn2+ Zn2+ Li+ H+ H+ H+ Na+(H+) H+
A/g
V/s
C
mA/cm2
mV/s
lδ-MnO2·nH2O
mV2O5·nH2O
nTi3C2Tx
oα-MnO2
pγ-MnO2
qζ-MnO2
rWO3·nH2O
sRuO2·nH2O
tMoO3-comp
uMoS2-comp
vα-Ni(OH)2
Capacity retentions at different rates (%)
(d)
1
2
3
4
5
6